Estuarine mixing

Hans Burchard[1], Knut Klingbeil[1], Xiangyu Li[1], Lloyd Reese[1], and W. Rockwell Geyer[2]

[1]Department of Physical Oceanography, Leibniz Institute for Baltic Sea Research Warnemünde, Rostock, Germany
[2]Department of Applied Physics and Engineering, Woods Hole Oceanographic Institution, Woods Hole, MA, USA

Correspondence: Hans Burchard (hans.burchard@iow.de)

Abstract. This review paper presents, explains and discusses major aspects of estuarine mixing which is defined as the destruction of salinity variance. Due to the large amounts of brackish water in estuaries produced by mixing of fresh river discharge and salty ocean water, mixing is one major characteristic of what is an estuary. In this review, mixing is quantified locally as well as on estuary-wide scales. Diagnostics of integrated mixing are given for estuarine volumes bounded by transects as well as isohalines (surfaces of constant salinity) moving with the flow. It is shown how entrainment across a moving isohaline surface depends on gradients of turbulent salt flux and mixing per salinity class. Various relations are derived that link estuarine salt mixing to other estuarine properties such as the freshwater discharge and the bulk estuarine circulation. For estuaries bounded towards the ocean by a fixed transect, the Knudsen mixing law is explained, where estuarine mixing is the product of the Knudsen salinities of inflowing and outflowing water masses and the river discharge. When the estuarine volume is bounded by a moving isohaline surface of salinity S, mixing inside the estuary is simply the product of S^2 and the river discharge. Major processes that drive estuarine mixing are presented on various time scales (tidal, fortnightly, weather and discharge time scales) and spatial scales (channel-shoal interaction, mixing fronts). As underlying methods for the quantification of mixing, observational concepts, as well as numerical modelling methods such as consistent turbulence closure modelling and numerical mixing analyses are presented. As an outlook, some future perspectives are sketched. Many of the concepts presented in this review are illustrated using simulation results from a numerical model setup of the Elbe River estuary.

1 Introduction

Estuaries are semi-enclosed coastal water bodies where riverine freshwater run-off from land is mixed with offshore salty ocean water to produce brackish water masses of intermediate salinities which are ejected offshore into the coastal ocean. In this sense, estuaries can be characterised as *mixing machines* (MacCready and Banas, 2011; Wang et al., 2017) with mixing rates far greater than in other parts of the ocean. Salt is the most characteristic constituent that is mixed in estuaries, because of (i) its significantly different concentration between rivers (typically < 0.5 g/kg) and the adjacent ocean (typically > 30 g/kg) and (ii) its inert character with no internal sinks and sources and no fluxes through the surface and the bottom. In addition to salt, there is a number of further properties, e.g., nutrients and pollutants, that are distinct between rivers and the ocean and which can be mixed in estuaries. This makes mixing a fundamental process in estuaries. We therefore follow here the definition of an estuary by Pritchard (1967) who stated *An estuary is a semi-enclosed coastal body of water which has a free connection with the open sea and within which sea water is measurably diluted with fresh water derived from land drainage.* Instead of *diluted* we would

prefer to say *mixed*, which effectively has the same meaning but highlights mixing as the defining process of estuaries. Water bodies that follow this principle are classical estuaries in the sense that their functioning is based on a net freshwater water supply. The contrasting case is given by inverse estuaries that are based on a net freshwater deficit due to evaporation, leading to the export of hypersaline water masses. The present review focusses on classical estuaries (in the following just denoted as *estuaries* for simplicity), whereas *inverse estuaries* are only occasionally discussed as contrasting systems. Fundamental concepts of estuaries and estuarine circulation have already been covered by previous reviews (MacCready and Geyer, 2010; Geyer and MacCready, 2014), such that we here focus on mixing in estuaries and its physical and ecological consequences.

Much of the estuarine literature focusses on mixing, starting with Knudsen's classic paper (Knudsen, 1900), in which he states: *As the freshwater spreads out over the seawater it mixes with it so that the salinity of the surface increases seawards* (translation by Burchard et al., 2018a). Fischer's review (Fischer, 1976) is entitled *Mixing and dispersion in estuaries*, highlighting its fundamental importance. Notwithstanding the attention focused on mixing throughout the estuarine literature, the actual meaning of the term *mixing* has often been vague or ambiguous: everyone is familiar with mixing via the daily-life experience of pouring milk into a cup of tea and using a tea spoon to mix it. However, amid the complex and multi-scale processes in estuaries, that simple concept is overwhelmed by consideration of larger scale processes associated with turbulence, shear dispersion and buoyancy flux. Turbulence, diffusion, dispersion, buoyancy flux and mixing are often loosely treated as synonyms, leading to confusion as to what we mean by mixing.

In this review, we come back to mixing in a cup (or glass beaker), or more precisely to the thermodynamic definition of mixing, which is the destruction of variance of some scalar quantity (Gibbs, 1878). In the estuarine context, we focus on the destruction of salinity variance, which is defined in the oceanic turbulence literature as χ_s, due to the down-gradient diffusion of salt by molecular diffusivity

$$\chi_s = 2\kappa \left[\left(\frac{\partial \tilde{s}}{\partial x} \right)^2 + \left(\frac{\partial \tilde{s}}{\partial y} \right)^2 + \left(\frac{\partial \tilde{s}}{\partial z} \right)^2 \right] \tag{1}$$

(Nash and Moum, 2002; Burchard and Rennau, 2008). In (1), κ is the molecular diffusivity of salt, $\tilde{s}$ is the turbulent salinity fluctuation, and square brackets denote Reynolds averaging (see Sec. 2.1 for details). In the turbulent environments of estuaries, this molecular process occurs at sub-millimetre scales, but it is the direct result of the turbulent and shearing motions acting on the salinity gradients at a wide range of scales extending all the way up to the horizontal dimensions of estuaries. It should be noted that the process of molecular mixing is irreversible inside the water body, such that $\chi_s \geq 0$. Negative mixing or *un-mixing* can however occur at the sea surface when evaporation takes place (Yu, 2010; Klingbeil and Lorenz, 2025) or sea ice is produced due to freezing (Notz and Worster, 2009) and in desalination plants to extract freshwater from salt water (reverse osmosis, Kim et al., 2019). In numerical models, *un-mixing* can also occur due to discretisation errors of advection schemes (Henell et al., 2023). Maintaining the strict thermodynamic definition of mixing turns out to be a powerful approach to examining estuarine processes, because salinity variance can be defined locally, as is often done in the turbulence literature, as well as globally, at the overall scale of the estuary. We do not question the importance of other concepts, such as vertical buoyancy flux and horizontal dispersion, but in this review we retain the strict definition of mixing to explore the processes responsible for its occurrence in estuaries as well as its quantitative relationship to estuarine exchange flow.

Throughout this review, exemplary data from a numerical simulation of the Elbe River estuary in northern Germany are used to demonstrate the different mixing theories. The Elbe River estuary is an elongated meso-tidal estuary with one major discharge source at the landward end for which several studies of estuarine mixing have been carried out (Reese et al., 2024, 2026; Burchard et al., 2025). A brief introduction into the Elbe River estuary is given in Sec. C of the appendix.

This review is structured as follows: After this introduction into the topic of estuarine mixing (Sec. 1), the existing theories on estuarine mixing are defined and discussed (Sec. 2). This section is structured into micro-structure mixing (Sec. 2.1) and parameterised mixing (Sec. 2.2), where Reynolds decomposition and turbulence closure assumptions are applied. The mixing definitions from Sec. 2 as well as the Total Exchange Flow analysis framework (Sec. 3.2) will be used in Sec. 3 (Estuarine Circulation and Mixing) to quantify mixing in entire estuaries. Before discussing estuarine mixing, we give a brief introduction to estuarine hydrodynamics (Sec. 3.1). For the mixing quantification, we first present the theory using fixed transects (Knudsen theories, see Sec. 3.3). Water Mass Transformation (WMT) theories (Sec. 3.4) are explained from which mixing laws for estuarine volumes bounded by isohaline surfaces as the seaward boundary are derived (Sec. 3.5). Sec. 3 concludes with some remarks on the relation between estuarine mixing and estuarine circulation (Sec. 3.6) and mixing of constituents other than salt (Sec. 3.7). While Sec. 2 and Sec. 3 focus on the definition and discussion of mixing, Sec. 4 gives examples for the most important estuarine processes that drive mixing. Those processes are related to single tides (Sec. 4.1.1), the spring-neap cycle (Sec. 4.1.2), time scales of river discharge and meteorological forcing (Sec. 4.1.3), channel-shoal interaction (Sec. 4.2.1) and mixing at fronts (Sec. 4.2.2). As methods to help quantifying mixing in estuaries, techniques to observe estuarine mixing are introduced (Sec. 5.1) and numerical modelling techniques are presented (Sec. 5.2), with a focus on turbulence closure modelling (Sec. 5.2.1) and numerical mixing (Sec. 5.2.2). Finally, some future perspectives are discussed in Sec. 6. The extensive appendix contains details about an analytic illustrative example for small-scale mixing (App. A), some key budget equations related to salinity variance (App. B), information about the Elbe River estuary model used to provide estuarine mixing examples (App. C), a derivation of the coordinate transformation of the vertical salinity equation (App. D), an explanation for the calibration of two-equation turbulence closure models (App. E), and derivations for the numerical mixing example (App. F). At the end of the appendix, a table with the most important variables, their definitions, units and defining equations is presented (Tab. 2).

2 Quantification of mixing

While mixing occurs on the micro-scale only, its integral effects are most prominently effective on the large, estuarine scale. We therefore start our explanations with the quantification of local stirring and mixing. This will first be based on molecular diffusion on the micro-scale and Reynolds averaging on the macro-scale (Sec. 2.1) and then parameterised by means of turbulence closures as it would be calculated in numerical models of estuaries (Sec. 2.2).

2.1 Micro-structure mixing

Mixing of a tracer s (for which we use salinity here as an example) occurs at the micro-scale when tracer gradients are reduced by molecular diffusion, following the Fickian law,

$$\frac{\partial \check{s}}{\partial t} + \frac{\partial}{\partial x_j}\left(\check{u}_j \check{s} - \kappa \frac{\partial \check{s}}{\partial x_j}\right) = 0, \tag{2}$$

where the Einstein summation convention $a_j b_j = \sum_{j=1}^{3} a_j b_j = a_1 b_1 + a_2 b_2 + a_3 b_3$ has been applied. In (2), $\check{s}$ is the instantaneous tracer concentration $\check{s} = [s] + \tilde{s}$ with the Reynolds-averaged tracer concentration $[s]$ and the fluctuating component $\tilde{s}$, κ is the molecular diffusivity of salinity, and $\check{u} = \check{u}_1$ and $\check{v} = \check{u}_2$ are the horizontal and $\check{w} = \check{u}_3$ is the vertical velocity component. The terms in the brackets on the left hand side of (2) are the advective and the molecular diffusive fluxes, the divergence of which determines the change of the salinity distribution. This transport equation determines the salinity distribution on all scales ranging from the sub-millimetre scales of molecular diffusion to the global scales of meridional overturning circulation, including scales of estuarine mixing.

In turbulence theory, the Reynolds average (also called ensemble average) is defined as the average of an infinite number of macroscopically identical but microscopically different flow realisations, where the turbulent random fluctuations are averaged out (Lesieur, 2008). Consequently, $[\tilde{s}] = 0$. In estuarine physics, and similarly in most fields of larger-scale oceanography, the Reynolds-averaged rather than the instantaneous properties of the flow are considered. Field observations of tracer concentrations (e.g., from Conductivity-Temperature-Depth (CTD) probes) as well as numerical model results are supposed to represent Reynolds-averaged quantities. A continuity equation (incompressibility condition) is used in most ocean models:

$$\frac{\partial \check{u}_i}{\partial x_i} = 0, \quad \frac{\partial [u_i]}{\partial x_i} = 0, \quad \frac{\partial \tilde{u}_i}{\partial x_i} = 0, \tag{3}$$

applying to instantaneous and thus to Reynolds-averaged and fluctuating velocity fields. Using (2), a dynamic equation for the Reynolds-averaged salinity can be derived:

$$\frac{\partial [s]}{\partial t} + \frac{\partial}{\partial x_j}\left([u_j][s] + [\tilde{u}_j \tilde{s}] - \kappa \frac{\partial [s]}{\partial x_j}\right) = 0, \tag{4}$$

with the advective tracer flux $[u_j][s]$, the turbulent tracer flux $[\tilde{u}_j \tilde{s}]$ and the diffusive tracer flux $-\kappa \partial [s]/\partial x_j$. Based on (2), it is also possible to derive an equation for the micro-structure tracer variance $[\tilde{s}^2]$:

$$\frac{\partial \left[\tilde{s}^2\right]}{\partial t} + \frac{\partial}{\partial x_j}\left(\left[u_j\right]\left[\tilde{s}^2\right] + \left[\tilde{u}_j \tilde{s}^2\right] - \kappa \frac{\partial [\tilde{s}^2]}{\partial x_j}\right) = \underbrace{-2[\tilde{u}_j \tilde{s}] \frac{\partial [s]}{\partial x_j}}_{P_s} \underbrace{- 2\kappa \left[\left(\frac{\partial \tilde{s}}{\partial x_j}\right)^2\right]}_{\chi_s} \tag{5}$$

(see, e.g., Eq. 5 by Mellor and Yamada, 1974). In (5), P_s quantifies the production of micro-structure variance due to turbulent stirring (with the Reynolds-averaged tracer gradient vector $\partial [s]/\partial x_j$) and χ_s represents destruction of microstructure variance due to molecular mixing.

Multiplying (4) by $2[s]$ gives a transport equation for the square of the Reynolds-averaged tracer:

$$\frac{\partial [s]^2}{\partial t} + \frac{\partial}{\partial x_j}\left([u_j][s]^2 + 2[\tilde{u}_j\tilde{s}][s] - \kappa \frac{\partial [s]^2}{\partial x_j} \right) = \underbrace{2[\tilde{u}_j\tilde{s}]\frac{\partial [s]}{\partial x_j}}_{-P_s} - 2\kappa \left(\frac{\partial [s]}{\partial x_j} \right)^2, \tag{6}$$

where on the right-hand side the stirring term P_s appears as a sink term besides a destruction term due to molecular diffusivity. In contrast to (5), where the destruction of micro-structure variance occurs due to molecular diffusivity acting on micro-structure gradients $\partial\tilde{s}/\partial x_j$, in (6) the molecular diffusivity acts on the much smaller Reynolds-averaged gradient $\partial[s]/\partial x_j$ such that this term is generally negligible. This means that variance is first transferred from the Reynolds-averaged regime of (6) to the turbulent regime (5), where it is then dissipated. In turbulence closure modelling typically $P_s = \chi_s$ (see, e.g., Eq. 31 by Mellor and Yamada, 1974) is applied such that stirring equals mixing, following a local equilibrium assumption. More details on turbulence closure modelling suitable for estuaries are given in Sec. 5.2.

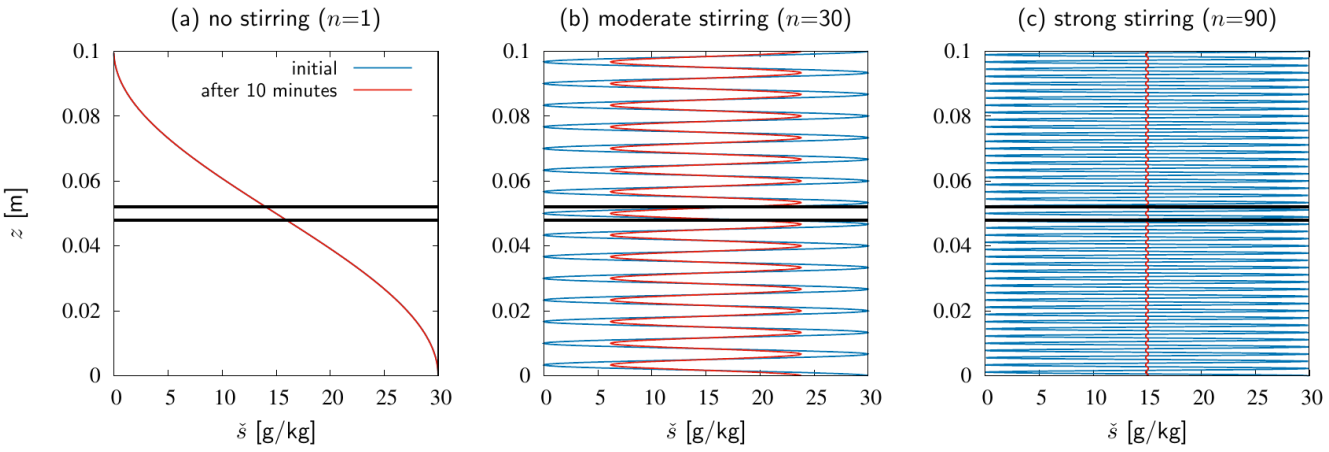

Figure 1. Stirring and mixing in a glass beaker: (a) Evolution of salinity $\check{s}$ for the case of no stirring, (b) little stirring, and (c) strong stirring. The initial distribution after the stirring is shown as blue lines, and the distribution after 10 minutes is shown as red lines. The parameters for the problem are chosen as height of fluid inside the one-dimensional glass beaker $D = 0.1$ m, and the molecular diffusivity of salinity, $\kappa = 10^{-9}\text{m}^2\ \text{s}^{-1}$. The two black bars mark the area over which the local variance is estimated. More details are given in Sec. A of the appendix.

In short: micro-structure tracer variance is produced by stirring P_s (increase of local micro-structure gradients due to turbulent eddies) and dissipated by mixing χ_s, while the divergence term on the left-hand side just spatially redistributes the micro-structure tracer variance. Note that the stirring term is twice the product of the turbulent flux times the Reynolds-averaged tracer gradient. The stirring term P_s is typically positive, since the Reynolds-averaged salinity gradient and the turbulent salt flux have opposite signs due to the generally down-gradient property of turbulent fluxes (classical exceptions occur in convective boundary layers, see e.g. Legay et al., 2025).

This can be explained by a laboratory experiment with salt mixing. A simple idealised model of this is given in Sec. A of the appendix and results are shown in Fig. 1. After having carefully pumped saltwater of 30 g/kg underneath freshwater (with some continuous mixing), the local salinity variance is mostly low: sufficiently small control volumes would contain water with a small salinity range (Fig. 1a). Introduction of turbulence by means of a spoon will lead to stirring (increase of P_s), such that local control volumes (marked as the area between the two black bars in Fig. 1) will contain streaks of saltwater at various ranges, with sharp gradients between them, such that the local variance $\left[\tilde{s}^2\right]$ is increased. This is demonstrated as initial conditions for moderate stirring (Fig. 1b) and strong stirring (Fig. 1c). Now, mixing χ_s will be moderately or strongly enhanced due to the small (and constant) molecular diffusivity κ acting on the strong micro-scale gradients $\partial\tilde{s}/\partial z$ (which are squared in the mixing term). At the end of this process, the salt will be almost fully diluted in the water such that local variance becomes small, with $\tilde{s} \to 0$ and $\breve{s} \to [s] = 15$ g/kg. Further introduction of turbulence by a spoon will not lead to further stirring (and thus not to further mixing), because the tracer gradients have vanished.

In real estuaries, stirring typically occurs due to vertical shear instabilities driven by tidal flow, generating large eddies as shown in Figs. 17 and 18 in Sec. 5.1. Via the classical turbulence downward cascade, smaller and smaller eddies are generated such that finally mixing is enhanced at the smallest scales. Since estuaries are typical narrow and friction-dominated, horizontal instabilities on the submesoscale (McWilliams, 2016) play a minor role for stirring. An exception would be large fjord-type estuaries with weak tides such as the Baltic Sea (Chrysagi et al., 2021).

Direct in-situ measurements of salinity mixing χ_s are difficult to obtain due to the small value of the molecular salinity diffusivity of $\kappa = \mathcal{O}(10^{-9}\mathrm{m}^2\mathrm{s}^{-1})$ and the consequently strong gradients at small scales, but successful attempts have been reported by Nash and Moum (2002) for locations on the continental shelf. According to these authors the salinity-gradient spectrum peaks at dissipative scales ten times smaller than the temperature-gradient spectrum, such that most salinity variance decay occurs in the sub-millimetre range. Therefore, and because of estuaries having generally higher levels of turbulence than continental shelves, direct observations of χ_s in estuaries are not feasible, and indirect observations are needed (see Sec. 5.1). Instead of using turbulence observations, mixing in estuaries is mostly studied by means of well-calibrated fine-resolution numerical models equipped with accurate numerical discretisations and physically based turbulence closures (Sec. 5.2).

2.2 Mixing at resolved local scales

Whereas the irreversible process of mixing happens at very small scales, the quantification of mixing is accomplished both in observations and in models through the application of turbulence closure assumptions (Mellor and Yamada, 1974; Peters and Bokhorst, 2001; Umlauf and Burchard, 2005). On the level of numerical ocean models, the turbulent fluxes are typically parameterised by means of the eddy diffusivity assumption, resulting in down-gradient turbulent tracer fluxes:

$$[\tilde{u}\tilde{s}] = -K_h \frac{\partial s}{\partial x}; \quad [\tilde{v}\tilde{s}] = -K_h \frac{\partial s}{\partial y}; \quad [\tilde{w}\tilde{s}] = -K_v \frac{\partial s}{\partial z}, \tag{7}$$

now using salinity $s = [s]$ as Reynolds-averaged tracer concentration. In (7), K_h is the horizontal eddy diffusivity and K_v is the vertical eddy diffusivity. With this the Reynolds-averaged salinity budget equation (4) becomes:

$$\underbrace{\frac{\partial s}{\partial t}}_{\text{change}} + \underbrace{\frac{\partial (us)}{\partial x} + \frac{\partial (vs)}{\partial y} + \frac{\partial (ws)}{\partial z}}_{\text{advection}} \underbrace{- \frac{\partial}{\partial x}\left(K_h \frac{\partial s}{\partial x}\right) - \frac{\partial}{\partial y}\left(K_h \frac{\partial s}{\partial y}\right) - \frac{\partial}{\partial z}\left(K_v \frac{\partial s}{\partial z}\right)}_{\text{diffusion}} = 0, \tag{8}$$

showing that salinity changes are exclusively determined by the divergence of advective and turbulent fluxes. Note that in (8) molecular tracer fluxes have been neglected. With (7) the production of micro-structure variance due to stirring becomes

$$P_s = 2K_h \left(\frac{\partial s}{\partial x}\right)^2 + 2K_h \left(\frac{\partial s}{\partial y}\right)^2 + 2K_v \left(\frac{\partial s}{\partial z}\right)^2 \stackrel{!}{=} \chi_s, \tag{9}$$

where in the last step stirring and mixing of micro-structure salinity variance are set equal, which is a typical assumption in turbulence closure modelling (see Sec. 2.1). The local variance decay χ_s is used as a local measure for the mixing of Reynolds-averaged salinity (Burchard and Rennau, 2008). This local equilibrium assumption is generally valid on the temporal and spatial scales that are resolved by numerical ocean models. In detail, χ_s appears as a sink term in both the salinity variance and salinity-square budgets. The corresponding derivation is shown in Sec. B of the appendix.

In estuaries, the vertical term of the salinity variance decay (9) typically dominates over the horizontal terms due to the dominance of tidally-driven vertical shear (Li et al., 2024), such that we obtain

$$\chi_s \approx \chi_{s,v} = 2K_v \left(\frac{\partial s}{\partial z}\right)^2. \tag{10}$$

This is the case because in estuaries horizontal turbulent transports and their divergences are small compared to the vertical transports, with the consequence that in estuarine models the horizontal diffusion is often neglected in the parameterised salinity budget equation (8) as well as in the salinity variance equation (B1). Due to this dominance of vertical processes in estuaries, it is instructive to study the balance of the vertical variance,

$$s_v'^2 = \left(s - \frac{1}{\eta + H}\int_{-H}^{\eta} s \,\mathrm{d}z\right)^2 = \left(s - \bar{s}_v\right)^2, \tag{11}$$

for the vertical integral of which the following budget equation can be derived from (8), see Li et al. (2018) for details:

$$\underbrace{\frac{\partial}{\partial t}\int_{-H}^{\eta} s_v'^2 \,\mathrm{d}z}_{\text{rate of change}} \underbrace{+ \frac{\partial}{\partial x}\int_{-H}^{\eta} u s_v'^2 \,\mathrm{d}z + \frac{\partial}{\partial y}\int_{-H}^{\eta} v s_v'^2 \,\mathrm{d}z}_{\text{advection}} = \underbrace{-2\int_{-H}^{\eta} u_v' s_v' \frac{\partial \bar{s}_v}{\partial x}\,\mathrm{d}z - 2\int_{-H}^{\eta} v_v' s_v' \frac{\partial \bar{s}_v}{\partial y}\,\mathrm{d}z}_{\text{horizontal straining}} \underbrace{- \int_{-H}^{\eta} \chi_{s,v}\,\mathrm{d}z}_{\text{vertical mixing}}, \tag{12}$$

where η is the surface elevation. Eq. (12) shows that the vertical variance balance is time-dependent and spatially variable. In contrast to the total salinity variance budget, the vertical salinity variance budget has source terms, the so-called horizontal straining terms, representing the conversion of horizontal variance ($s_h'^2$, where $s_h' = s_{\mathrm{tot}}' - s_v' = \bar{s}_v - \bar{s}_{\mathrm{tot}}$) associated with the horizontal salinity gradient $\partial \bar{s}_v / \partial x$ to vertical variance (Simpson et al., 1990). Note that horizontal straining is split into

longitudinal straining and lateral straining (first and second term of horizontal straining, respectively) and can be a source (mainly during ebb straining) and a sink (mainly during flood straining) of vertical variance, whereas the effect of vertical mixing is always to reduce the vertical variance. According to Li et al. (2018), estuarine mixing is driven in a three-step process: First, horizontal variance is provided to the estuary by means of boundary variance transports from the river and the ocean, through the *boundary transport* term in (B2). Then the *horizontal straining* term in (12) converts horizontal variance into vertical variance, which is then in a third step mixed away by the *vertical mixing* term in (12).

3 Estuarine circulation and mixing

After a short introduction into the basics of estuarine hydrodynamics in Sec. 3.1, we here introduce mixing concepts for entire estuaries, first following the classical theory proposed by Knudsen (1900), see Sec. 3.3, which can be calculated by using the Total Exchange Flow (TEF) analysis framework across fixed transects (Sec. 3.2). After introducing local isohaline theory (Sec. 3.4), we show how to analyse mixing in estuarine volumes bounded by an isohaline instead of a fixed transect (Sec. 3.5). Based on the local isohaline theory, the quantification of estuarine circulation is directly related to mixing (Sec. 3.6). Finally, mixing of constituents other than salt is briefly discussed (Sec. 3.7).

3.1 Basics of estuarine hydrodynamics

Although this review paper mainly focusses on estuarine salt mixing, a short introduction into the hydrodynamics determining the salt distribution and the turbulence available for salinity mixing will be given here. More detailed reviews can be found in MacCready and Geyer (2010) and Geyer and MacCready (2014).

Estuaries are characterised by a longitudinal salinity gradient extending from the region of the estuarine mouth with values typically close to ocean salinity (somewhat below 35 g/kg) to values of river salinity (typically below 0.5 g/kg) in the fresh-water range. Since saline water is more dense than fresh water, this salinity gradient causes a longitudinal density gradient which results in a longitudinal pressure gradient in the momentum balance, with a barotropic and a baroclinic term. While the baroclinic term is zero at the surface and increases continuously towards the bottom (driving water in up-estuarine direction, with intensification at the bottom), the barotropic pressure-gradient term is independent of the vertical position and drives water out of the estuary. In addition oscillating tides provide small-scale turbulence resulting in vertical shear stress divergence and consequently in diffusion of the longitudinal velocity profiles. The combination of these forces results in a gravitationally-driven tidally averaged exchange flow, with near-bottom flow directed in up-estuarine direction and near-surface flow directed in down-estuarine direction, the so-called gravitational circulation. The strength of the stratifying gravitational circulation depends on the ratio of the gravitational forces due to the longitudinal density gradient and the de-stratifying vertical shear stress divergence. This ratio is expressed as the Simpson number

$$\mathrm{Si} = \frac{D^2 |b_x|}{\langle u_*^2 \rangle} \tag{13}$$

(Simpson et al., 1990; Monismith et al., 1996; Stacey et al., 2008) with the water depth D, the horizontal buoyancy gradient $b_x = \partial b/\partial x$, the buoyancy $b = -g/\rho_0(\rho - \rho_0)$, the potential density ρ, the reference density ρ_0, the gravitational acceleration g, and the bottom friction velocity u_*. There are several other hydrodynamic processes contributing to estuarine exchange flow. One essential process is tidal straining (Simpson et al., 1990): During flood saltier ocean water is sheared over less salty estuarine water, such that the water column becomes statically unstable and thus highly turbulent such that properties are vertically homogenised. During ebb the opposite occurs, resulting in stable stratification and suppression of turbulence. This asymmetry of turbulence does not only affect the salt distribution, but also the velocity profiles: During flood up-estuarine momentum is transported downwards in a much stronger amount than down-estuarine momentum is transported downwards during ebb, which in a tidal average leads to an up-estuarine residual flow near the bottom (Jay and Musiak, 1994). This process has also been named ESCO (eddy-viscosity – shear covariance) by Dijkstra et al. (2017). In an idealised model study Burchard and Hetland (2010) could show that in tidally energetic flows the contribution of ESCO to estuarine circulation could be stronger than that of gravitational circulation. Other important hydrodynamic processes generating estuarine circulation are lateral circulation (Lerczak and Geyer, 2004), estuarine convergence (Ianniello, 1979; Burchard et al., 2014) and wind straining (Scully et al., 2005). It could be shown that gravitational circulation, ESCO, and lateral circulation are strongly scaling with Si (Burchard et al., 2011; Lange and Burchard, 2019). Since Si is larger during neap tide than during spring tide (due to smaller u_*), the estuarine exchange flow is expected to be stronger during neap tide. The estuarine circulation in concert with vertical mixing is a major process carrying salt into the estuary, against the river discharge. Often, this so-called shear dispersion process is parameterised by a horizontal diffusion term in the longitudinal salt balance equation (MacCready, 2004).

The Simpson number Si does also have a strong influence on the stratification in an estuary. For $\mathrm{Si} < 0.2$ (tidally energetic), the water column would be mixed throughout the tidal cycle. For $\mathrm{Si} > 1$ (weak tidal energy), stratification should be maintained during the entire tidal cycle. For intermediate situations with $0.2 \leq \mathrm{Si} \leq 1$, however, the water column should stratify during ebb and destratify during flood, leading to strain-induced periodic stratification (SIPS, Simpson et al., 1990; Verspecht et al., 2009). Since mixing is typically proportional to the square of the vertical salinity gradient, see (10), stratification has a major impact on estuarine mixing. Specific examples of physical drivers of estuarine mixing are discussed in Sec. 4.

3.2 Total Exchange Flow

The estuarine exchange flow of water masses defined by salinity, i.e., the net inflow of high salinity ocean waters and the net outflow of low salinity estuarine waters, can be best quantified in terms of time-averaged transports in fixed salinity classes. The resulting Total Exchange Flow (TEF) provides an analysis framework based on salinity coordinates rather than geopotential (z-)coordinates which is consistently linked to the Knudsen theory as well as to estuarine mixing. As shown by several authors (MacCready, 2011; Sutherland et al., 2011; Burchard et al., 2018a), the Eulerian (z-coordinate) framework could be mapped back to time-averaged salinities, but the resulting exchange flow profiles would significantly underestimate the exchange flow. Therefore, the TEF framework has developed into a major research tool for analysing estuarine dynamics. For the Baltic Sea, approaches similar to TEF had already been developed earlier (Walin, 1977; Döös et al., 2004). Here, we briefly explain the theoretical framework for TEF and refer to the literature for the details (MacCready, 2011; Burchard et al., 2018a).

Given a fixed transect T across an estuary, the time-averaged volume, salt and salt-squared transports across the transect for all salinities $> S$ are defined as

$$Q(S) = \left\langle \int\limits_{A(S)} u \,\mathrm{d}A \right\rangle, \quad Q_s(S) = \left\langle \int\limits_{A(S)} us \,\mathrm{d}A \right\rangle, \quad Q_{s^2}(S) = \left\langle \int\limits_{A(S)} us^2 \,\mathrm{d}A \right\rangle, \tag{14}$$

where triangular brackets denote temporal averaging, u is the velocity normal to the transect (positive when directed into the estuary) and $A(S)$ is the part of the transect area with instantaneous salinities $> S$. It should be noted that $Q(S)$ is the streamfunction of the estuarine circulation in salinity space (MacCready, 2011; Burchard et al., 2025). When defining $S_{\max}$ and $S_{\min}$ as the maximum and minimum salinities occurring on the transect during the averaging period, respectively, then sufficiently long averaging results in $Q(S_{\max}) = Q_s(S_{\max}) = Q_{S^2}(S_{\max}) = 0$, $Q(S_{\min}) = -Q_r$ (total volume transport equals river discharge) and $Q_s(S_{\min}) = 0$ (total salt transport vanishes under long-term averaging). The link to mixing is given by $Q_{s^2}(S_{\min}) = \mathbb{M}$ (total salinity-squared transport equals mixing), see details in Burchard et al. (2019). These properties of $Q(S)$, $Q_s(S)$, and $Q_{s^2}(S)$ are demonstrated for a cross-channel transect near the mouth of the Elbe River estuary in Fig. 2a,c,d, where nearly balanced conditions are given such that the respective deviations from the expected values at $S = S_{\max}$ are small.

Taking the S-derivative of (14) results in the volume, salinity and salinity-squared transport per salinity class (the Total Exchange Flow, TEF),

$$q(S) = -\frac{\partial Q(S)}{\partial S}, \quad q_s(S) = -\frac{\partial Q_s(S)}{\partial S}, \quad q_{s^2}(S) = -\frac{\partial Q_{s^2}(S)}{\partial S}, \tag{15}$$

where the minus sign ensures that inflow at high salinities is positive to highlight the character of the exchange flow. The connection to the Knudsen relations (18), (21) and (22) is given by separately integrating the positive and negative contributions (denoted by superscripts $^+$ and $^-$) of the transport per salinity class,

$$\begin{aligned} &Q_{\mathrm{in}} = \int\limits_{S_{\min}}^{S_{\max}} q^+(S)\,\mathrm{d}S, \qquad Q_{\mathrm{out}} = \int\limits_{S_{\min}}^{S_{\max}} q^-(S)\,\mathrm{d}S, \qquad Q_{s,\mathrm{in}} = \int\limits_{S_{\min}}^{S_{\max}} q_s^+(S)\,\mathrm{d}S, \quad Q_{s,\mathrm{out}} = \int\limits_{S_{\min}}^{S_{\max}} q_s^-(S)\,\mathrm{d}S, \\ &Q_{s^2,\mathrm{in}} = \int\limits_{S_{\min}}^{S_{\max}} q_{s^2}^+(S)\,\mathrm{d}S, \quad Q_{s^2,\mathrm{out}} = \int\limits_{S_{\min}}^{S_{\max}} q_{s^2}^-(S)\,\mathrm{d}S, \end{aligned} \tag{16}$$

and by deriving transport-weighted inflow and outflow salinities and squared salinities,

$$s_{\mathrm{in}} = \frac{Q_{s,\mathrm{in}}}{Q_{\mathrm{in}}}, \quad s_{\mathrm{out}} = \frac{Q_{s,\mathrm{out}}}{Q_{\mathrm{out}}}, \quad (s^2)_{\mathrm{in}} = \frac{Q_{s^2,\mathrm{in}}}{Q_{\mathrm{in}}}, \quad (s^2)_{\mathrm{out}} = \frac{Q_{s^2,\mathrm{out}}}{Q_{\mathrm{out}}}. \tag{17}$$

An exemplary TEF profile is found in Fig. 2b for the Elbe River estuary. Zero values for $q(S)$ occur for extreme values of $Q(S)$, in consistency with (15). For the two-layer exchange flow shown here, there is one unique maximum of $Q(S)$, such that the salinity S at which this occurs is the dividing salinity s_{div} between inflow and outflow (MacCready et al., 2018). Note that the dividing salinity s_{div} can also be used to calculate the Knudsen parameters Q_{in}, Q_{out}, s_{in}, and s_{out}, providing a numerically

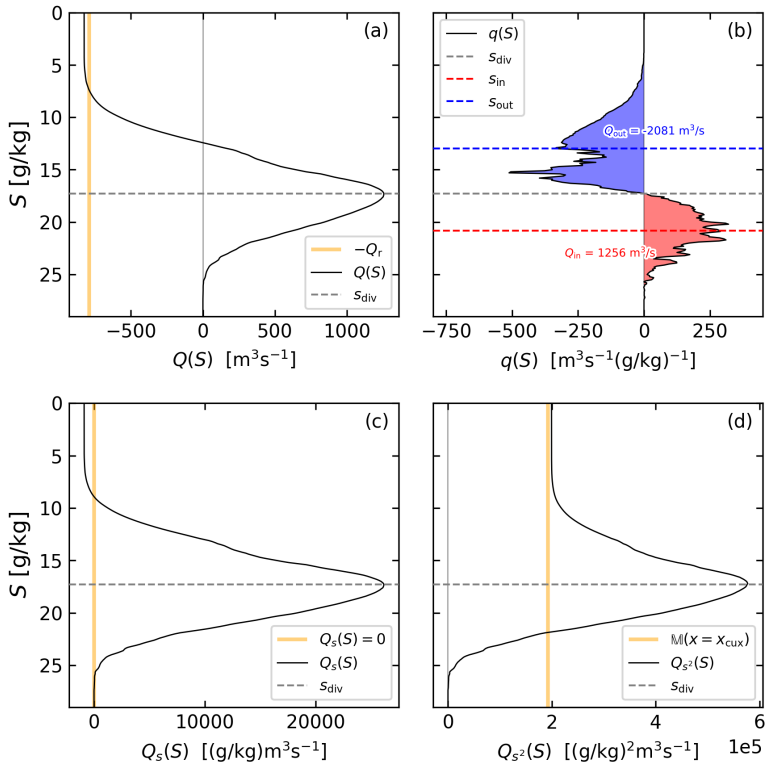

Figure 2. TEF analysis using numerical model data from a cross-channel transect at along-channel position x_{cux} at Cuxhaven near the mouth of the Elbe River estuary (see Fig. C1a), averaged for the full month of April 2024. (a) Volume transport $Q(S)$ across the transect, with the freshwater discharge Q_{r} and the dividing salinity s_{div} for reference. (b) Volume transport per salinity class, $q(S)$, as well as the bulk inflow and outflow salinities s_{in} and s_{out}, respectively. The shaded areas and written numbers correspond to the bulk volume inflow (Q_{in}, red) and bulk volume outflow (Q_{out}, blue). (c) Salinity transport $Q_s(S)$; (d) salinity-squared transport Q_{s^2} across the transect, with the integrated mixing within the estuarine volume bounded by the same transect, $\mathbb{M}(x = x_{\mathrm{cux}})$, for reference.

more robust method compared to the direct computation via (16) (Lorenz et al., 2019). For multi-layer flows, multiple dividing salinities may occur (Lorenz et al., 2019; Burchard et al., 2025).

The TEF analysis framework has been applied for a variety of estuarine studies, such as for tidal estuaries (MacCready, 2011; Chen et al., 2012; Wang et al., 2017; Conroy et al., 2020; Lemagie et al., 2022; Reese et al., 2024), tidal bays (Gräwe et al., 2016; Rayson et al., 2017; Xiong et al., 2021; Lemagie et al., 2022), non-tidal estuaries (Lange et al., 2020; Burchard et al., 2025), inverse estuaries (Lorenz et al., 2020), fjords (Sutherland et al., 2011; Lemagie et al., 2022; MacCready and Geyer, 2024), and regional seas (Döös et al., 2004; Burchard et al., 2018a).

3.3 Knudsen theory

To assess how entire estuaries quantitively act as mixing machines, the local relations derived in Sec. 2.2 are now integrated over estuarine volumes. For this, the continuity equation (3) and the salinity equation (4) are first integrated over the estuarine volume V which is separated from the ocean by means of a fixed vertical transect:

$$Q_{\rm in} + Q_{\rm out} + Q_r = \frac{{\rm d}V}{{\rm d}t}, \quad Q_{\rm in} s_{\rm in} + Q_{\rm out} s_{\rm out} = \frac{{\rm d}\left(\bar{s}V\right)}{{\rm d}t}, \tag{18}$$

(see Fig. 3a) with the inflow transport and representative salinity $Q_{\rm in} \geq 0$ and $s_{\rm in}$ (the ocean water inflow), outflow transport and representative salinity $Q_{\rm out} \leq 0$ and $s_{\rm out}$ (the brackish water outflow), as defined in (16) and (17). Further quantities in (18) are the river run-off $Q_r \geq 0$ (assuming zero river salinity for simplicity), the average salinity in the estuary, $\bar{s}$ and the volume-integrated salinity $\bar{s}V$. Details of the derivation of (18) are given in Burchard et al. (2019). The conservation laws (18) have already been formulated by Knudsen (1900) and have become the basis for analyses of exchange flow in many estuaries (see e.g., Ji et al., 2007; MacCready, 2011; Sutherland et al., 2011; Chen et al., 2012; Burchard et al., 2018a). The positioning of the transect that separates the estuarine volume from the ocean is arbitrary, but often the geographical location of the river mouth is chosen. In (18) freshwater transports across the surface (evaporation or precipitation), the bottom (submarine groundwater discharge) as well as horizontal diffusive salt transports across the transect are neglected. Relations including freshwater transport through the sea surface can be found in Lorenz et al. (2021). Under long-term averaged conditions, the volume and salt storage terms on the right-hand side of (18) would vanish. Under such circumstances, $s_{\rm out} \leq s_{\rm in}$ and $Q_{\rm in} \leq -Q_{\rm out}$ must hold, as illustrated for the Elbe estuary in Fig. 4a,b, where balanced conditions with a nearly vanishing volume storage $\frac{{\rm d}V}{{\rm d}t}$ are given. Under such circumstances, inflow from the ocean occurs at higher salinities than outflow towards the ocean due to mixing with riverine water.

The bulk mixing of an estuary is then obtained by averaging the integrated salinity variance budget (B2) in time:

$$\frac{\rm d}{{\rm d}t} \int\limits_V s'^2_{\rm tot} {\rm d}V \approx Q_r \bar{s}^2_{\rm tot} + Q_{\rm in}(\bar{s}_{\rm tot} - s_{\rm in})^2 + Q_{\rm out}(\bar{s}_{\rm tot} - s_{\rm out})^2 - \mathbb{M}, \tag{19}$$

with the estuarine bulk mixing

$$\mathbb{M} = \left\langle \int\limits_V \chi_s \, {\rm d}V \right\rangle, \tag{20}$$

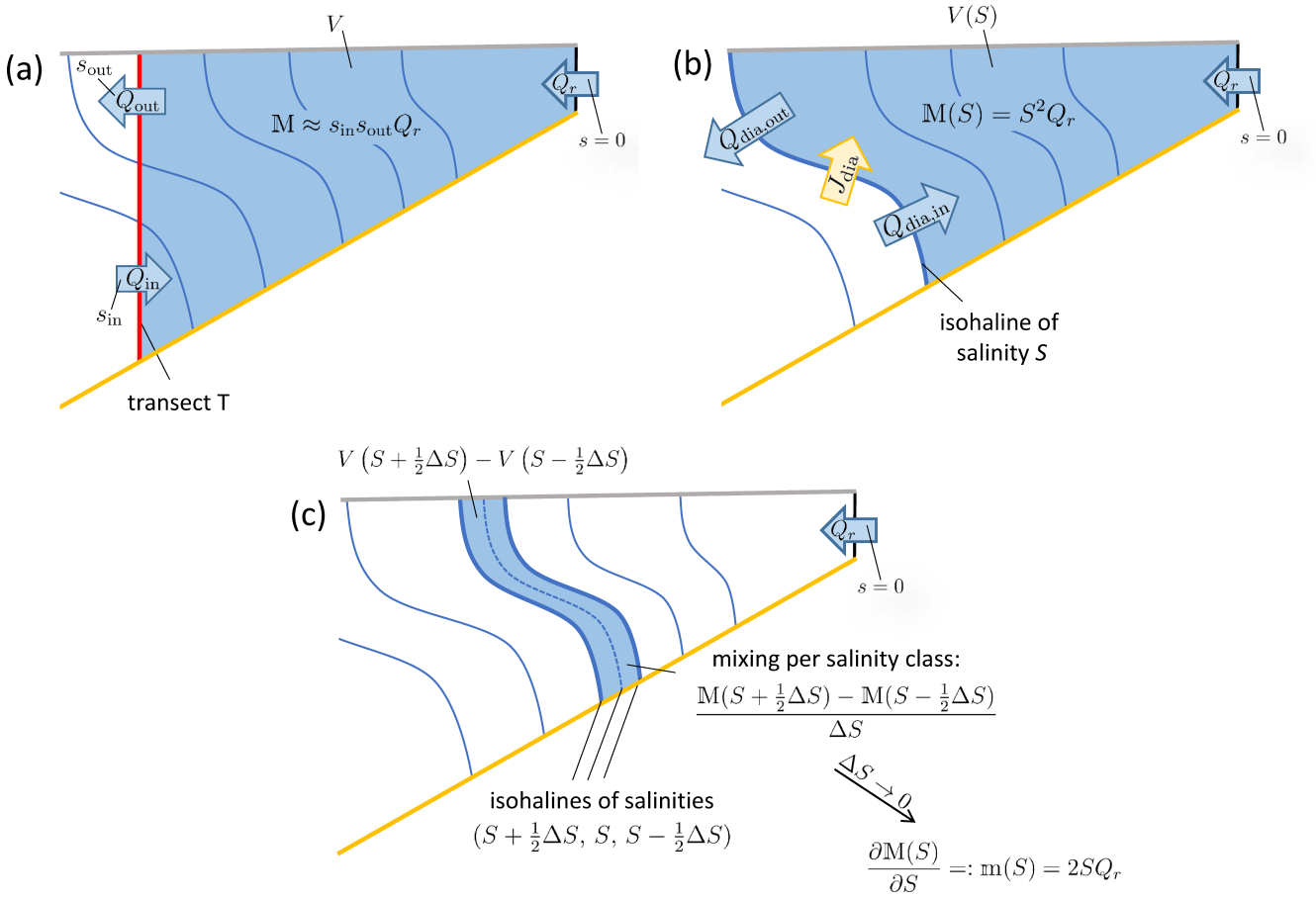

Figure 3. Sketch showing the principles of volume and salt conservation as well as mixing in estuaries: (a) Estuarine volume (light blue shading) bounded by a fixed transect (bold red line), showing the classical Knudsen (1900) transports and salinities as well as the Knudsen mixing law (21) as derived by MacCready et al. (2018). (b) Estuarine volume (light blue shading) bounded by an isohaline of salinity S (bold blue line), showing the diahaline advective (Q_{dia}) and diffusive transports (J_S) as well as the mixing law (32) as derived by Burchard (2020). (c) Envelope of a discrete estuarine sub-volume (light blue shading) around the isohaline of salinity S (dashed blue line), bounded by the isohalines of salinities $S + \frac{1}{2}\Delta S$ and $S - \frac{1}{2}\Delta S$ (bold blue lines). The mixing per discrete salinity class is shown as well as the limit for $S \to 0$ which results in the universal law of estuarine mixing (33) for an infinitesimally thin salinity class. The bottom is marked by an orange line, the surface by a grey line and the fixed river transect by a red line. Advective volume transports are marked by blue arrows and the diffusive salt transport is marked by a yellow arrow.

see the derivations by MacCready et al. (2018) and Burchard et al. (2019). In (19), the approximations $(s^2)_{\rm in} \approx (s_{\rm in})^2$ and $(s^2)_{\rm out} \approx (s_{\rm out})^2$ have been made for simplicity, where $(s^2)_{\rm in}$ and $(s^2)_{\rm out}$ are inflowing and outflowing salinity squares, respectively, as defined in (17). Assuming long-term averaging such that the temporal derivatives vanish and using (18), we finally obtain

$$\mathbb{M} \approx Q_{\rm in} s_{\rm in}^2 + Q_{\rm out} s_{\rm out}^2 = s_{\rm in} s_{\rm out} Q_r = (s_{\rm in} - s_{\rm out}) s_{\rm in} Q_{\rm in}, \tag{21}$$

(MacCready et al., 2018), relating the Knudsen parameters directly to estuarine mixing. While Knudsen (1900) had mentioned the role of mixing for the estuarine exchange flow qualitatively, (21) gave the first quantitative estimate of estuarine mixing as a function of the Knudsen parameters. An accurate bulk mixing estimate allowing $(s^2)_{\rm in} \neq (s_{\rm in})^2$ and $(s^2)_{\rm out} \neq (s_{\rm out})^2$ has been derived by Burchard et al. (2019):

$$\mathbb{M} = \frac{s_{\rm out}(s^2)_{\rm in} - s_{\rm in}(s^2)_{\rm out}}{s_{\rm in} - s_{\rm out}} Q_r. \tag{22}$$

For the special case of $(s^2)_{\rm in} = (s_{\rm in})^2$ and $(s^2)_{\rm out} = (s_{\rm out})^2$, (21) is identical to (22). These equalities are only exact when the inflowing and outflowing salinities are constant in time and space during the averaging interval (Burchard et al., 2019). For estuaries with strongly fluctuating salinities at the mouth (such as for the short Merrimack estuary, see Chen et al., 2012) relation (22) has to be used instead of (21) to obtain an accurate estimate for the mixing.

Relation (21) is demonstrated in Fig. 4c for a numerical simulation of the Elbe estuary. It can be seen that the estimate is near-exact for almost the entire length of the estuary, proving its value for the study of bulk mixing in realistic estuaries, as also tested in studies by Broatch and MacCready (2022) and Reese et al. (2024).

The principle of salt mixing inside an estuary bounded by a fixed transect is sketched in Fig. 3a. The first relation of (21) shows that the mixing does also balance the exchange of squared salinity with the ocean, such that mixing can also be defined as the reduction of squared salinity integrated over the estuary (which often simplifies the calculations, see Burchard et al., 2019), as it is expressed locally in (B3). The second relation of (21) shows that estuarine mixing can be estimated simply by knowing inflowing and outflowing salinities and the river run-off (MacCready et al., 2018). The third relation of (21) demonstrates the relation between estuarine circulation (quantified as strength of $Q_{\rm in}$, see Broatch and MacCready, 2022; MacCready and Geyer, 2024) and mixing, a topic that is expanded on in Sec. 3.6.

Using the Knudsen relations (18), yet another useful reformulation of (21) has been derived by Qu et al. (2022) for estuaries in which the riverine inflow has non-zero salinity:

$$\mathbb{M} \approx Q_r (s_r - s_{\rm out})^2 + Q_{\rm in} (s_{\rm in} - s_{\rm out})^2, \tag{23}$$

which is identical to (21) for a river salinity of $s_r = 0$. In (23), the right-hand side is split into two terms representing the *mixing pathways* from the inflows to the outflows, with the first one leading from the river inflow to the brackish water outflow and the second one leading from the seawater inflow to the brackish water outflow (with source-water salinities put first in the brackets).

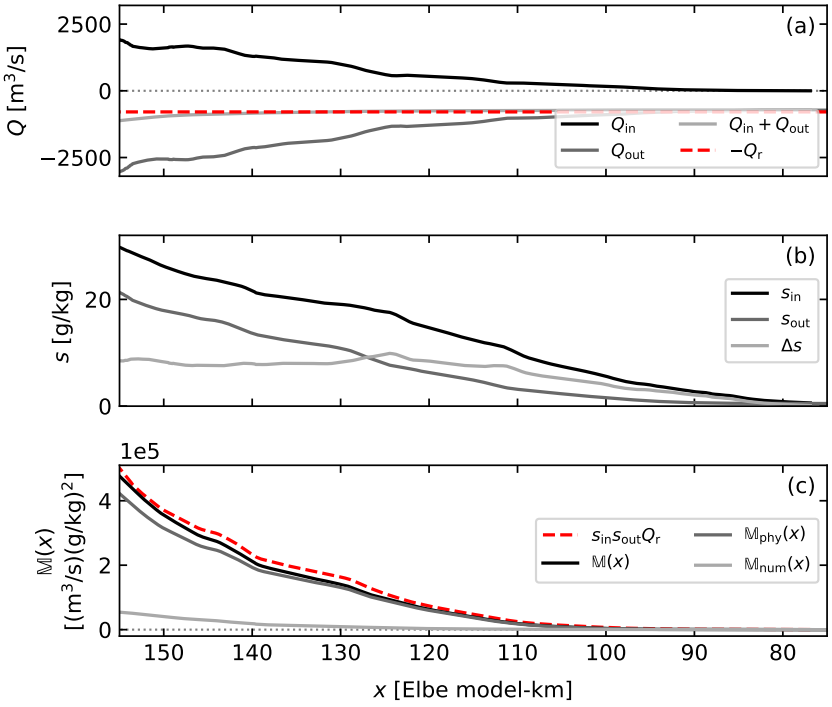

Figure 4. Bulk parameters of the exchange flow through cross-channel transects at each along-channel position x from a numerical simulation of the Elbe River estuary, averaged for the month of April 2024. (a) Volume inflow and outflow Q_{in} and Q_{out}, respectively, compared to the freshwater discharge Q_{r}. (b) Inflow and outflow salinities s_{in} and s_{out}, respectively, as well as their difference $\Delta s = s_{\mathrm{in}} - s_{\mathrm{out}}$. (c) Integrated mixing $\mathbb{M}(x)$ within the estuarine volume bounded by a cross-channel transect at along-channel position x, split into the contributions of the physical mixing $\mathbb{M}_{\mathrm{phy}}$ due to the mixing parameterisation as well as the numerical mixing $\mathbb{M}_{\mathrm{num}}$ due to discretization errors. The directly computed mixing (solid lines) is compared to the mixing estimate (21).

The Knudsen mixing relation (21) has been extended by Lorenz et al. (2021) for the case of non-zero freshwater fluxes through the surface, i.e., precipitation and evaporation:

$$\mathbb{M} \approx s_{\mathrm{in}} s_{\mathrm{out}} (Q_r + Q_{\mathrm{surf}}) - s_{\mathrm{surf}}^2 Q_{\mathrm{surf}}, \tag{24}$$

with the surface freshwater transport Q_{surf} (positive for net precipitation) and the representative surface salinity s_{surf} (square root of surface salinity variance transport divided by $-Q_{\mathrm{surf}}$). Since $s_{\mathrm{surf}} > (s_{\mathrm{in}} s_{\mathrm{out}})^{1/2}$ for evaporation and $s_{\mathrm{surf}} < (s_{\mathrm{in}} s_{\mathrm{out}})^{1/2}$ for precipitation, both evaporation and precipitation are sources of mixing, in addition to the exchange flow. The example of the Persian Gulf as an inverse estuary with strong evaporation is briefly discussed in Sec. 4.1.3.

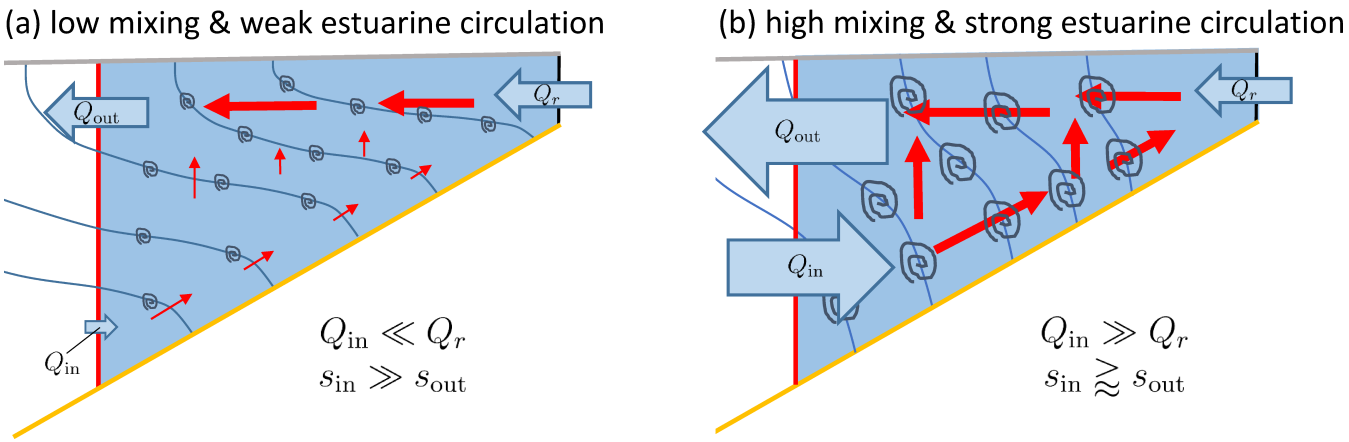

Figure 5. Sketch showing estuarine conditions for low mixing causing weak estuarine circulation (panel a) and high mixing causing strong estuarine circulation (panel b). In both panels, Q_r and s_{in} are supposed to be identical. With prescribed low mixing $\mathbb{M}$ in panel a and a high mixing $\mathbb{M}$ in panel b, the Knudsen relations (18) and (21) quantify Q_{in}, Q_{out} and s_{out}.

For the interpretation of the mixing relations it is instructive to consider the mixing completeness Mc (Burchard et al., 2019) by non-dimensionalising (21) using Q_r and s_{in}:

$$\text{Mc} = \frac{\mathbb{M}}{s_{\text{in}}^2 Q_r} \approx \frac{s_{\text{out}}}{s_{\text{in}}}, \tag{25}$$

where the river run-off Q_r and inflowing salinity s_{in} (sometimes equated to the ocean salinity) can be considered as the external forcing of the estuary. Mixing completeness in estuaries can cover the full range of theoretically possible values of $0 \leq \text{Mc} \leq 1$. Tab. 1 gives a number of examples for estuarine systems with low, medium and high mixing completeness. It should be noted that the mixing completeness is always calculated with respect to a fixed transect and that for each estuarine system the mixing completeness varies strongly with discharge and tidal intensity (e.g., during the spring-neap cycle).

In the extreme case of no mixing, the riverine freshwater would flow out at the surface with no modification and no ocean water entering the system ($s_{\text{out}} = 0$ and $Q_{\text{in}} = 0$), such that the mixing completeness would be zero. In estuaries with low mixing, brackish water of only low salinity is produced, with $s_{\text{out}} \ll s_{\text{in}}$ and $Q_{\text{in}} \ll Q_r$, such that the mixing completeness is $s_{\text{out}}/s_{\text{in}} \ll 1$, see sketch in Fig. 5a. This would theoretically be the case for deep fjords with low tidal energy (Inall and Gillibrand, 2010). Mostly, fjords do however have large water bodies and low discharge such that the freshwater is strongly diluted by tidal mixing as, for example, for the Puget Sound where the mixing completeness is as large as about 0.97 (see Sutherland et al., 2011, and Tab. 1). Low mixing values of about $\text{Mc} = 0.18$ have been observed for the tidally intense Merrimack estuary during high discharge (see Chen et al., 2012). Under these conditions, the salt intrusion length shortens considerably such that high-salinity ocean water and low-salinity river water are in close contact at the mouth of this estuary discharging directly into the coastal ocean, leading to low mixing. Other low values of mixing completeness are also observed for the Hudson river estuary during neap tide ($\text{Mc} = 0.36$, see Wang et al., 2017) and the Elbe River estuary at high discharge ($\text{Mc} = 0.37$, see

Reese et al., 2024). In both cases, the water is relatively strongly stratified in the region of the transect such that $s_{\rm out} \ll s_{\rm in}$. The large variability that estuaries have due to changes in discharge and tidal intensity is demonstrated by the fact that the Elbe for low discharge, the Merrimack for low discharge, and the Hudson for spring show values of mixing completeness as high as $\mathrm{Mc} = 0.75$, $\mathrm{Mc} = 0.86$ and $\mathrm{Mc} = 0.87$, respectively. Almost complete mixing is obtained for the shallow Wadden Sea of the German Bight, as sketched in Fig. 5b. In the Sylt-Rømø-Bight, where the freshwater run-off is low and tidal mixing is high, Gräwe et al. (2016) calculated values of inflowing and outflowing salinity both > 30 g/kg with only about 1 g/kg difference, such that the mixing compleness is about $\mathrm{Mc} = s_{\rm out}/s_{\rm in} \approx 30/31 \approx 0.97$. These are values comparable to Puget Sound, see above. For the Baltic Sea, a non-tidal semi-enclosed sea in northern Europe, Knudsen (1900) estimated $s_{\rm in} = 17.4$ g/kg and $s_{\rm out} = 8.7$ g/kg, such that the mixing completeness is $\mathrm{Mc} = 0.5$, a value that could be confirmed by a multi-decadal model simulation (Burchard et al., 2018a, 2019).

Table 1. List of estuarine systems with typical values of mixing completeness Mc for different tidal and runoff conditions. Note that estuaries with strong temporal variation (e.g., the Hudson River estuary during the spring-neap cycle) are not in balance, such that (25) is only a rough approximation.

Name of estuary	position of transect	mixing completeness Mc	Reference
Merrimack (high discharge)	jetties	0.18	Chen et al. (2012)
Hudson (neap tide)	Battery	0.36	Wang et al. (2017)
Elbe (high discharge)	Cuxhaven	0.37	Reese et al. (2024)
Columbia (spring-neap cycle)	Cape Disappointment	0.45	MacCready (2011)
Baltic Sea (observed)	Darss Sill	0.50	Knudsen (1900)
Baltic Sea (simulated)	Darss & Drogden Sill combined	0.54	Burchard et al. (2018a, 2019)
Elbe (low discharge)	Cuxhaven	0.75	Reese et al. (2024)
Merrimack (low discharge)	jetties	0.86	Chen et al. (2012)
Hudson (spring tide)	Battery	0.87	Wang et al. (2017)
Puget Sound (spring-neap average)	Admiralty Inlet North	0.97	Sutherland et al. (2011)
Wadden Sea (Sylt-Rømø Bight)	tidal gulley	0.97	Gräwe et al. (2016)

3.4 Water Mass Transformation and diahaline mixing

Often, it is instructive to consider dynamics of estuaries in an isohaline framework, i.e., to evaluate transports, mixing and other properties relative to moving surfaces of constant salinity (isohalines) instead of the Eulerian framework with fixed spatial coordinates. With this, a quasi-Lagrangean perspective is added to the analysis with reference to the moving flow. In the isohaline analysis, geographical features such as a fixed transect at the mouth of the estuary do not play a central role. Since isohalines can move inside and outside the estuarine water body and extend over large areas covering parts of the estuary and the river plume, the isohaline analysis treats estuary and river plume as a dynamic continuum. This isohaline view of

estuarine dynamics was first proposed by Walin (1977), with specific reference to the Baltic Sea with its isohalines extending over up to 1000 km from the Central Baltic Sea to its Western reaches (Henell et al., 2023). Later, the isohaline concept was applied to tidal estuaries (MacCready and Geyer, 2001; MacCready et al., 2002; Wang et al., 2017) and river plumes (Hetland, 2005; Muche et al., 2026). Here, we first introduce a local diahaline analysis, before we discuss the bulk analysis of estuarine dynamics across isohaline surfaces in Sec. 3.5.

Local mixing can move isohaline surfaces vertically such that a diahaline mass transport occurs relative to the moving isohaline surface. When normalised to isohaline unit surface and unit mass, this results in a so-called entrainment velocity. Starting for explanation with the one-dimensional salinity budget equation (D3), a coordinate transformation from geopotential z to salinity coordinates s (assuming a stable salinity stratification with $\partial s/\partial z < 0$), after time averaging in salinity coordinates, $\langle\cdot\rangle_S$, a formulation for the vertical entrainment velocity $u_{\mathrm{dia},z}(S)$ (vertical velocity relative to the vertically moving isohaline) is obtained:

$$u_{\mathrm{dia},z}(S) = \left\langle w - \frac{\partial z}{\partial t} \right\rangle_S = \frac{\partial}{\partial S} \left\langle K_v \frac{\partial S}{\partial z} \right\rangle_S = -\frac{\partial j_{\mathrm{dia},z}(S)}{\partial S} \tag{26}$$

(Wang et al., 2017; Klingbeil and Henell, 2023), where $j_{\mathrm{dia},z}(S)$ is the time-averaged upward salinity flux through the moving isohaline. The vertical velocity of the isohaline S due to both advection and turbulent diffusion is given by $\partial z/\partial t$ (with z being the vertical position of the isohaline). Details of the derivation of (26) is given in (D1) - (D3). The meaning of (26) is sketched in Fig. 6a: there is a maximum of vertical turbulent salinity flux $j_{\mathrm{dia},z}$ in the entrainment layer that caps the turbulent bottom boundary layer. This maximum results from a large vertical salinity gradient $|\partial s/\partial z|$ at a still high level of turbulence originating from the boundary layer, expressed as eddy diffusivity K_v. Below this maximum, vertical salinity flux is divergent, thus lowering the local salinity which in time-average leads to an upward entrainment velocity $u_{\mathrm{dia},z}$. Above the entrainment layer, the opposite happens, resulting in a downward salinity flux. A similar process has been described and sketched by Ferrari et al. (2016), using density fluxes near the bottom of the ocean. The exchange flow in the bottom boundary layer itself with upwelling near the bottom and downwelling above has already been described by Garrett (1991). It should be noted that the total diahaline salt flux consists of two contributions, with one advective contribution and one diffusive contribution:

$$f_{\mathrm{dia},z}(S) = u_{\mathrm{dia},z}(S)S + j_{\mathrm{dia},z}(S) = -\frac{\partial j_{\mathrm{dia},z}(S)}{\partial S} S + j_{\mathrm{dia},z}(S), \tag{27}$$

with the consequence that volume flux and salt flux are not proportional to each other and that the distribution of the diffusive salt flux in salinity coordinates entirely determines the total diahaline salt flux.

To relate $j_{\mathrm{dia},z}$ to mixing χ_s, Li et al. (2022) defined the local mixing per salinity class which for a vertical water column with a monotone salinity profile reads as

$$m(S) = \left\langle -\frac{\partial z}{\partial S}\chi_s \right\rangle_S = \left\langle -\frac{\partial z}{\partial S} 2K_v \left(\frac{\partial S}{\partial z}\right)^2 \right\rangle_S = 2\left\langle -K_v \frac{\partial S}{\partial z} \right\rangle_S = 2j_{\mathrm{dia},z}(S). \tag{28}$$

which can be seen as a thickness-weighted time-average of the local mixing χ_s, see also Klingbeil et al. (2019), Burchard et al. (2021) and Li et al. (2022). Combining (26) and (28) results in a key relation between entrainment velocity and mixing,

$$u_{\mathrm{dia},z}(S) = -\frac{1}{2}\frac{\partial m(S)}{\partial S}, \tag{29}$$

which could be called the diahaline mixing-entrainment relation. Note that here upward velocities $u_{\mathrm{dia},z}$ and fluxes $j_{\mathrm{dia},z}$ are denoted as positive quantities. Details of the derivation of (29) for non-monotone salinity distributions in three dimensions can be found in Klingbeil and Henell (2023). The principle of (29) is sketched in Fig. 6b: as given by (28), m has local maxima in the same locations as $j_{\mathrm{dia},z}$, i.e., in the entrainment layers. For mixing per salinity class increasing with height, $\partial m/\partial z > 0 \Leftrightarrow \partial m/\partial S < 0$ (for stable salinity stratification), a positive entrainment velocity $u_{\mathrm{dia},z} > 0$ is expected. For mixing decreasing with height, the opposite occurs. This leads to a typical pattern of diahaline exchange flow in estuaries with positive (upward, towards lower salinities into the estuary) entrainment through an isohaline near the bottom, and a negative (downward, towards higher salinities out of the estuary) entrainment through the same isohaline near the surface further seawards. For realistic estuaries this has been shown for the Hudson River estuary (Wang et al., 2017), the Pearl River estuary (Li et al., 2022, 2024), the Elbe River estuary (Reese et al., 2024), the Changjiang River estuary (Chang et al., 2024) and the Baltic Sea (Henell et al., 2023). In particular, Henell et al. (2023) and Reese et al. (2024) calculated both sides of (29) independently to demonstrate their equality (aside from small numerical differences) in real-world estuarine systems. The advantage of (29) over (26) is given by the fact that χ_s and thus m can be split into physical and numerical contributions (see Sec. 5.2.2), such that numerically generated spurious entrainment can be calculated, as shown by Henell et al. (2023) for the Baltic Sea.

The relationship between diahaline mixing m and entrainment velocity $u_{\mathrm{dia},z}$ across the isohaline of 11 g/kg is shown in Fig. 7 for the Elbe River estuary in northern Germany. It is clearly visible that as stated in (29), entrainment requires mixing since hotspots of the two quantities align well. In the up-estuary reach of the isohaline surface, where it is close to the bottom, upwelling (red) dominates, whereas at the down-estuary near-surface reaches of the isohaline downwelling (blue) dominates.

3.5 Estuarine mixing in isohaline volumes

Local diahaline mixing as introduced in Sec. 3.4 can be expanded to estuarine volumes (Walin, 1977). The local relation (27) for the total diahaline salt flux $f_{\mathrm{dia},z}(S)$ can be integrated over the entire isohaline surface to result in

$$F_{\mathrm{dia}}(S) = Q_{\mathrm{dia}}(S)S + J_{\mathrm{dia}}(S) = -\frac{\partial J_{\mathrm{dia}}(S)}{\partial S}S + J_{\mathrm{dia}}(S), \tag{30}$$

where F_{dia} is the total salt transport, $Q_{\mathrm{dia}} < 0$ is the diahaline volume transport, and $J_{\mathrm{dia}} > 0$ is the diffusive salt transport across the isohaline surface (see Fig. 8a by Walin, 1977). If instead of a fixed transect T a moving isohaline of salinity S is considered as the seaward boundary of the estuary (see Fig. 3b), the volume and salt budget is of this form:

$$Q_{\mathrm{dia,in}}(S) + Q_{\mathrm{dia,out}}(S) + Q_r = \frac{\mathrm{d}V(S)}{\mathrm{d}t}, \quad \left(Q_{\mathrm{dia,in}}(S) + Q_{\mathrm{dia,out}}(S)\right)S + J_{\mathrm{dia}}(S) = \frac{\mathrm{d}(\bar{s}_{\mathrm{tot}}V(S))}{\mathrm{d}t}, \tag{31}$$

with the isohaline volume $V(S)$, the average salinity inside this volume $\bar{s}_{\mathrm{tot}}$, the net advective inflow through the isohaline, $Q_{\mathrm{dia,in}} > 0$, and the the net advective outflow through the isohaline, $Q_{\mathrm{dia,out}} < 0$. Transformations of (31) show that long-term averaged mixing inside the estuarine volume bounded by an isohaline S is

$$\mathbb{M}(S) = \int\limits_{V(S)} \chi_s \,\mathrm{d}V = S^2 Q_r, \tag{32}$$

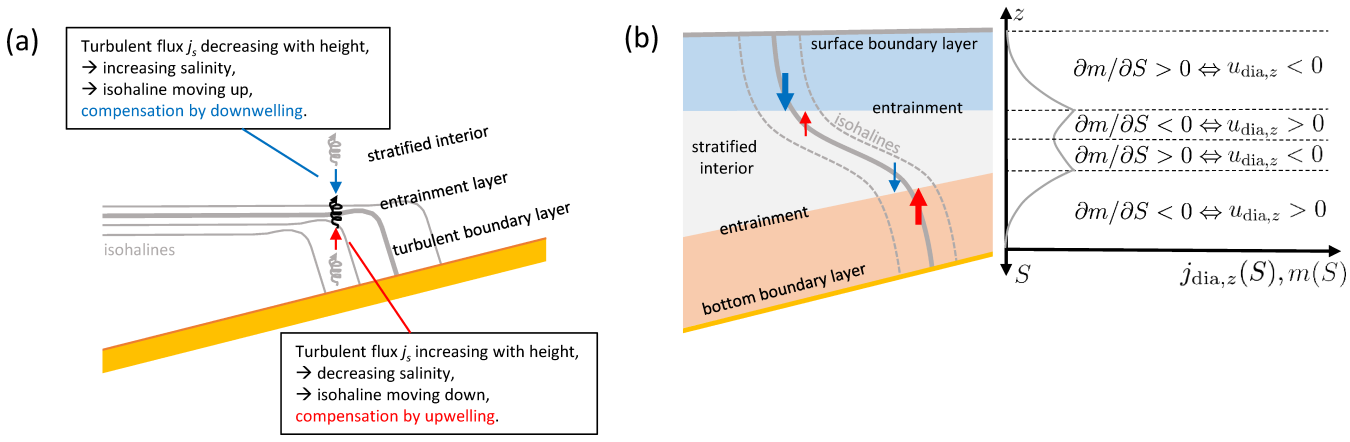

Figure 6. Sketch demonstrating the mechanism and distribution of diahaline exchange flow in estuaries. (a) Generation of diahaline exchange flow by means of a divergent vertical turbulent salinity flux $j_{\mathrm{dia},z}$, according to (26), shown for the bottom boundary layer of an estuary. High values of $j_{\mathrm{dia},z}$ are marked by a black whirl, and low values are marked by grey whirls. The entrainment velocity is marked as red (upwards, $u_{\mathrm{dia},z} > 0$) and blue (downwards, $u_{\mathrm{dia},z} < 0$) arrows. (b) Situation of time-averaged diahaline exchange in an estuary. The bottom boundary layer and the surface boundary layer are marked by colour, both being separated from a more stratified interior via entrainment layers. Three exemplary isohalines are drawn. The entrainment velocity is again marked as red and blue arrows, where the size of the arrows corresponds to its relative magnitude. On the right side of the sketch a typical profile of the local mixing per salinity class $m(S)$ is shown, along with consistent signs of the entrainment velocity $u_{\mathrm{dia},z}$, according to (29).

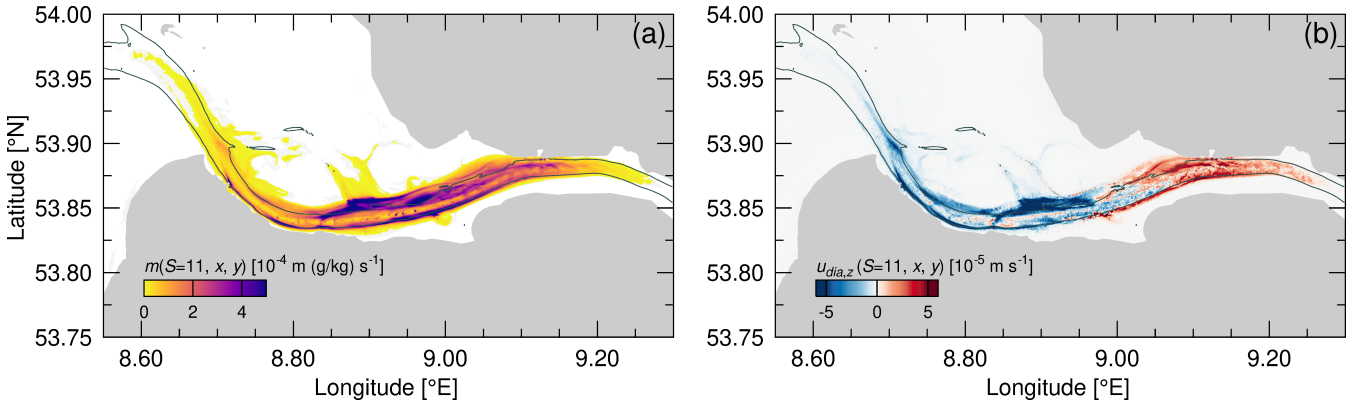

Figure 7. Diahaline mixing m (panel a) and diahaline entrainment velocity $u_{\mathrm{dia},z}$ (panel b) across the isohaline surface of 11 g/kg, averaged over two spring-neap cycles during April 2024 in the lower Elbe River estuary in Germany. The line in both panels shows the 10 m isobath.

which can be seen as a special case of $\mathbb{M} \approx s_{\mathrm{in}} s_{\mathrm{out}} Q_r$ from (21) with $s_{\mathrm{in}} = s_{\mathrm{out}} = S$ (Burchard, 2020). The relation (32) is exact for long-term averaging and zero freshwater transports through the surface and bottom of the estuary. A mixing relation for non-zero river salinity is shown in (F28).

With $\mathbb{M}(S)$ being a continuous function of S and assuming that Q_r is independent of S, we can take the derivative of $M(S)$ with respect to S:

$$\mathbb{m}(S) = \frac{\partial \mathbb{M}(S)}{\partial S} = 2SQ_r, \tag{33}$$

where $\mathbb{m}(S)$ is the salt mixing per salinity class. It should be noted that $\mathbb{m}(S)$ can also be obtained by integrating the local mixing per salinity class $m(S)$ from (29) over the projection of the isohaline surface to the horizontal (Li et al., 2022). A discrete version of (33) is sketched in Fig. 3c in order to explain the infinitesimal property of the mixing per salinity class. The linear dependence of $\mathbb{m}(S)$ on salinity S has been formulated and derived as the *universal law of estuarine mixing* (Burchard, 2020).

The relation (33) can be explained by first stating that the volume transport across the isohaline must for long-term averaged conditions equal the river runoff Q_r. Furthermore, the advective salt transport across the isohaline, $-S(Q_{\mathrm{dia,in}} + Q_{\mathrm{dia,out}}) = SQ_r$, must equal the diahaline diffusive salt transport, such that $J_{\mathrm{dia}}(S) = SQ_r$, see the second equation in (31). With

$$\mathbb{m}(S) = 2J_{\mathrm{dia}}(S), \tag{34}$$

which can be derived by integration of (28) over the horizontal projection of the isohaline surface, relation (33) is obtained (Burchard et al., 2021). A relation equivalent to the combination of (33) and (34) had been derived by Hetland (2005), based on earlier work of Garvine (1999), to quantify the turbulent salt transport into river plumes due to entrainment, see the steady-state version of his equation (4).

To accurately reproduce the universal law by means of models of realistic estuaries such as the Pearl River estuary (Li et al., 2022), the Changjiang River estuary (Chang et al., 2024) and the Elbe River estuary (Reese et al., 2024) averaging over one spring-neap cycle is typically sufficient. In a numerical model, the mixing which a salinity field experiences is the sum of the parameterised physical mixing $\mathbb{m}_{\mathrm{phy}}(S)$ and spurious numerical mixing $\mathbb{m}_{\mathrm{num}}(S)$ due to the discretisation of the advection operator, see Sec. 5.2.2 for details. Both, relations (32) and (33), are tested for the Elbe estuary in Fig. 8. There, it can be seen that the directly computed total mixing quantities $\mathbb{M}(S)$ and $\mathbb{m}(S)$, each consisting of the sum of numerical and physical mixing, closely follow their respective relation up to the point where the isohaline surfaces partly leave the model domain through the open boundary (grey-shaded areas in the Figure). Here, we first find an underestimation of the predicted mixing by relations (32) and (33) which can likely be related to left-over stratification in the German Bight from earlier high-discharge periods entering the model domain via the open boundary and then being mixed away. For very high salinity classes, the mixing in the model is much weaker than the predicted mixing since substantial parts of the isohaline surfaces are outside of the model domain such that most of the potential mixing is not covered by the model. While the Knudsen mixing law (21) is only valid when salinity fluctuations at the open boundary are limited, the universal law of estuarine mixing, (32) and (33), is exact for all estuaries (without relevant freshwater fluxes across the sea surface).

One interesting consequence of the universal law of estuarine mixing can be seen by reformulating (33) as

$$\mathbb{m}(S) = \mathbb{v}(S)\bar{\chi}_s(S) = 2SQ_r, \tag{35}$$

where $\mathbb{v}(S)$ is the volume per salinity class and $\bar{\chi}_s(S)$ is the salinity mixing averaged over the salinity class S. Since for long-term averages $\mathbb{v}(S)\bar{\chi}_s(S)$ is fixed, (35) means that at low mixing rates $\bar{\chi}_s(S)$ the volumes per salinity class should be large, with the consequence that at low mixing rates, isohaline spacing should be wide. When comparing for example the salinity fields for the Hudson River estuary for neap tide and for spring tide (Warner et al., 2005a), the isohaline spacing at springs is wider than at neaps. Assuming that storage terms do not play an essential role for these situations, the conclusion could be drawn that average mixing is smaller at springs than at neaps. This is consistent with the findings of Warner et al. (2020) who find that maximum mixing occurs during late neap tides, see also Sec. 4.1.2. This is also in line with the study of Garvine (1999) who showed that increased (background) diffusivity would reduce the area of a river plume (see also the river plume study by Li et al., 2024, who showed that additional mixing due to islands in the plume region can reduce the plume area and volume).

3.6 Relating estuarine circulation to mixing

In his famous abyssal recipes Munk (1966) fitted a vertical one-dimensional advection-diffusion equation to hydrographic observations in the central Pacific Ocean and concluded that turbulent mixing with an effective vertical diffusivity of $1.3 \cdot 10^{-4}\mathrm{m}^2\mathrm{s}^{-1}$ would be needed to explain the global overturning circulation. In later studies, the decomposition of the underlying mixing processes into wind and tidal mixing and their regional distribution had been further specified (see e.g., Munk and Wunsch, 1998; Kuhlbrodt et al., 2007; Nikurashin and Ferrari, 2011; Cessi, 2019). On the much smaller scales of estuaries, the same must be postulated: estuarine circulation requires mixing and vice versa. Here, we discuss different concepts of this duality.

Let us first summarise what we have discussed about this issue until now. In his fundamental paper, Knudsen (1900) already stated that estuarine circulation is associated with mixing (Sec. 1). The general process is that salty ocean water entering the estuary is first mixed with fresh river water inside the estuary and then ejected as brackish water towards the ocean, making estuaries mixing machines (MacCready and Banas, 2011; Wang et al., 2017). When there is no mixing inside the estuary, then no further salty water can enter the estuary in the long term (Sec. 3.3). In that sense, the volume transport of salty water flowing into the estuary, Q_{in}, is a good measure for the estuarine circulation (Broatch and MacCready, 2022; MacCready and Geyer, 2024). A first quantitative estimate for the tight relationship between estuarine circulation and mixing has been established in the third relation of (21) by MacCready et al. (2018), showing a proportionality between the bulk mixing M and Q_{in}, with $(s_{\mathrm{in}} - s_{\mathrm{out}})s_{\mathrm{in}}$ as factor of proportionality.

The streamfunction $Q(S)$ of the estuarine circulation as defined in (14) is the time-averaged volume transport into the estuary across a fixed transect for all salinities above S and therefore contains the information about the Total Exchange Flow, see Sec. 3.2 for details. It can be directly linked to mixing, as derived already by Walin (1977) to quantify the overturning circulation

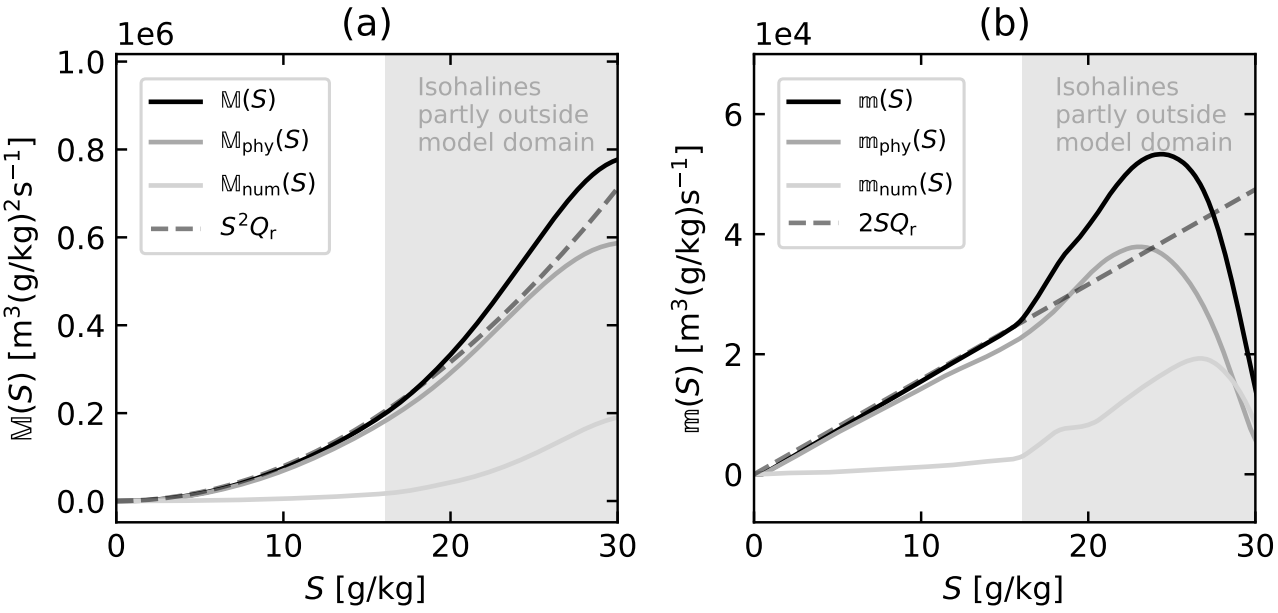

Figure 8. Salt mixing from a realistic numerical simulation of the Elbe River estuary, averaged for the full month of April 2024. (a) Integrated mixing $\mathbb{M}(S)$ within an estuarine volume bounded by an isohaline surface of salinity S as computed directly from numerical model data (solid black line) as well as from the freshwater discharge Q_r using equation (32) (dashed line). (b) Mixing per salinity class $\mathbb{m}(S)$ as computed directly from numerical model data (solid black line) as well as from the universal law of estuarine mixing, (33) (dashed line). In each panel, the respective contributions of the physical mixing $\mathbb{M}_\mathrm{phy}$ and $\mathbb{m}_\mathrm{phy}$ due to the mixing parameterisation as well as the numerical mixing $\mathbb{M}_\mathrm{num}$ and $\mathbb{m}_\mathrm{num}$ due to discretisation errors to the total diagnosed mixing are shown as solid grey lines.

of the Baltic Sea to mixing:

$$Q(S) = Q_\mathrm{dia,est}(S) = -\frac{\partial J_\mathrm{dia,est}(S)}{\partial S} = -\frac{1}{2}\frac{\partial \mathbb{m}_\mathrm{est}(S)}{\partial S}, \tag{36}$$

where the subscript $_\mathrm{est}$ means that diahaline transport Q_dia, diahaline salt flux J_dia and diahaline mixing per salinity class $\mathbb{m}$ are only considered for the part of the isohaline that is located on the estuarine side of the transect, see Fig. 9. The first equality in (36) is demonstrated in Fig. 9a: under long-term averaged conditions the volume transport $Q(S)$ into the subvolume bounded by the transect T, the isohaline S and the bottom must be equal to the volume transport across the isohaline S, $Q_\mathrm{dia,est}(S)$. The second equality in (36) results from the integration of the entrainment relation (26) over the projection of the isohaline part situated upstream of the transect T. The third relation of (36) which had not been proposed by Walin (1977) is simply the S-derivative of (34) restricted to the upstream part of the estuary. Walin (1977) stated about this relation (his Eq. 7): *Equation (36) represents in the most simple way how the deep water supply is related to the overall vertical (i.e. cross-isohaline) mixing properties in the basin.* What Walin (1977) specifically calls the *deep water supply* to the Central Baltic Sea is more generally

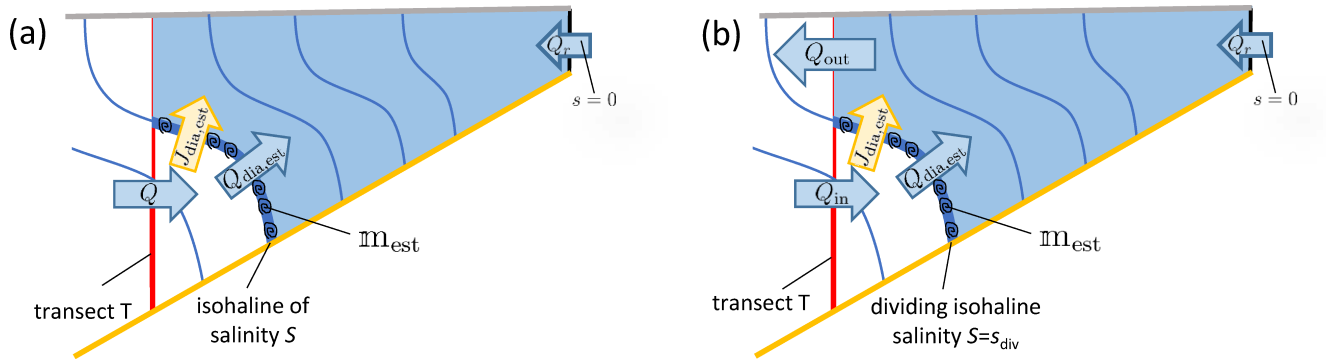

Figure 9. Sketch showing the relation between estuarine circulation and diahaline mixing. (a) Demonstration of the relation (36) by Walin (1977). (b) Demonstration of the relation (37) by Burchard et al. (2025) using the dividing salinity isohaline to quantify the exchange flow by means of $Q_{\rm in}$.

the up-estuarine part of the estuarine circulation. Note that independently of Walin (1977), Wang et al. (2017) used the first two equalities of (36) to calculate exchange flow accumulated between two estuarine segments.

When choosing the dividing salinity $S = s_{\rm div}$ for relation (36) with $Q(s_{\rm div}) = Q_{\rm in}$ (see Sec. 3.2), then the quantification of the estuarine circulation is directly linked to mixing:

$$Q_{\rm in} = -\frac{\partial J_{\rm dia,est}(s_{\rm div})}{\partial S} = -\frac{1}{2}\frac{\partial \mathbb{m}_{\rm est}(s_{\rm div})}{\partial S}, \tag{37}$$

see details in Burchard et al. (2025) and Fig. 9b. The significance of (37) is that it is a direct quantification of the estuarine circulation (defined as $Q_{\rm in}$) by means of the (S-gradient of the) diahaline mixing. This relation is directly applicable to simple estuaries with a typical two-layer exchange flow, but has also been extended to multi-layer exchange flow (Burchard et al., 2025). For the Elbe River estuary, relation (37) is demonstrated in Fig. 10.

3.7 Mixing of other constituents than salt

This review focuses on mixing of salt. The reason is that salinity is the defining constituent of estuaries, continuously ranging from minimum values near zero in the river water towards ocean salinity values near the mouth of the estuary or in the river plume. Therefore, salinity can be used as a coordinate in estuaries (Walin, 1977) substituting spatial coordinates. Also, salinity is conservative with basically no inner sinks and sources, and also bottom and surface fluxes of salt are negligible. However, many other constituents are mixing in estuaries, such as heat, oxygen, nutrients, and pollutants. Based on the work of Walin (1977, salinity coordinates) and Walin (1982, temperature coordinates), for larger ocean scales, theoretical Water Mass Transformation (WMT) frameworks have been developed to analyse mixing of constituents other than salt (Hieronymus et al., 2014; Groeskamp et al., 2019). To evaluate non-conservative behaviour of estuarine tracers due to sources or sinks, such tracers are often represented as function of salinity (Boyle et al., 1974). By doing so, non-conservative tracer mixing is identified by a non-linear relation between tracer concentration and salinity. However, as shown by Loder and Reichard (1981),

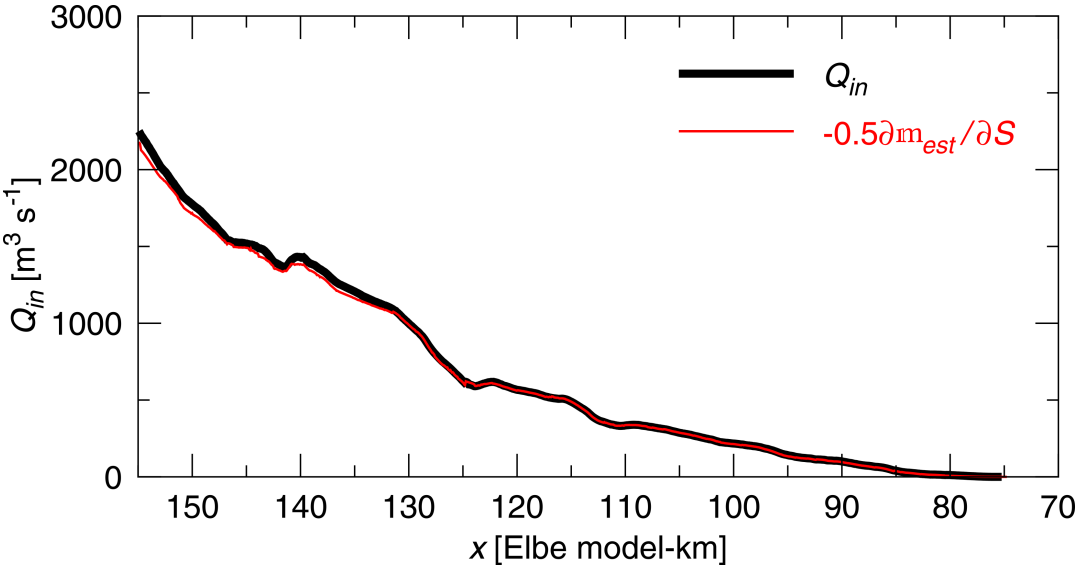

Figure 10. The relation (37) between estuarine circulation (quantified as the inflowing volume transport Q_{in}) and estuarine mixing (quantified as $\mathrm{m}_{\mathrm{est}}$), averaged over two spring-neap cycles during April 2024 in the lower Elbe River estuary in Germany.

such non-linear behaviour could also be caused by tracer variability in the freshwater source of the estuary. There is a large body of literature about effects of estuarine mixing of tracers other than salt on ecosystem dynamics. For example, Geyer (1993) proposes differential vertical mixing of suspended particulate matter (SPM) as a mechanism of creating Estuarine Turbidity Maxima. Tidal covariance between longitudinal velocity and concentration of SPM due to vertical SPM mixing can lead to up-estuary SPM transport (Scully and Friedrichs, 2007). In a similar way, Scully et al. (2022) explain the generation of local maxima of carbon dioxide partial pressure in estuaries, the so-called Estuarine Gas Exchange Maxima. Nitrogen-to-phosphate ratios in estuaries has been shown to critically depend on tidal mixing (Lui and Chen, 2011). These are just a few examples which show the essential role of mixing of tracers other than salt in estuaries. However, a general theory for such tracer mixing has not yet been proposed.

4 Major mixing processes and estuarine mixing hotspots

In the previous chapters we have presented various local and bulk theories of mixing and showed examples for the Elbe River estuary. These theories and examples prove that mixing, defined as integrated or local salinity variance decay due to turbulent processes, is an ubiquitous element in estuaries. Moreover, mixing defines what an estuary, consisting of a mixture of ocean and river water, is. While we know from the bulk mixing rules for estuaries, e.g., the *Knudsen mixing law* (21) or the *universal law of estuarine mixing* (33), how strong the overall mixing is in an estuary, we need to understand where the mixing occurs in time and space and which processes drive it. The intensity of mixing in an estuary is dictated by (10), $\chi_s \approx 2K_v(\partial s/\partial z)^2$,

indicating that mixing depends linearly on the intensity of turbulence, as expressed by the vertical diffusivity, and quadratically on the strength of the vertical salinity gradient. Typically in estuaries, the stronger the turbulence, the weaker the vertical salinity gradient, so it is not obvious a priori where and when mixing will be maximal in an estuary. In this section, the mixing in the Elbe estuary (and in one case that of the James River estuary) is used to provide an example of the various factors influencing the temporal and spatial variation of mixing in a partially mixed estuary.

4.1 Temporal variability

In estuaries, various time scales are relevant, including semi-diurnal tidal time scales and the fortnightly spring-neap cycle as well as times scales of weather and river-run-off (days to months). In the subsequent sections, the most relevant processes on these time scales are discussed.

4.1.1 Tidal variability

An analysis of the tidal cycle of the vertical salinity variance in the Elbe River estuary using (12) averaged over most of the estuary demonstrates the sequence of processes driving mixing (Fig. 11).

Panel (a) of Fig. 11 indicates that the vertical variance shows considerable variation through the tidal cycle, sharply rising at the end of flood, then decreasing to a minimum near the end of ebb. Panel (b) of Fig. 11 shows the individual terms in the vertical variance balance (12). Lateral straining is strongest during the flood tide (Fig. 11c). It accounts for most of the increase in stratification (as expressed by total vertical variance) toward the end of the flood tide, but it has little correspondence with mixing. This contribution of lateral straining has been observed in other estuaries (Purkiani et al., 2015; Geyer et al., 2017), with the important consequence that it produces a maximum in stratification at the beginning of the ebb tide. The longitudinal strain is actually negative during the flood (i.e., weakening stratification), but it is strongly positive during the ebb. This is the well-known signal of tidal straining, first described by Simpson et al. (1990). Particularly notable are the mid-ebb peaks in mixing, which are almost exactly in phase with the peak in longitudinal straining. This correspondence between longitudinal straining during the ebb and estuarine mixing has been found in other partially mixed estuaries including the Hudson River estuary (Wang and Geyer, 2018; Warner et al., 2020) and also the more strongly stratified Changjiang River estuary (Li et al., 2018) and Connecticut River estuary (Holleman et al., 2016).

Why is longitudinal straining so effective at increasing estuarine mixing? Going back to (10), we see that the intensity of mixing depends more sensitively on stratification than on the turbulence itself, although both are necessary to generate mixing. The positive strain that occurs during the ebb provides a continual source of stratification, which roughly balances the destruction of stratification by mixing during a significant fraction of the ebb tide (the times when the longitudinal strain and mixing have equal magnitude in Fig. 11). Paradoxically, the increased stratification during the ebb actually has an inhibitory influence on turbulence, but this inhibition of turbulence causes an enhancement of the vertical shear during the ebb. Fig. 12 shows representative vertical profiles of velocity u, salinity s, eddy diffusivity K_v and mixing χ_s during flood and ebb in the Elbe estuary. The strong mixing that occurs during the ebb is found in the stratified boundary layer, in which the eddy diffusivity is actually much weaker than its value during the flood tide. The key to the mixing is the persistence of stratification,

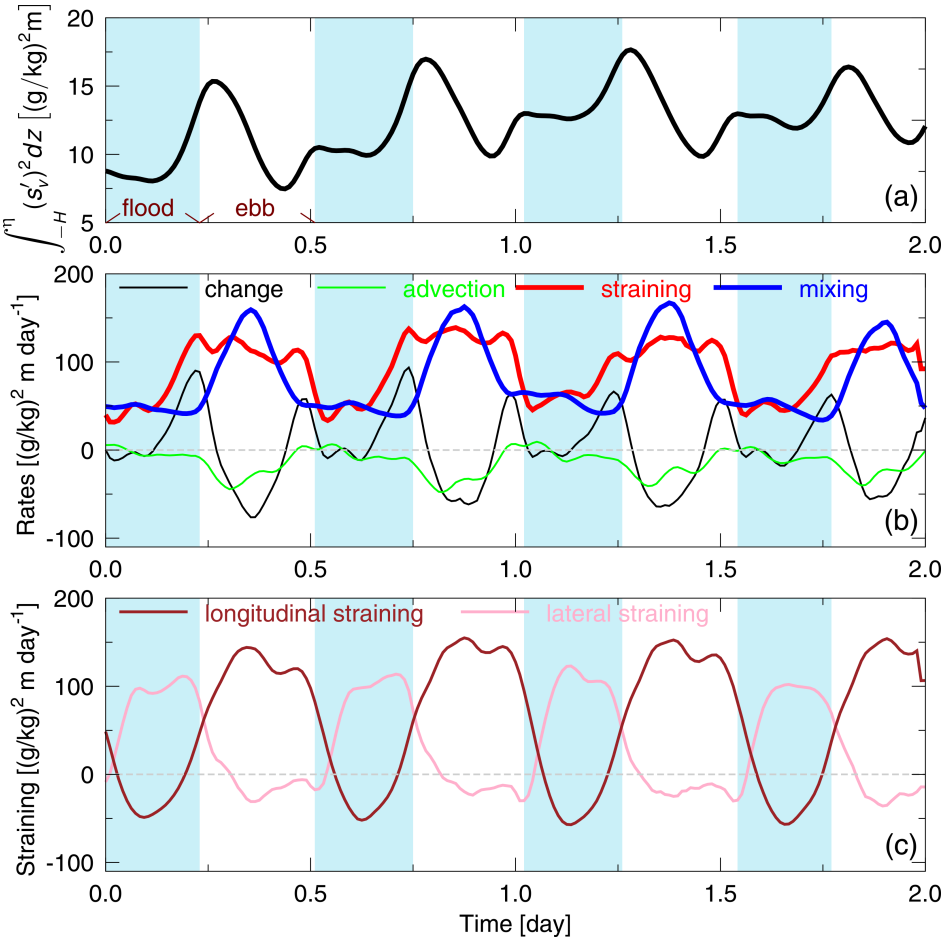

Figure 11. Dynamics of vertical salinity variance, spatially averaged over the Elbe River estuary domain between river kilometres 85 and 160, during four tidal cycles. a) Vertical salinity variance; b) Terms in the variance budget (12); c) Straining term split into longitudinal and lateral components.

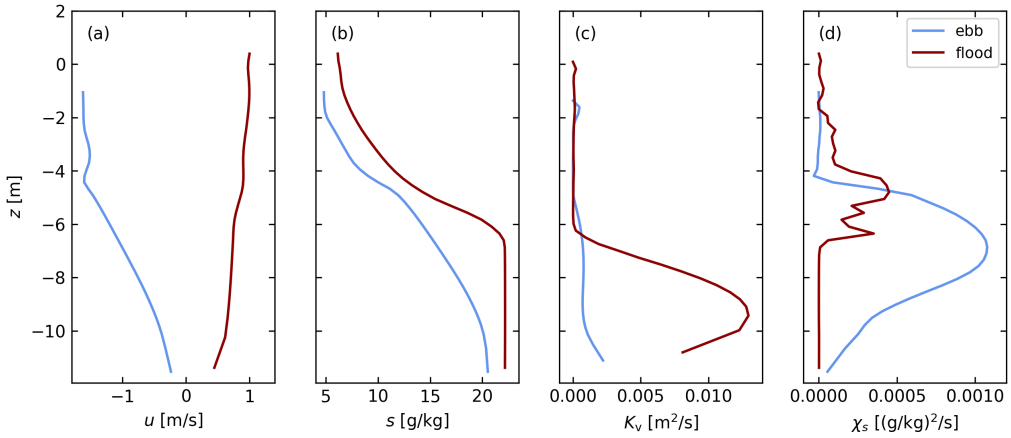

Figure 12. Simulated vertical profiles of (a) the along-channel current velocity u, (b) salinity s, (c) vertical eddy viscosity K_v, and (d) local salt mixing χ_s from a near-shoal location within the inner Elbe River estuary at along-channel position $x = 127$ km for ebb (blue) and flood (red), respectively, during a neap tidal cycle. The data was averaged over five neighbouring grid cells, corresponding to an along-channel distance of 360 m. Temporally, the data was averaged for one hour around peak ebb and peak flood, respectively.

which is maintained by the strong shear that strains the along-estuary density gradient. Even though turbulence is weakened by stratification, it is not completely suppressed, due to the turbulence production originating from the bottom stress. During the flood tide, the boundary layer produces virtually no mixing, due to the absence of stratification. The only significant mixing occurs in the pycnocline when the well-mixed highly turbulent bottom boundary layer is entraining into the stratified layer above, where the turbulence is much weaker than the boundary layer but the stratification is strong. This shows that maximum mixing does not occur at the maxima of eddy diffusivity or salinity stratification, but at locations where both overlap (see also Warner et al., 2020, who report similar results for the Hudson River estuary).

4.1.2 Spring-neap cycle

The spring-neap cycle of tidal amplitude variation results in a large variation in the intensity of mixing, as shown in a time-series based on the numerical model of the Elbe estuary. As often observed in partially mixed estuaries, the stratification (as represented by vertical variance, Fig. 13b) shows a large variation over the spring-neap cycle, with a sharp peak in stratification each neap tide. Again we have the paradoxical result that the peak mixing occurs during neap tides (Fig. 13c), when turbulent intensity is the weakest. Returning to (10), the mixing depends on the square of the vertical salinity gradient but only linearly on the eddy diffusivity. According to estuarine theory, stratification varies roughly as K_v^{-2} (MacCready and Geyer, 2010), so the increased stratification is a much more important contributor to mixing than K_v through the spring neap cycle.

The timeseries of longitudinal strain through the spring-neap cycle (Fig. 13c) shows that it has similar spring-neap variation as mixing. The strain is a key ingredient for mixing — without it the stratification would vanish and there would be nothing

to mix. The strain increases during neap tides due to the increased stratification, which augments the horizontal strain term in (12) directly by the increase in s_v', and indirectly by the stratification-induced reduction in eddy viscosity, which increases u_v' (MacCready and Geyer, 2010).

Other estuaries show a different phase relationship between mixing and the spring-neap cycle. For example, in the Hudson River estuary the peak mixing occurs between neaps and springs (Wang and Geyer, 2018), and in the Changjiang River estuary outflow the peak mixing occurs during spring tides (Li et al., 2018). These variations in the timing of mixing are related to the relative strength of tidal forcing to the stratifying tendency of the estuarine circulation. This balance is represented by the Simpson number as defined in (13). In the Elbe River estuary, Si remains low for most of the spring-neap cycle, with strong stratification only occurring around the time of neap tides. The Hudson River estuary has higher values of Si, and the Changjiang higher still, leading to persistent stratification through the spring-neap cycle (Li et al., 2018). A closer look into the dynamics of the Changjiang River estuary reveals that most of the mixing occurs outside the estuary in the extensive river plume, due to the high river discharge (Li et al., 2018; Chang et al., 2024). In the sense of the universal law of estuarine mixing (32), this can also be formulated as follows: Since the estuary is relatively fresh during high-flow conditions, mixing inside the estuary is small. Therefore strong mixing must occur outside the estuary, i.e. in the river plume, to amount to $\mathbb{M}(S) = S^2 Q_r$, where here S is a salinity separating the estuary - river plume continuum from the adjacent coastal ocean. In this high Si regime, the strength of the turbulence becomes the limiting factor controlling mixing, leading to the peak mixing during spring tides.

Although these studies did not investigate the processes of mixing in detail, neap tidal turbulence might not be sufficiently strong to entrain the turbulent bottom boundary layer into the region of the surface-attached buoyant plume and cause mixing. Therefore, substantial near-surface salinity stratification remains until spring tides reduce it by mixing. In general it could be hypothesised that in tidally energetic estuaries vertical salinity variance is mixed away immediately once it is generated by straining during neap tides, as in the Elbe, Hudson and Pearl River estuaries. In stratified estuaries, this mixing process is delayed until spring-tide turbulence can efficiently mix, as in the Changjiang River estuary.

4.1.3 Variation with variance input and direct meteorological forcing

In estuaries, there are four boundaries through which salinity variance can be introduced: the river boundary (river discharge), the seaward boundary (salinity fluctuations at the mouth), the sea surface (evaporation and precipitation) and the bottom (groundwater discharge, which we do not further consider here).

The bulk mixing laws for estuaries show clearly that under balanced conditions, mixing should be proportional to the river runoff Q_r. This is obvious from the *Knudsen mixing law* in an estuarine volume bounded by a fixed transect, $\mathbb{M} = s_{\mathrm{in}} s_{\mathrm{out}} Q_r$, (see (21) as proposed by MacCready et al., 2018) and for the *universal law of estuarine mixing* inside a volume bounded by an isohaline surface of salinity S, $\mathbb{M}(S) = S^2 Q_r$, (see (32) as proposed by Burchard, 2020). Since these two theories are based on long-term averaging, time lags between changes in runoff and changes in mixing are expected due to the storage of volume, salt and salinity variance (Broatch and MacCready, 2022). The dependence of mixing on runoff has most impressively been shown in the study by Broatch and MacCready (2022) for the Puget Sound: When the runoff during summer becomes four times larger than the spring runoff, mixing increases roughly by the same factor, showing a much stronger signal than the

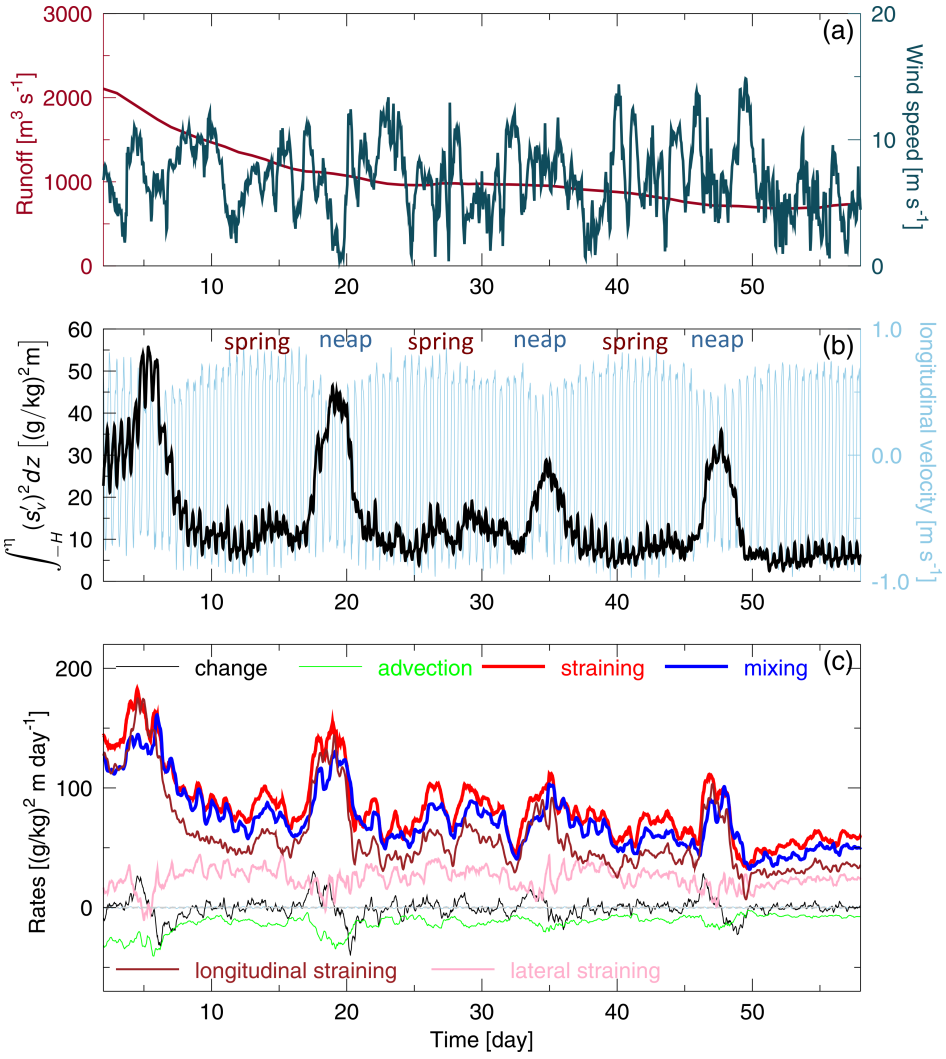

Figure 13. Dynamics of vertical salinity variance, spatially averaged over the Elbe River estuary domain between river kilometres 85 and 160, during four selected spring-neap cycles, as well as forcing conditions. (a) Runoff and wind speed; (b) vertical salinity variance and longitudinal tidal velocity amplitude; (c) terms of the vertical salinity budget according to (12).

spring-neap cycle. This is specifically supported by the universal law (32): Since the salinity at the mouth of the large Puget Sound might not change much, the volume-integrated mixing should be largely proportional to the river discharge. Similarly, the Elbe River estuary simulations show higher neap-tide mixing peaks during high runoff than during low runoff (Figs. 13a,c), which is consistent with the estuarine mixing laws (21) and (32).

In estuaries salinity fluctuations at the open ocean boundary are typically small and fluctuating with the tidal flow. In addition, salinity might vary with the dynamics of wind-driven upwelling and downwelling. An extreme example of the latter is the essentially non-tidal and highly industrialised Warnow River estuary in the Western Baltic Sea where downwelling events can decrease the offshore salinity from 20 g/kg to 8 g/kg within a few hours (Lange et al., 2020), leading to substantial salinity variance changes in the estuary and an inversion of estuarine circulation. This variance input has also strong impacts on the mixing in the estuary (Burchard et al., 2025).

Evaporation and precipitation should have an effect on estuarine mixing by affecting the variance input available for mixing, see the extended Knudsen mixing law (24). For classical freshwater-dominated tidal estuaries we are not aware of dedicated studies of this effect, although the good agreement between the simulated mixing (including precipitation and evaporation) and the estimate (32) (which neglects precipitation and evaporation) in studies of such estuaries by Li et al. (2022) and Reese et al. (2024) indicates that its impact may be negligible. For the Persian Gulf, a large inverse estuary with some freshwater inflow, Lorenz et al. (2021) applied (24) and estimated that evaporation caused about half of the variance input for mixing, with the other half generated by the freshwater runoff. This ratio between the two mixing contributions needs to be compared to the ratio of the freshwater transports due to evaporation ($-Q_{\mathrm{surf}}$) and river discharge (Q_r), which is 10:1 for the Persian Gulf. This implies that indeed, mixing of variance input from evaporation should generally have the tendency to be small compared to mixing caused by river discharge.

The effect of wind forcing on estuarine mixing has not yet been a focus of dedicated studies. Wind forcing can generally have two competing effects: straining of the salinity field and mixing (Scully et al., 2005; Chen and Sanford, 2009). Down-estuary wind forcing has a similar effect to ebb tidal straining by shearing less dense brackish water over dense ocean water and suppressing turbulence (Sec. 4.1.1 and Geyer, 1997). When a certain threshold is exceeded, the mixing effect of wind forcing would win over the straining effect, such that strong down-estuary winds are expected to be destratifying. In contrast to that, up-estuary winds have the same effect as flood straining and are therefore always destratifying. In a correlation analysis, Broatch and MacCready (2022) showed that wind forcing has some effect on mixing in Puget Sound, which however is dominated by the river runoff forcing. For a small weakly tidal estuary Yin et al. (2025) described the effect of wind pumping (covariance between wind stress and flow velocity) as an effective mechanism of up-estuarine salt transport which eventually will lead to increased salt mixing. However, in the tidally more energetic Elbe River estuary no obvious influence of the wind forcing is visible (compare Figs. 13a and c), although this has not yet been investigated by means of a correlation analysis.

4.2 Spatial variations

If estuaries had a flat bottom, their dynamics could be largely explained by means of one-dimensional or two-dimensional models without lateral variations. However, most estuaries are characterised by one or more deep channels (often deepened

due to dredging) in longitudinal direction which carry most of the tidal flow. Shoals at the sides and between the channels lead to a typical channel-shoal structure where the channel-shoal transition leads to dynamic processes crucial to estuarine circulation and mixing (Sec. 4.2.1). But also in longitudinal direction, estuaries are not smooth. Channels often show a strong along-channel variability, e.g., due to constrictions in width and depth leading to local fronts and enhanced mixing (Sec. 4.2.2).

4.2.1 Channel-shoal interaction

Since flood and ebb currents in the tidal channels are faster than over the shoals, a significant lateral velocity gradient evolves over the channel-shoal transition (Fig. 14a). During flood, this velocity shear in conjunction with the longitudinal salinity gradient leads to a faster increase of the salinity in the channel than on the shoal (differential advection, see Huzzey and Brubaker, 1988; Geyer et al., 2020), such that a lateral salinity and thus density and internal pressure gradient is generated (Fig. 14b). The pressure gradient drives a lateral exchange flow leading to the generation of vertical salinity stratification (Fig. 14c) which is then mixed due to bottom-generated turbulence over the channel-shoal transition (Fig. 14d). A similar situation occurs during ebb, when differential advection leads to lower salinities in the channel centre as compared to the shoals. This substantially increased mixing over the channel-shoal transition has been shown by means of numerical model simulations for the Hudson River estuary by Warner et al. (2020) and for the Elbe River estuary by Reese et al. (2024, 2026). The intensified mixing over the channel-shoal transition in the Elbe River estuary is also demonstrated in Fig. 7a. Observations in San Francisco Bay (Collignon and Stacey, 2013) and the James River estuary (Huguenard et al., 2015) show enhanced mixing over the channel-shoal transition as well.

It should be noted that the lateral shear over the channel-shoal transition during flood is one leg of a lateral circulation across estuaries that leads to strong axial flow convergence near the surface (Nunes and Simpson, 1985). It was later found that lateral straining is also an important mechanism feeding back into the longitudinal estuarine circulation and up-estuarine salt transport (Lerczak and Geyer, 2004; Burchard et al., 2011; Bo et al., 2024), which indirectly leads to increased salt mixing in estuaries.

4.2.2 Mixing at fronts

Bathymetrical bumps and lateral constrictions in a tidal channel in conjunction with tidal flow and longitudinal salinity gradients can lead to frontogenesis in estuaries (Geyer and Ralston, 2015) as well as increased mixing. The principle of this process is sketched in Fig. 15 for the example of an ebb current: Assuming an initially vertically well-mixed estuary with equally-spaced vertical isohaline surfaces, a sheared ebb current over a bathymetrical bump and a zone of weak recirculation downstream of the bump (Fig. 15a), the isohalines will be strained differentially. Over flat bathymetry, the classical ebb straining described by Simpson et al. (1990) will occur, leading to increased mixing (Sec. 4.1.1, and left side of Fig. 15b). On the lee side of the bump, where the ebb flow is partially blocked near the bed, the down-estuary advection of the isohalines is reduced or inverted while it is increased near the surface. This situation leads to a near-bottom retention of saline water on the lee side of the bump and thus to increased salt stratification. At the same time, the recirculation velocity near the bed and thus the vertical shear on the lee side of the bump will increase due to the backward slope of the strongly stratified isohalines. Increased shear, in turn, leads to increased turbulence production which in concert with strong stratification finally leads to strongly increased mixing.

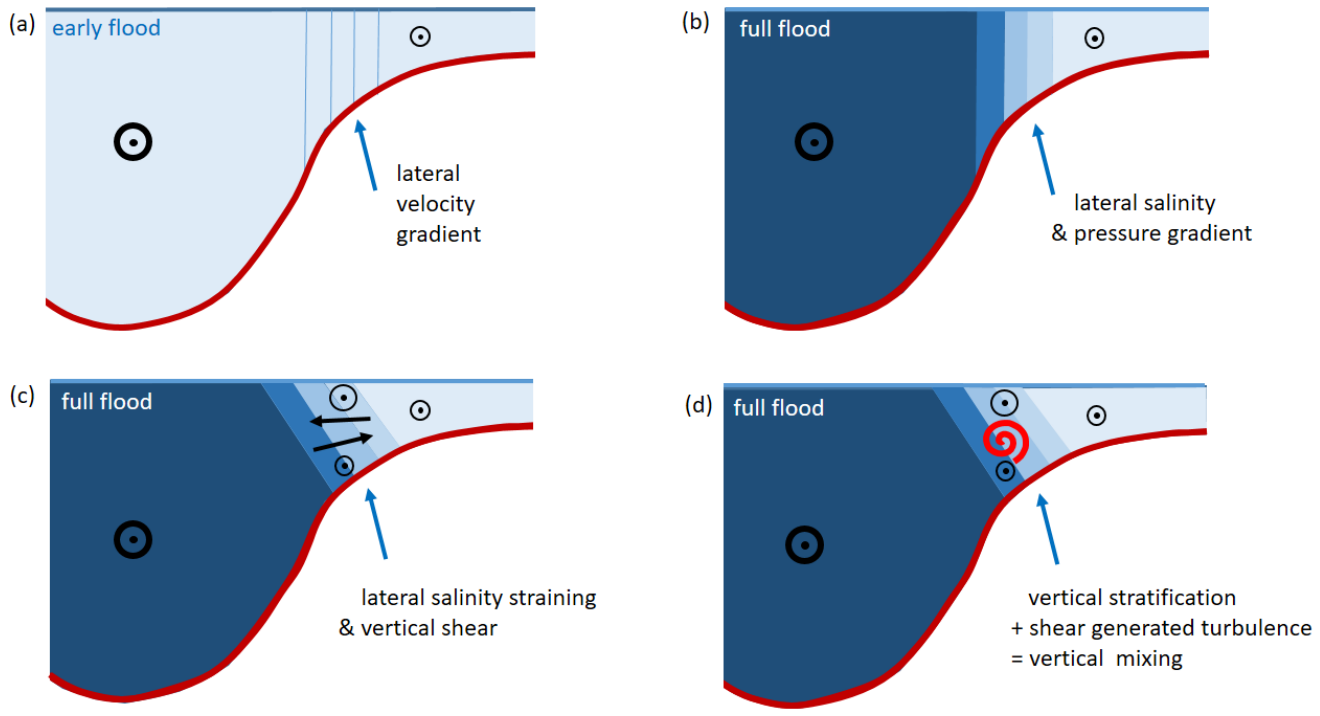

Figure 14. Sketch for explaining the effect of the channel-shoal transition on estuarine mixing during flood. The colour scaling indicates salinity, with dark blue colours representing high salinities. (a): early flood, when for simplicity no lateral salinity gradients are assumed; (b): full flood, generation of lateral salinity and thus density gradients due to differential advection; (c): full flood, lateral exchange flow driven by lateral density gradients leading to vertical stratification; (d): vertical shear generates small-scale turbulence which in concert with vertical stratification leads to vertical mixing.

In their model simulations of the Hudson River estuary, Geyer and Ralston (2015) show that the composite Froude number (Armi and Farmer, 1986) in the frontal zone becomes supercritical in a similar way as was observed offshore of the lift-off point of a river plume at the mouth of an estuary (Horner-Devine et al., 2015). Mixing hotspots related to bathymetric bumps in tidal channels are also visible in model simulations for the Hudson River estuary (Geyer and Ralston, 2015; Warner et al., 2020).

A realistic example of frontal mixing comes from a numerical model representation of the partially mixed James River estuary (Fig. 16). This estuary has two pronounced constrictions, one at km 18, and the other at the mouth at km 30. The expansions on the seaward (right) side of these constrictions result in steep upward tilt of the isopycnals due to the supercritical hydraulic response to the expansions (Geyer et al., 2017). These steeply sloping isopcnals are associated with strong horizontal and vertical salinity gradients, i.e., frontal conditions. At the time of maximum ebb, mixing (as quantified by $\chi_s \approx 2K_v\,(\partial s/\partial z)^2$) shows a pronounced maximum along each of the frontal zones. The energy for mixing along these frontal zones does not

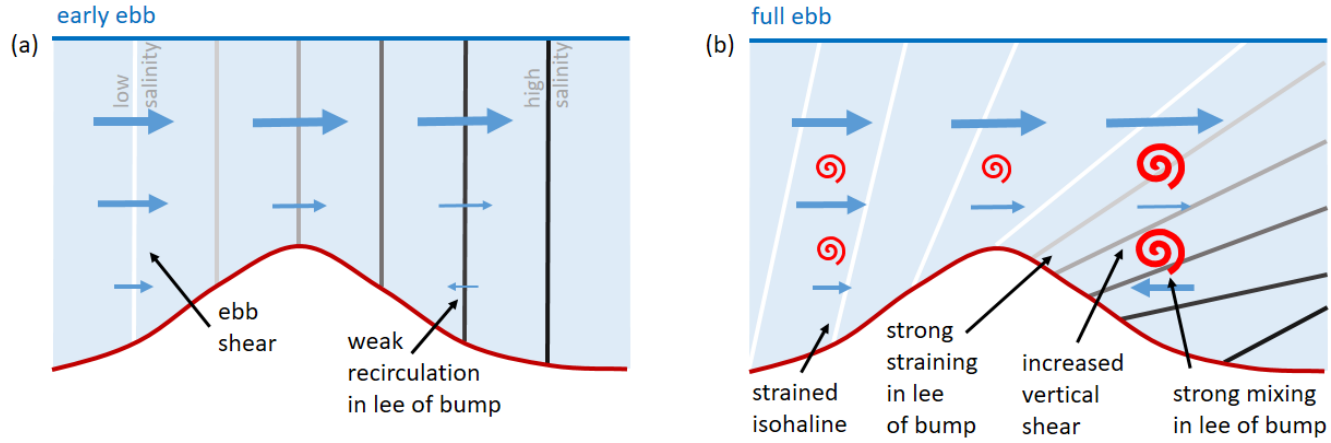

Figure 15. Sketch explaining the effect of along-channel bathymetric bumps on increased mixing during ebb. (a): The vertical lines represent isohalines, with light grey shading indicating lower and dark grey shading indicating greater salinity. During this phase of early ebb, the salinity field is still assumed to be vertically well-mixed. The arrows represent horizontal flow velocity, showing some weak recirculation in lee of the bathymetric bump; (b): due to strong shear and blocking of the flow, the salinity field is most strongly strained in lee of the bump. The combination of strong shear-generated turbulence and strong salinity stratification then leads to a hotspot of vertical salt mixing.

come from the bottom boundary layer, but rather from the baroclinic shear associated with the steeply sloping pycnocline. That strong shear also maintains the strong stratification via longitudinal straining of the horizontal salinity gradient. An observational example of the same phenomenon is discussed in Sec. 5.1 and illustrated in Fig. 17.

5 Methods to quantify mixing

5.1 Observational methods

Direct field measurements of the mixing of salt in estuaries is impractical, due to the microscopic scales at which the dissipation of salinity variance occurs, see Sec. 2.1. The turbulent motions that drive mixing can be resolved however, and numerous field investigations have quantified mixing based on measurements of turbulent motions at scales from metres to centimetres, then using theoretical arguments to relate the observable characteristics of the turbulence with either the mixing χ_s or the diahaline turbulent salt flux $j_{\mathrm{dia},z}$. A common approach is to use the relationship between the eddy diffusion coefficient for mass K_v and turbulent kinetic energy dissipation rate ε,

$$K_v = \frac{\mathrm{Rf}}{1-\mathrm{Rf}} \frac{N^2}{\varepsilon} \tag{38}$$

as proposed by Osborn (1980), where Rf is the flux Richardson number and N is the buoyancy frequency. With an estimate of K_v and a local measure of the vertical salinity gradient $\partial s/\partial z$, the vertical turbulent salt flux $j_{\mathrm{dia},z}$ and the salinity variance

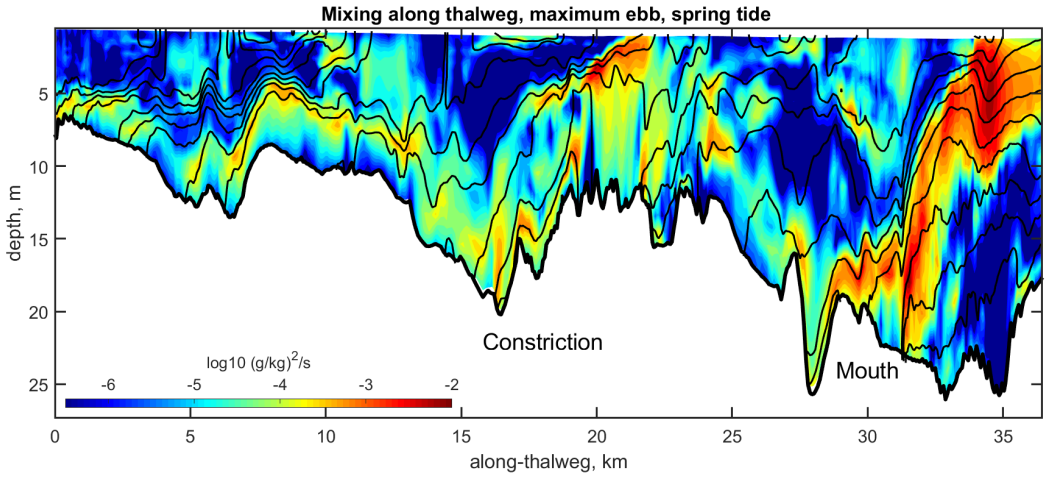

Figure 16. Realistic numerical simulation of conditions along the thalweg of the James River estuary during maximum ebb of spring tide, under moderate river discharge conditions, illustrating frontal zones with intensified mixing. The vertical component of the local mixing rate, $\chi_s \approx 2K_v \left(\partial s/\partial z\right)^2$, is shown as colour scale. The along-estuary salinity distribution is indicated by black contours (contour interval 1 g/kg).

dissipation χ_s are readily estimated, see (10) and (26). Peters and Bokhorst (2000, 2001) pioneered the use of a free-falling shear probe in an estuary for the purpose of quantifying mixing; since then this method has been followed in a variety of estuarine settings (Rippeth et al., 2001; Becherer et al., 2011; Ross et al., 2019; Huguenard et al., 2019; Reese et al., 2026). This method is challenging for measuring turbulence near the bottom, due to the risk of smashing the delicate shear probe into the bottom. An alternative method is the estimation of the dissipation rate ε based on the inertial-subrange velocity spectrum measured by a turbulence-resolving current meter (Trowbridge et al., 1999; Giddings et al., 2011). A related methodology pioneered by Gargett (1994), and applied by Stacey et al. (1999), Lu and Lueck (1999) and Giddings et al. (2011) among others is to use an Acoustic Doppler Current Profiler (ADCP) to obtain a direct measurement of the Reynolds stress $[\tilde{u}\tilde{w}]$, then in combination with a measure of the vertical shear to estimate eddy viscosity A_v, and then to infer the eddy diffusivity K_v and the mixing rate χ_s.

These methods are most effective in weak stratification conditions, when dissipation rates tend to be high and the turbulent length scale is readily resolved by the sensor. As stratification gets stronger, however, the scales of turbulent motions decrease, as scaled by the Ozmidov scale

$$L_O = \left(\frac{\varepsilon}{N^3}\right)^{1/2} \tag{39}$$

making it harder to obtain a reliable estimate of ε. More problematical is that the estimation of mixing χ_s depends on the square of the local salinity gradient, see (9), which itself is a challenging quantity to measure at the small vertical scales relevant to turbulence within a stratified environment.

Micro-conductivity sensors provide a means of resolving the salinity gradient and associated overturns at scales relevant to the characterization of turbulent motions (Peters and Bokhorst, 2001). The Thorpe overturn scale L_T (Thorpe, 1977) provides an alternative means of estimating the turbulent dissipation rate:

$$\varepsilon \approx L_T^2 N^3, \tag{40}$$

as shown by Peters (1997) in his turbulence measurements in the Hudson River estuary. It is particularly useful in the stratified interior, where the small vertical scales of turbulence make other methods of estimating ε more difficult (Etemad-Shahidi and Imberger, 2002; McPherson et al., 2019).

All of the above methods depend on a turbulence closure assumption as well as an estimate of mixing efficiency to link the dissipation rate ε to the actual mixing of salt, χ_s. The use of micro-conductivity sensors offers a more direct approach to estimating the mixing of salt. Following Holleman et al. (2016), high-frequency micro-conductivity time series measurements can resolve the inertial subrange and the viscous-convective subrange of the salinity variance spectrum

$$S_{ss}(k) = b_0 \chi_s \varepsilon^{-1/3} \mathcal{K}^{-1} \min(\mathcal{K}, \mathcal{K}_\eta)^{-2/3}, \tag{41}$$

where S_{ss} is the power spectral density of salinity variance, $b_0 = 0.4$ is the Kolmogorov constant for scalar variance, $\mathcal{K}$ is the wave number and $\mathcal{K}_\eta = 0.04(\varepsilon/\nu^3)^{1/4}$ is the Kolmogorov wave number, with the molecular viscosity ν. Note that the last term in (41) resolves the transition from the inertial subrange to the viscous-convective subrange at length-scales of $\mathcal{K}_\eta^{-1}$. As long as the height of the spectrum within either the inertial or viscous-convective subrange can be estimated, (41) can be used in combination with an estimate of ε to estimate mixing, i.e., the dissipation of salinity variance χ_s, without relying on turbulence closure assumptions. Moreover, the formula depends only weakly on the estimate of ε, which is often hard to estimate accurately in the stratified turbulent regime. Holleman et al. (2016) used this method to estimate mixing rates in the highly stratified Connecticut River estuary. Their analysis demonstrated peak values of χ_s in the pycnocline in association with intense shear instability during ebb tide (Fig. 17).

Acoustic backscatter also provides a more direct means of estimating mixing, as demonstrated by Lavery et al. (2013). Using a broadband array of echo sounders, Lavery et al. (2013) demonstrated that the observed scattering in the pycnocline of the Connecticut River estuary has a spectral slope consistent with the viscous-convective subrange. Other scatterers, such as fish, bubbles and sediment, have distinctly different spectral slopes. If the stratification is strong enough and other scatterers do not overwhelm the signal, the acoustic backscatter intensity can be used as a nearly direct measure of χ_s. While the signal-to-noise ratio of the acoustic amplitude does not offer the same precision as microstructure measurements, it produces remarkable spatial resolution, as demonstrated by acoustic measurements within a train of Kelvin-Helmholz instabililities in the Connecticut River estuary (Fig. 18). Based on the evidence provided by the analysis of Lavery et al. (2013), echo-sounding imagery can be used to identify regions of intense mixing, even if the actual magnitude of χ_s cannot be quantified.

5.2 Numerical modelling techniques

Since direct observations of turbulent properties in estuaries are very tedious and noisy (see the discussion in Sec. 2.1), the analysis of mixing in estuaries largely relies on numerical models. The advantage of numerical models is certainly their coverage

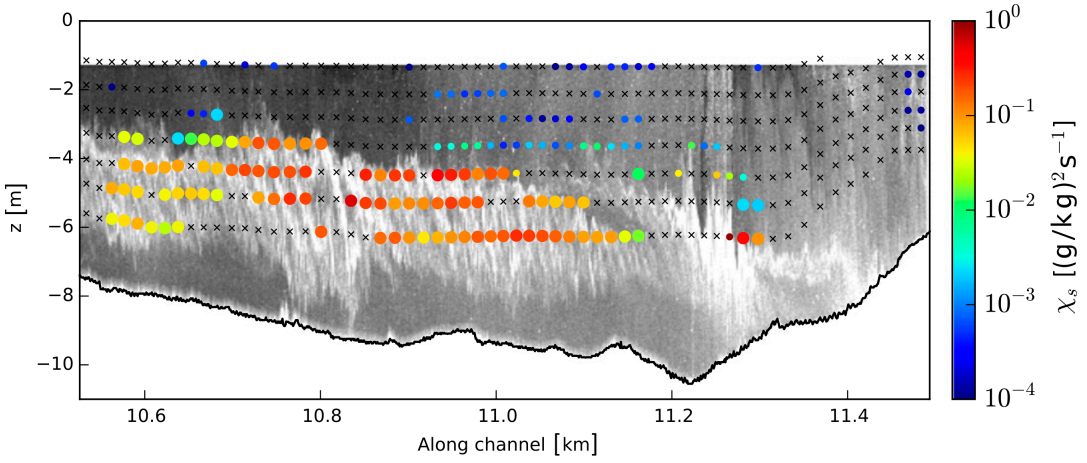

Figure 17. Spatial distribution of χ_s (coloured dots) in the stratified shear layer of the early ebb in the Connecticut River estuary, estimated from combined observations by a string of Acoustic Doppler Velocimetres (ADPs) and microconductivity probes. The crosses are locations where values of χ_s could not be reliably estimated. The grey scales in the background indicate the intensity of acoustic backscatter. This figure has been taken from Holleman et al. (2016).

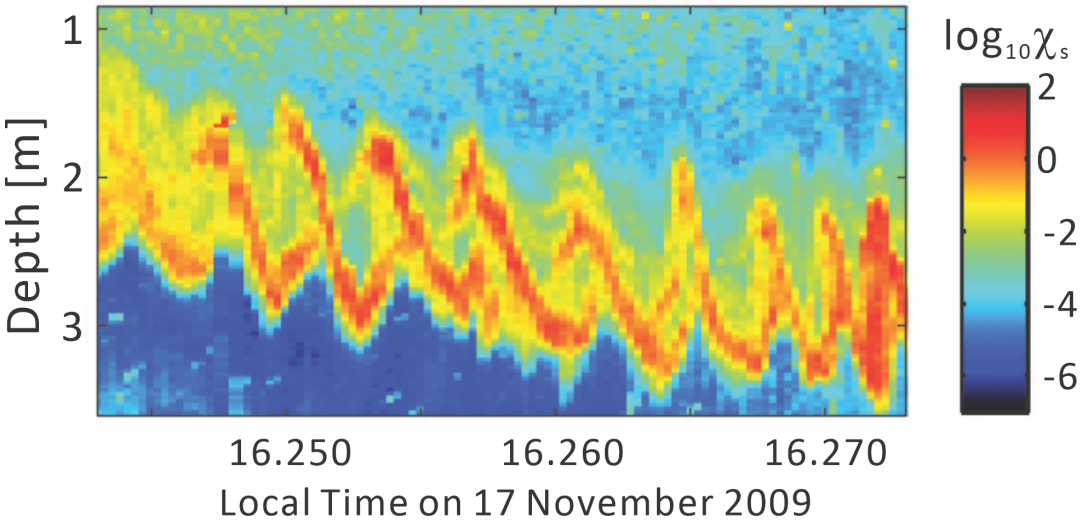

Figure 18. Kelvin-Helmholtz instabilities in the Connecticut River estuary. The colour shading shows the decadal logarithm of the salinity mixing χ_s, estimated from acoustic backscatter measurements. This figure has been taken from Lavery et al. (2013).

of the entire four-dimensional estuarine space (three spatial directions and time), whereas observations can only sparsely cover this space. However, to ensure that the numerical model results sufficiently represent real estuaries, several measures need to be taken: besides realistic input data into the model (such as bathymetry, open boundary conditions, meteorological forcing) and a thorough validation using observational data, the numerical model itself must be physically sound and numerically accurate. There is an extensive body of literature addressing these two topics (Griffies, 2004; Umlauf and Burchard, 2005; Shchepetkin and McWilliams, 2005; Zhang et al., 2016; Klingbeil et al., 2018). Here, we will present in more detail two aspects which are key to the proper assessment of mixing in estuaries: turbulence closure modelling (Sec. 5.2.1) and numerical mixing analysis (Sec. 5.2.2).

5.2.1 Turbulence closure modelling

The starting point of turbulence closures are the fundamental laws of momentum, mass and energy conservation from which transport equations based on molecular viscosities and diffusivities can be derived, see e.g. the molecular salinity equation (2). Applying the Reynolds decomposition (see Lesieur, 2008, and the discussion in Sec. 2.1) leads to transport equations for Reynolds-averaged variables, see e.g. the salinity equation (4), which include unknown second moments such as the vertical turbulent salt flux $j_{\mathrm{dia},z} = [\tilde{w}\tilde{s}]$. In a similar manner, exact transport equations can be derived for those second moments, which however would include unknown third moments, and so forth. This infinite series of unclosed higher and higher order equations establishes the turbulence closure problem. An example for a second-moment transport equation ($[\tilde{s}^2]$ in this case) is (5) which includes among others the vertical turbulent transport of the micro-structure salinity variance $[\tilde{w}\tilde{s}^2]$ as a third moment. Second-moment closures use parameterisations for all unknown third moments, such that the system of second-moment transport equations is closed. To substantially simplify the solution, equilibrium assumptions are made for most second moments in such a way that the sum of the transport divergence and the time change are set to zero. For the example of the micro-structure variance equation (5), this leads to the equality of stirring and mixing ($P_s = \chi_s$), see also the discussion in Sec. 2.1.

A central element of turbulence closures is the eddy diffusivity assumption (7), relating turbulent tracer fluxes to Reynolds-averaged tracer gradients, with the eddy diffusivity as a factor of proportionality, leading to the principle of down-gradient turbulent tracer fluxes. Similar assumptions are made for momentum and turbulent quantities. The eddy diffusivities include the entire second-moment closure. For the key quantity of the turbulent kinetic energy ($k = \frac{1}{2}[\tilde{u}_j^2]$), a budget equation is generally solved with shear production as source term and dissipation of TKE into heat as sink term. For stable stratification, turbulence leads to mixing as well as negative buoyancy production, which leads to an increase of local potential energy and acts as a further TKE sink term. For estuarine numerical modelling, the use of so-called two-equation turbulence closure models has become a good compromise between efficiency and accuracy (Warner et al., 2005a). In such models, the first equation generally is the budget-equation for the TKE, while the second equation is related to the length scale of turbulence, such as the dissipation rate of TKE, ε (the k-ε model), or the turbulence frequency, $\omega = \varepsilon/k$ (the k-ω model). If properly calibrated, these different versions of length-scale related equations perform similarly (Warner et al., 2005b). The most important aspect of the calibration is to ensure the quantitatively correct damping of vertical turbulent mixing caused by stable stratification. The principles of this calibration process are explained in the appendix (Sec. E). In essence, the steady-state gradient Richardson number is set to

the value of $\mathrm{Ri_{st}} = 0.25$ such that for stronger stratification ($\mathrm{Ri} > \mathrm{Ri_{st}}$), turbulence is suppressed and for weaker stratification it is enhanced. A properly calibrated turbulence closure model does also reproduce the canonical values of mixing efficiency $\Gamma \approx 0.2$ and the steady-state flux Richardson number $\mathrm{Rf_{st}} \approx 0.15$ (Osborn, 1980). It should be noted that these values would only be reached in numerical models for so-called stationary homogeneous shear layers where production and destruction of TKE are balanced. In cases of strong temporal variability or locations with a substantial vertical turbulent transport of TKE (such as in active entrainment layers), significant deviations can occur (see the discussion by Holleman et al., 2016).

5.2.2 Numerical mixing analysis

Although the numerical mixing in the model of the Elbe River estuary is relatively small (see Figs. 4 and 8), it can be of considerable size in other estuarine models (Ralston et al., 2017; Henell et al., 2023). Therefore, the quantification of numerical mixing is discussed here. As demonstrated in the previous sections, the comparison of analytically derived mixing relations with diagnosed mixing from numerical simulations requires the quantification of the total variance decay experienced by a tracer in the numerical model. This does not only consist of contributions from the parameterised turbulence closure (physical mixing), but also from the discretisation of the tracer advection operator (spurious numerical mixing; Griffies et al., 2000). It is assumed that the tracer advection discretisation is conservative, monotone (in the sense that it does not generate wiggles and new tracer maxima and minima) and weakly diffusive. Many advection schemes with these properties have been developed such as the FCT (Flux-Corrected Transport) schemes (Zalesak, 1979), TVD (Total Variation Diminishing) schemes (Pietrzak, 1998) and the MPDATA (Multidimensional Positive Definite Advection Transport Algorithm) schemes (Smolarkiewicz, 2006). They all use some degree of implicit diffusion to ensure monotonicity.

In many model applications, numerical mixing has been found to explain a large portion of the total (physical plus numerical) mixing. High values of numerical mixing of typically 50% have been found for the Baltic Sea (Hofmeister et al., 2011) and the Puget Sound (Broatch and MacCready, 2022), while Li et al. (2018) report about 33% of numerical mixing for their simulation of the Changjiang River estuary. Low numerical mixing has been seen for simulations with high explicit horizontal diffusivity (Reese et al., 2024, for the Elbe River estuary) or for idealised estuarine models (MacCready et al., 2018). To account for the role of numerical mixing and to evaluate measures for its reduction, numerical mixing analysis methods have been developed (Burchard and Rennau, 2008; Klingbeil et al., 2014; Schlichting et al., 2023; Banerjee et al., 2024). Here, we first briefly describe general methods to quantify physical and numerical mixing in ocean models, before we give recommendations on how to reduce numerical mixing (see below).

Methods to quantify numerical mixing.

To demonstrate methods to discriminate between physical and numerical mixing and to accurately quantify their sum, we give a detailed one-dimensional example of an advection-diffusion equation in App. F, including its discretisation (App. F1), the derivation of the mixing analysis (App. F2), a stationary solution of the one-dimensional advection-diffusion equation (App. F3) and the derivation of its analytical solution (App. F4). For this analysis, a first-order upstream (FOU) method is used as an example because it allows for an explicit discretisation of the physical and numerical mixing. Since the FOU scheme for advection shown in (F3) is inherently diffusive, it is generally not used in ocean models. Instead, mostly non-

linear schemes are used for which the spurious numerical variance decay cannot be analytically derived. To separate between physical and numerical mixing, it is convenient to carry out the advection and diffusion discretisation in different steps, as an operational-split method. After the advection step, the numerical mixing is diagnosed, and after the diffusion step, the physical mixing is calculated. It is also possible to further separate the numerical and physical mixing into horizontal and vertical contributions. Different methods of numerical mixing quantification have been proposed for the pure advection step. Since the advection equation for the squared tracer, (F2) for $K_h = 0$, is equivalent to the advection equation for the tracer itself, (F1) for $K_h = 0$, Burchard and Rennau (2008) proposed to additionally carry out an advection step for the squared tracer (which should conserve the squared tracer) and to subtract from it the square of the advected tracer, (F1), which reduces the squared tracer. This difference should be a good estimate for the variance reduction in a particular grid point during a particular time step. Division by the time step Δt should give the local numerical variance decay (or mixing). As an alternative, Klingbeil et al. (2014) proposed to calculate the left-hand side (time derivative and advection term) of the diagnostic tracer-square advection equation as an estimate for the right-hand side (which should be the numerical mixing). Yet another method has recently been proposed by Banerjee et al. (2024). All three methods are equivalent when integrated over a larger area, and differences do only show up in the local distribution of the numerical mixing. An accurate numerical mixing quantification requires the direct implementation of the analysis into the numerical model code, since analysing numerical mixing from model output even at high output frequency has proven quite inaccurate (Schlichting et al., 2023).

There are alternative diagnostic methods to quantify numerical mixing, however not in terms of variance decay (Gibson et al., 2017; Holmes et al., 2021; Drake et al., 2025).

Measures to reduce numerical mixing. Generally, a finer resolution should lead to a reduction of numerical mixing. However, Burchard and Rennau (2008) showed that this might not be very efficient, since for an idealised example a grid-refinement by a factor of nine in the horizontal direction and by a factor of four in vertical direction (equivalent to a 144-fold increase in computational resources) led to a reduction of numerical mixing by less than a factor of two. More promising is the better alignment of grid layers with isopycnals, or adding a Lagrangean type of vertical grid motion, to reduce vertical advection with respect to moving coordinate layers. Specifically, vertically adaptive coordinates proved to significantly reduce numerical mixing (Hofmeister et al., 2011; Gräwe et al., 2015). A further reduction of numerical mixing can be achieved by aligning the horizontal grid with the major tidal flow directions. The present Elbe River estuary model (adopted from Reese et al., 2026) as well as the Weser River estuary model by Rummel et al. (2025) align the curvilinear grid with the dredged navigational channel and not, as typically done, with the lateral shoreline. This reduces numerical mixing because in estuaries lateral salinity gradients are generally much larger than longitudinal ones, such that these specially constructed horizontal coordinates align with those gradients which then do not have to be advected with the along-estuary flow across grid interfaces.

Numerical mixing is a fact in all numerical model applications that cannot be avoided. It is therefore essential to quantify its contribution to the tracer distribution, which is the result of the sum of intended physical and unintended numerical mixing. Intentionally reducing physical mixing would be one way to obtain realistic total mixing. This has been impressively demonstrated by Ralston et al. (2017) who in a model application to the Connecticut River estuary reduced the physical mixing by reducing the steady-state Richardson number $\mathrm{Ri}_{\mathrm{st}}$ from the canonical value of 0.25 (see Sec. 5.2.1) to a very low value of

0.1. By doing so, they increased the numerical mixing from 50% to 66%, but lowered the total mixing such that the resulting salinity structure was more realistic. Such measures should however be handled with care since the numerical mixing generally has a different spatial and temporal distribution than the physical mixing (Klingbeil et al., 2014; Henell et al., 2023).

6 Future Perspectives

As reviewed in this paper, the work of past decades nowadays provides a consistent theoretical framework for estuarine mixing, the foundations of which have been laid in the early work by Knudsen (1900) and Walin (1977). Although their work did not explicitly define and quantify mixing, mixing theories are conveniently founded on their frameworks. In agreement with turbulence theory (Osborn and Cox, 1972; Mellor and Yamada, 1974), local mixing of a certain tracer is defined as the dissipation rate of the local variance of this tracer, χ_s, see eqs. (9) and (B1) and Burchard and Rennau (2008). Estuarine mixing $\mathbb{M}$ itself is then the integral of χ_s over estuarine volumes averaged over a certain period of time (e.g., the spring-neap cycle). Relating these definitions to bulk forcing parameters for the estuaries leads to the *Knudsen mixing law* (21) when the estuary is bounded by a fixed transect (MacCready et al., 2018) or to the *universal law of estuarine mixing* (32) when the estuary is bounded by a moving isohaline (Burchard, 2020). Therefore, to understand the estuarine mixing $\mathbb{M}$, its temporal and spatial composition by means of the local variance decay χ_s has to be studied. In a few cases, this was achieved through observations (e.g., Lavery et al., 2013; Holleman et al., 2016), but is more typically done with realistic numerical models of estuaries (e.g., Warner et al., 2020; Reese et al., 2024). These models are consistent with the mixing theories only if numerical mixing due to the discretisation of the tracer advection terms is included (e.g., Li et al., 2022). Using these observations and modelling techniques, the major mixing processes in some example estuaries are now understood, see e.g. Warner et al. (2020) for the Hudson River estuary, Broatch and MacCready (2022) for the Salish Sea, Henell et al. (2023) for the Baltic Sea and Reese et al. (2026) for the Elbe River estuary.

Due to its high relevance for the understanding of estuarine dynamics and its socio-economical and ecological consequences, the research on estuarine mixing will continue. More studies for other estuaries will certainly come, most probably resulting in a different weighting of the most relevant mixing processes, maybe even describing new processes. But apart from that, the future of estuarine mixing research will likely be dominated by the technological progress that allows for ever finer-resolved, more efficient numerical modelling down to smaller and smaller scales. Here, we discuss in detail where, and to which extent, we see potential for such progress.

Increased computational resources. It is expected that the trend of ever-increasing computational resources will continue. As an important development, the ongoing replacement of the more traditional Central Processing Units (CPUs) by modern Graphics Processing Units (GPUs) will improve the overall computational efficiency. As computational codes for coastal ocean models will become available for GPUs, this increase in computational power can be used for finer resolution models, longer simulation periods or larger model domains. Finer resolution models would be able to resolve further processes of estuarine mixing with more accuracy, such as smaller-scale topographic effects. Specifically, consequences of coastal engineering such as dredging and dam-building, which are commonly under-resolved in contemporary numerical simulations, could be reproduced

more realistically. Today, multi-decadal simulations of well-resolved estuaries are hardly feasible. Such longer simulation periods could, however, be used to better reproduce interannual variability and consequences of long-term trends such as sea-level rise and changes in precipitation and evaporation patterns. Larger model domains could help to include more of the tidal or non-tidal parts of rivers or larger portions of the adjacent ocean including the river plume. It has been shown that the universal law of estuarine mixing (33) is only valid for isohaline surfaces that do not leave the model domain. On the other hand, isohaline theory does not distinguish between estuarine and river plume mixing, and often the transition between the two cannot be seen from model topography and coastlines. Therefore, it is desirable to simulate the entire river-estuary-plume region within a single model setup. Similarly, the confluence of multiple estuaries and river plumes could be simulated at fine resolution when computational resources further improve.

Large Eddy Simulation modelling. More powerful computer resources could also allow for models with improved model physics, such as using higher-order turbulence parameterisations or the application of Large-Eddy Simulation (LES) models. Both improvements would have a direct effect on the computation of mixing. One example for higher-order turbulence closure models could be the use of non-local models that do not enforce the down-gradient assumption of turbulent fluxes (see the recent study by Legay et al., 2025). Furthermore, parameterisations of Langmuir Turbulence which potentially affects estuarine mixing in the presence of wind waves could be added (Harcourt, 2015). The application of LES models to estuaries would mean that the most energetic turbulent eddies could be resolved instead of being parameterised by turbulence closure models. Then, only the small-scale mixing would need to be parameterised, for which generally relatively simple closures should be sufficient. A further advantage of LES models over classical coastal ocean models is their non-hydrostatic pressure calculation which would allow for the reproduction of non-hydrostatic effects such as internal lee wave generation (Skyllingstad and Wijesekera, 2004), generation of interfacial waves at pycnoclines when the surface and the bottom boundary layers interact (Yan et al., 2022) or Langmuir Circulation effects in shallow coastal waters (Wang et al., 2022). Two specific LES model applications have been reported by Li et al. (2008) and Li et al. (2010) who calculated a tidal water-column setup with periodic boundary conditions in both horizontal directions. So far, no further estuarine LES applications have been published. Specifically efficient LES model codes such as Oceananigans (Ramadhan et al., 2020) that can be executed on GPUs open vast possibilities of coastal (see the recent study by Huang et al., 2025) and estuarine LES applications in the future, starting with idealised setups, but also with the future potential to simulate estuarine dynamics over more realistic topographies.

Water Mass Transformation theory. The concept of Water Mass Transformation (WMT) has been strongly extended in recent years (see, e.g., Hieronymus et al., 2014; Groeskamp et al., 2019). Such multi-dimensional WMT concepts using other constituents in addition to salinity, such as temperature or biogeochemical tracer concentrations, are typically applied to large-scale ocean problems. Estuarine applications have yet to be created, but could give insight where, for example, temperature plays an important role in addition to salinity, such as shown for the Arctic Ocean (Pemberton et al., 2015), the Persian Gulf (Lorenz et al., 2020) or the Baltic Sea (Henell et al., 2023).

Machine Learning. Finally, applications of Machine Learning (ML) have entered all fields of oceanography, including coastal and estuarine research. Typical estuarine applications would comprise the calculation of river discharge from meteorological data (Börgel et al., 2025) or the estimation of the salt intrusion length inside estuaries (Rummel et al., 2025). It is not

yet obvious in which way fast, efficient and well-trained ML algorithms could be exploited to support research on estuarine mixing, but it can certainly be expected that ML applications will soon extend our toolkit in addition to numerical modelling and observational methods.

Appendix A: Stirring and mixing: the case of saltwater in a glass beaker

The effects of stirring and mixing in a fluid subject to molecular diffusion are explained here quantitatively by means of a simple analytical example. We assume a fluid in a glass beaker of 0.1 m depth and a cross-sectional area of 0.01 m^2, thus containing 1 litre of fluid. Imagine our beaker initially contains salty water underlaying freshwater with a smooth transition in between, with a horizontally homogeneous distribution such that they only depend on the vertical coordinate z and time t. The vertical diffusive spreading of the salinity $\check{s}$ in our beaker would then be described by the classical one-dimensional diffusion equation of the form

$$\frac{\partial \check{s}}{\partial t} = \kappa \frac{\partial^2 \check{s}}{\partial z^2} \tag{A1}$$

with $\kappa = 10^{-9} \mathrm{m}^2\ \mathrm{s}^{-1}$ denoting the molecular diffusivity of salt. Let us assume an initial salinity distribution of the form

$$\check{s}(z) = \frac{1}{2} s_{\max} \left(1 + \cos\left(\frac{n\pi z}{D}\right)\right), \tag{A2}$$

with the maximum salinity $s_{\max} = 30$ g/kg where n is a positive integer, and D the thickness of the fluid inside the beaker. For $n = 1$, the fluid is unstirred, and we only have a single layer of salty water underneath the freshwater with mixed conditions in between (see Fig. 1a). Increasing n may be viewed as a simple model for a stirring process that creates an increasing number of interfaces between salty and fresh water. For $n = 30$ (Fig. 1b), the stirring process has created 30 such interfaces, and for $n = 90$ (Fig. 1c), 90 interfaces can be defined. It should be clear that in a real beaker, the stirring process induces salinity patches and streaks that are highly distorted and three-dimensional. Nevertheless, our simple one-dimensional model is sufficient to illustrate the basic effects of stirring and mixing as shown in the following.

To investigate the temporal evolution of the salinity layers as a result of mixing, we insert an ansatz of the form

$$\check{s}(z,t) = \frac{1}{2} s_{\max} \left(1 + a(t) \cos\left(\frac{n\pi z}{D}\right)\right) \tag{A3}$$

into (A1), where $a(t)$ denotes the dimensionless amplitude of the salinity with $a(0) = \frac{1}{2}$. This yields a differential equation of the form

$$\frac{\mathrm{d}a(t)}{\mathrm{d}t} = -\frac{a(t)}{\tau}, \tag{A4}$$

where $\tau = D^2/(\kappa n^2 \pi^2)$ combines all parameters of the problem. The solution of (A4) is of the form

$$a(t) = e^{-\frac{t}{\tau}}\ , \tag{A5}$$

which reveals that τ plays the role of a *mixing time scale*.

The blue lines shown in Fig. 1 (see the figure caption for the parameters chosen) illustrate the behaviour of the solution found above for different values of n. For $n = 1$ (no stirring, Fig. 1a) the effect of mixing is seen to be negligible after a period of ten minutes. If some gentle stirring is applied (figuratively using the spoon) such that n is increased to 30, considerable mixing effects can be seen already after 10 minutes (Fig. 1b). Only intensive stirring ($n = 90$) leads to the desired result of (almost) complete mixing within a reasonable amount of time (Fig. 1c). For the parameters chosen, the mixing time scale is about $\tau = 17000$ minutes for the case of no stirring ($n = 1$), about $\tau = 19$ minutes for little stirring ($n = 30$), and about $\tau = 2$ minutes for strong stirring ($n = 90$).

Appendix B: Salinity-variance equations

This appendix introduces some Reynolds-averaged salinity-variance or salinity-square equations to demonstrate the function of the salinity variance decay χ_s as sink term. Based on (8) and using (9), the salinity variance equation with the local variance per unit volume $s'^2_{\mathrm{tot}} = (s - \bar{s}_{\mathrm{tot}})^2$ and the volume-averaged salinity $\bar{s}_{\mathrm{tot}}$ is of the following form:

$$\underbrace{\frac{\partial s'^2_{\mathrm{tot}}}{\partial t} + s'_{\mathrm{tot}} \frac{\mathrm{d}}{\mathrm{d}t}\bar{s}_{\mathrm{tot}}}_{\text{change}} + \underbrace{\frac{\partial (u s'^2_{\mathrm{tot}})}{\partial x} + \frac{\partial (v s'^2_{\mathrm{tot}})}{\partial y} + \frac{\partial (w s'^2_{\mathrm{tot}})}{\partial z}}_{\text{advection}} \underbrace{- \frac{\partial}{\partial x}\left(K_h \frac{\partial s'^2_{\mathrm{tot}}}{\partial x}\right) - \frac{\partial}{\partial y}\left(K_h \frac{\partial s'^2_{\mathrm{tot}}}{\partial y}\right) - \frac{\partial}{\partial z}\left(K_v \frac{\partial s'^2_{\mathrm{tot}}}{\partial z}\right)}_{\text{diffusion}} = - \underbrace{\chi_s}_{\text{mixing}} , \tag{B1}$$

where the advective and diffusive flux divergences conservatively re-distribute local variance. Mixing χ_s is the sink term for the local variance. An extra term due to the non-constant volume-averaged salinity $\bar{s}_{\mathrm{tot}}$ is included in the change term (MacCready et al., 2018, see Burchard et al. (2018b) for hints to the derivation). The variance budget of the entire estuary results from integration of (B1) over the volume of the estuary:

$$\underbrace{\frac{\mathrm{d}}{\mathrm{d}t}\int\limits_V s'^2_{\mathrm{tot}}\,\mathrm{d}V}_{\text{change}} + \underbrace{\int\limits_A \left(\boldsymbol{u} s'^2_{\mathrm{tot}} - K_h \boldsymbol{\nabla} s'^2_{\mathrm{tot}}\right)\cdot \mathrm{d}\boldsymbol{A}}_{\text{boundary transport}} = \underbrace{-\int\limits_V \chi_s\,\mathrm{d}V}_{\text{mixing}} \tag{B2}$$

(MacCready et al., 2018; Burchard et al., 2019), where A is the boundary of the estuary towards the river and the ocean, $\boldsymbol{u}$ is the velocity vector at the open boundary and $\mathrm{d}\boldsymbol{A}$ is the normal vector orthogonal to the area element A pointing out of the estuary, see details in Li et al. (2018). While the volume integrated mixing is the only sink term in (B2), an explicit source does not exist. Instead variance may enter the estuary via the boundary transport term as freshwater from the river and as saline water from the adjacent coastal ocean.

Inserting (7) into (6), or multiplying the salinity budget equation (8) by $2s$, we obtain a budget equation for the squared salinity, which has the same mixing term as the local variance equation (B1):

$$\underbrace{\frac{\partial s^2}{\partial t}}_{\text{change}} \underbrace{+ \frac{\partial (u s^2)}{\partial x} + \frac{\partial (v s^2)}{\partial y} + \frac{\partial (w s^2)}{\partial z}}_{\text{advection}} \underbrace{- \frac{\partial}{\partial x}\left(K_h \frac{\partial s^2}{\partial x}\right) - \frac{\partial}{\partial y}\left(K_h \frac{\partial s^2}{\partial y}\right) - \frac{\partial}{\partial z}\left(K_v \frac{\partial s^2}{\partial z}\right)}_{\text{diffusion}} = - \underbrace{\chi_s}_{\text{mixing}} , \tag{B3}$$

which is the parameterised version of (6). Often, it is more handy to diagnose the budget of the squared salinity (B3) rather than the local variance (B1), since the time-variable volume-averaged salinity $\bar{s}_{\mathrm{tot}}$ does not need to be considered.

Appendix C: Elbe River estuary model

C1 Study region

The Elbe River estuary is located in northern Germany and extends over 150 km from a weir south of Hamburg to the German Bight in the North Sea . It is an M_2-dominated, mesotidal estuary at a mean tidal range of 3.0 to 3.5 m (Boehlich and Strotmann, 2008). The tidal signal is further modified throughout the spring-neap cycle. Its broad salinity range (0.5 to > 30 g/kg within the model domain), medium discharge intensity of about 800 m^3/s on a multi-decadal average (Strotmann, 2017), and relatively simple, funnel-shaped, single-channel geometry make this estuary an ideal example for the illustration of basic estuarine mixing dynamics. Further, the navigational channel is subject to intensive dredging measures, comparable to other estuaries under high anthropogenic maintenance, and surrounded by extensive tidal flats.

The Elbe is a partially mixed estuary with a medium stratification intensity as shown for the analysis period of April 2024 in Fig. C1b,c, where the spring-neap averaged surface to bottom salinity difference amounts to up to 6-7 g/kg, and the salt intrusion reaches more than 50 km up-estuary. It displays a clear two-layer exchange flow pattern (see Fig. C1d).

A more detailed description of the Elbe River estuary can be found in Burchard et al. (2004), Reese et al. (2024), and Burchard et al. (2025).

C2 Numerical model and setup

The three-dimensional numerical model data used for all Elbe River examples in this paper was created with the General Estuarine Transport Model (GETM; Burchard and Bolding, 2002; Klingbeil and Burchard, 2013). For turbulence closure, GETM is coupled to the General Ocean Turbulence Model (GOTM; Burchard et al., 1999; Li et al., 2021), here using a second-order, algebraic closure for a k-ε parameterization (Umlauf and Burchard, 2005).

The specific Elbe River estuary setup used here is a derivative of the setup presented in Reese et al. (2024) with an increased horizontal (2404×397 cells with a mean resolution of 80 m in along-channel direction and 98 m in cross-channel direction) and vertical (40 adaptive layers) grid resolution and a new simulation period covering the year 2024. As in Reese et al. (2024), it uses a curvilinear grid with thalweg-following and cross-channel grid lines, resulting in horizontal grid cells of variable size, where the finest resolution is achieved within the navigational channel. The model domain is limited in upstream direction by the location of a weir that marks the end of the upstream tidal intrusion, and in downstream direction by an open boundary within the German Bight. The setup topography was created from a dataset from the year 2022 (Wasserstraßen- und Schifffahrtsamt Hamburg, 2024) that was expanded along the outer regions of the model domain via interpolation of additional datasets (Sievers et al., 2020; Wasserstraßen- und Schifffahrtsamt Hamburg, 2011; Wasserstraßen- und Schifffahrtsamt Weser-Jade-Nordsee, 2023).

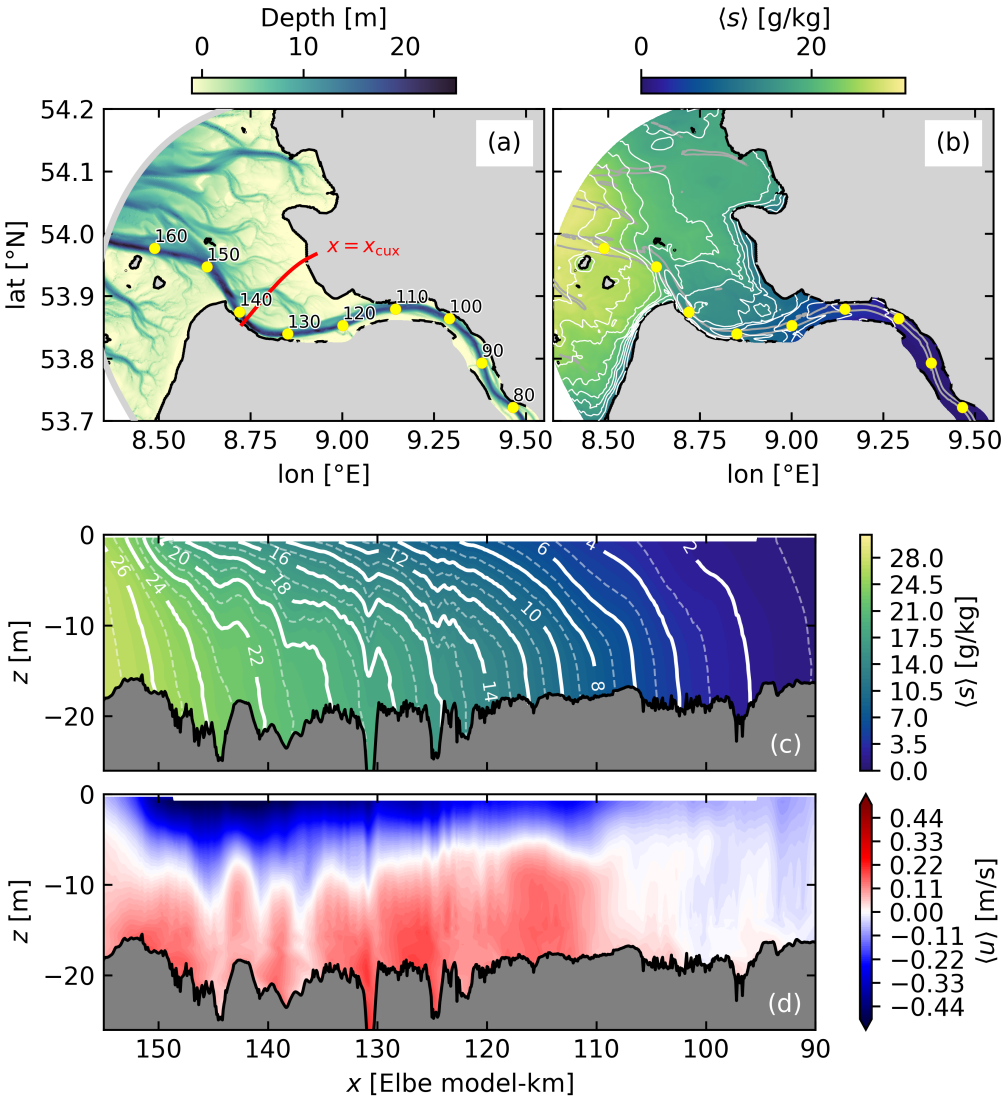

Figure C1. Overview of the numerical simulation of the Elbe River estuary. (a) Downstream section of the setup topography, showing the open boundary in the German Bight as a bold grey line, the distance from the upstream boundary as yellow dots in km, and the location of the cross-channel transect used for the analysis in Fig. 2 as a red line. (b) Average surface salinity. White lines indicate even salinities. (c) Average salinity along the thalweg of the navigational channel. Solid (dashed) white lines indicate even (odd) salinities. (d) Estuarine circulation in terms of the tidally averaged along-channel velocity $\langle u \rangle$ along the thalweg of the navigational channel, where red shading indicates an inflow into the estuary and blue shading indicates an outflow towards the German Bight. In (b)-(d), the properties have been averaged for the full month of April 2024.

Overall, the Elbe River setup uses a realistic forcing. This includes initial distributions for temperature and salinity as well as tidal elevations and vertical temperature and salinity profiles along the open boundary (E.U. Copernicus Marine Service, 2024), the daily-averaged freshwater discharge at the upstream end of the model domain (Wasserstraßen- und Schifffahrtsamt Magdeburg, 2024) at a constant salinity of 0.5 g/kg, and a 1 km-resolved meteorological forcing (Norwegian Meteorological Institute, 2024).

Within the process of model validation, the intensity of the prescribed freshwater discharge was adjusted by a factor of 1.3, and the horizontal eddy diffusivity was computed as a function of grid size (Smagorinsky, 1963). These choices were made to properly reproduce the observed salinity distribution within the Elbe River estuary. In particular, the adjustment of the freshwater discharge is a common procedure due to the uncertainty of discharge data.

Appendix D: Coordinate transformation of vertical salinity equation

Neglecting horizontal turbulent fluxes, the salinity equation (8) can also be formulated as

$$\frac{\mathrm{D}s}{\mathrm{D}t} = \frac{\partial}{\partial z}\left(K_v \frac{\partial s}{\partial z}\right). \tag{D1}$$

Assuming a stable salinity stratification with $\partial s/\partial z < 0$, for every isohaline the vertical position can be given by $z = z^s(x, y, s, t)$ such that (D1) can be multiplied by $\partial z^s/\partial s$ to yield

$$\underbrace{\frac{\partial z^s}{\partial s}\frac{\mathrm{D}s}{\mathrm{D}t}}_{=u_{\mathrm{dia},z}} = \frac{\partial}{\partial s}\underbrace{\left(K_v \frac{\partial s}{\partial z}\right)}_{=-j_{\mathrm{dia},z}} \tag{D2}$$

and $u_{\mathrm{dia},z}$ (the diahaline velocity per unit horizontal area) can be obtained from

$$w = \frac{\mathrm{D}z}{\mathrm{D}t} = \frac{\partial z^s}{\partial t} + u\frac{\partial z^s}{\partial x} + v\frac{\partial z^s}{\partial y} + \underbrace{\frac{\partial z^s}{\partial s}\frac{\mathrm{D}s}{\mathrm{D}t}}_{=u_{\mathrm{dia},z}}. \tag{D3}$$

Note that the diahaline fluxes $u_{\mathrm{dia},z}$ and $j_{\mathrm{dia},z}$ are defined positive upwards here, whereas they are usually defined positive up-gradient in the literature. For almost flat isohalines $u_{\mathrm{dia},z} \approx w - \frac{\partial z^s}{\partial t}$ can be interpreted as the vertical velocity relative to the moving isohalines. Due to the neglect of horizontal turbulent fluxes, the diahaline diffusive salt flux per unit horizontal area $j_{\mathrm{dia},z}$ in (D2) is identical to the vertical turbulent salt flux. Henell et al. (2023) and Reese et al. (2024) demonstrated that relation (D2) approximately holds also in realistic estuarine cases where horizontal turbulent fluxes are present. Moreover, relation (D2) also holds for arbitrary salinity distributions including inversions, based on generalised definitions of $u_{\mathrm{dia},z}$ and $j_{\mathrm{dia},z}$ (Klingbeil and Henell, 2023).

Appendix E: Calibration of two-equation turbulence closure models

After carrying out a second-moment closure as briefly described in Sec. 5.2.1 and presented in more detail by Burchard and Bolding (2001) and Umlauf and Burchard (2005) and applying the boundary layer assumption (vertical gradients are much

larger than horizontal gradients), the closure results in the down-gradient parameterisation of momentum,

$$[\tilde{u}\tilde{w}] = -A_v \frac{\partial u}{\partial z}, \quad [\tilde{v}\tilde{w}] = -A_v \frac{\partial v}{\partial z}, \tag{E1}$$

with the eddy viscosity A_v, and the down-gradient parameterisation for turbulent tracer flux (7), with the following relation for the eddy viscosity A_v and the eddy diffusivity K_v:

$$A_v = c_\mu(\mathrm{Ri})\frac{k^2}{\varepsilon}, \qquad K_v = c'_\mu(\mathrm{Ri})\frac{k^2}{\varepsilon}, \tag{E2}$$

with the non-dimensional stability functions c_μ and c'_μ depending in the case of quasi-equilibrium stability functions (Galperin et al., 1988) on the non-dimensional gradient-Richardson number Ri, the turbulent kinetic energy per unit mass, k, and its dissipation rate, ε. The definition of the gradient Richardson number

$$\mathrm{Ri} = \frac{N^2}{S_v^2} \tag{E3}$$

is given with the squared shear frequency $N^2 = \partial b/\partial z$, the squared vertical shear $S_v^2 = (\partial u/\partial z)^2 + (\partial v/\partial z)^2$. The stability functions c_μ and c'_μ include the entire second-moment closure (Burchard and Bolding, 2001).

For the case of two-equation turbulence closure models the full transport equations for k and ε are calculated (Rodi, 1987). Instead of the dissipation rate equation, other length-scale related properties such as the turbulence frequency $\omega = \varepsilon/k$ could be modelled, following the generic length scale (GLS) approach by Umlauf and Burchard (2003). The k-ε model, as it is typically used in three-dimensional coastal ocean models, is of the following form:

$$\begin{aligned}
\frac{\partial k}{\partial t} + \frac{\partial (uk)}{\partial x} + \frac{\partial (vk)}{\partial y} + \frac{\partial (wk)}{\partial z} - \frac{\partial}{\partial z}\left(\frac{A_v}{\sigma_k}\frac{\partial k}{\partial z}\right) &= P + B - \varepsilon, \\
\frac{\partial \varepsilon}{\partial t} + \frac{\partial (u\varepsilon)}{\partial x} + \frac{\partial (v\varepsilon)}{\partial y} + \frac{\partial (w\varepsilon)}{\partial z} - \frac{\partial}{\partial z}\left(\frac{A_v}{\sigma_\varepsilon}\frac{\partial \varepsilon}{\partial z}\right) &= \frac{\varepsilon}{k}\left(c_1 P + c_3 B - c_2 \varepsilon\right),
\end{aligned} \tag{E4}$$

with the shear production $P = A_v S_v^2$, and the vertical buoyancy flux $B = -K_v N^2$. In (E4), c_1, c_2, c_3, σ_k and σ_ε are empirical parameters. The horizontal diffusive transport of k and ε is generally ignored. To demonstrate how these two-equation turbulence closure models are calibrated to predict the correct response of mixing to stratification and shear, the transport equations for k and ε are analysed for homogenous shear-layers where the advective and diffusive transport-divergence terms vanish. Necessary conditions for equilibrium solutions of (E4) are found by setting the left-hand sides to zero, such that (E4) can be transformed to

$$\left.\begin{aligned} P + B - \varepsilon &= 0 \\ c_1 P + c_3 B - c_2 \varepsilon &= 0 \end{aligned}\right\} \quad \Rightarrow \quad \frac{c_1 - c_2}{c_3 - c_2} = \frac{c'_\mu(\mathrm{Ri_{st}})}{c_\mu(\mathrm{Ri_{st}})} \cdot \mathrm{Ri_{st}}, \tag{E5}$$

with the steady-state gradient Richardson number $\mathrm{Ri_{st}}$ denoting the gradient Richardson number for the stationary solution. To obtain the result of (E5), first ε was eliminated. With the well-calibrated parameters $c_1 = 1.44$ and $c_2 = 1.92$ (Rodi, 1987) and $\mathrm{Ri_{st}} = 0.25$ (Schumann and Gerz, 1995) eq. (E5) provides an implicit non-linear equation to calibrate c_3 which determines the

damping effect of stratification on turbulence (Burchard and Bolding, 2001). For the second-moment closure by Cheng et al. (2002) this leads to $c_3 = -0.74$ (Umlauf and Burchard, 2005). It can be shown that for a large gradient Richardson number with $\mathrm{Ri} > \mathrm{Ri}_{\mathrm{st}}$ turbulence is damped due to stable stratification and vice versa (Burchard and Bolding, 2001). This means that an increased steady-state gradient Richardson number with $\mathrm{Ri}_{\mathrm{st}} > 0.25$ will lead to increased turbulence for a given Ri and vice versa (Umlauf and Burchard, 2005). This principle has been used by Ralston et al. (2017) to decrease physical mixing by substantially lowering $\mathrm{Ri}_{\mathrm{st}}$ in order to account for the too high numerical mixing of an estuarine model, see Sec. 5.2.2. Interestingly, steady-state solutions of (E4) under the neglect of transport divergences are also provided by

$$\Gamma = \left(-\frac{B}{\varepsilon}\right)_{\mathrm{st}} = \frac{c_2 - c_1}{c_1 - c_3} \quad \text{and} \quad \mathrm{Rf}_{\mathrm{st}} = \left(-\frac{B}{P}\right)_{\mathrm{st}} = \frac{c_2 - c_1}{c_2 - c_3}. \tag{E6}$$

For the settings of $c1$, c_2 and c_3 given above, a mixing efficiency of $\Gamma = 0.21$ and a steady-state flux Richardson number of $\mathrm{Rf}_{\mathrm{st}} = 0.17$ result (both close to the generic values of $\Gamma = 0.2$ and $\mathrm{Rf}_{\mathrm{st}} = 0.15$ by Osborn, 1980), see the derivations by Umlauf (2009).

Appendix F: Derivations for numerical mixing example

F1 Discretisation of the one-dimensional advection-diffusion equation

To illustrate the quantification of physical and numerical mixing, the simple case of the one-dimensional advection-diffusion equation and its discretisation by means of a first-order upstream scheme for the advection term and a central-difference scheme for the diffusion term is examined here. The one-dimensional advection-diffusion equation is of the following form:

$$\frac{\partial s}{\partial t} + u\frac{\partial s}{\partial x} - K_h\frac{\partial^2 s}{\partial x^2} = 0, \tag{F1}$$

with the constant advection velocity u and the positive and constant physical diffusivity $K_h > 0$. Multiplying (F1) by $2s$ results in the one-dimensional version of (B3):

$$\frac{\partial s^2}{\partial t} + u\frac{\partial s^2}{\partial x} - K_h\frac{\partial^2 s^2}{\partial x^2} = \underbrace{-2K_h\left(\frac{\partial s}{\partial x}\right)^2}_{\chi_s}, \tag{F2}$$

with the physical mixing χ_s on the right-hand side as a sink term. For $u > 0$, a straight-forward explicit-in-time discretisation for (F1) with constant time step Δt and constant spatial increment Δx is given by

$$\frac{s_i^{n+1} - s_i^n}{\Delta t} + u\frac{s_i^n - s_{i-1}^n}{\Delta x} - K_h\frac{s_{i+1}^n - 2s_i^n + s_{i-1}^n}{\Delta x^2} = 0, \tag{F3}$$

with a first-order upstream discretisation for the advection term and a central-difference discretisation for the diffusion term. In (F3), the subscripts i indicate the spatial increment and the superscripts n indicate the number of the time step. For a negative velocity $u < 0$, the upstream discretisation of the advection term would simply mean to exchange s_{i-1}^n by s_{i+1}^n. The scheme is numerically stable for a Courant number of $\mu = |u|\Delta t/\Delta x \leq 1$ and the diffusion number $\nu = K_h\Delta t/\Delta x^2 \leq \frac{1}{2}$. Multiplication

of (F3) by $s_i^{n+1}+s_i^n$ (equivalent to the multiplication of (F1) by $2s$) and subsequent reorganisation results in a diagnostic equation for the advection and diffusion of s^2, as reproduced by the discretisation of the advection-diffusion equation (F1):

$$\frac{\left(s_i^{n+1}\right)^2-\left(s_i^n\right)^2}{\Delta t}+u\frac{\left(s_i^n\right)^2-\left(s_{i-1}^n\right)^2}{\Delta x}-K_h\frac{\left(s_{i+1}^n\right)^2-2\left(s_i^n\right)^2+\left(s_{i-1}^n\right)^2}{\Delta x^2}=$$

$$\underbrace{-2K_h\left\{(2\nu+2\mu)\left(\frac{s_{i+1}^n-s_{i-1}^n}{2\Delta x}\right)^2+\left(\frac{1}{2}-\nu-\frac{1}{2}\mu\right)\left(\frac{s_{i+1}^n-s_i^n}{\Delta x}\right)^2+\left(\frac{1}{2}-\nu-\frac{3}{2}\mu\right)\left(\frac{s_i^n-s_{i-1}^n}{\Delta x}\right)^2\right\}}_{\text{discrete physical mixing},\,\chi_{s,\mathrm{phy},i}} \tag{F4}$$

$$\underbrace{-2\frac{u\Delta x}{2}(1-\mu)\left(\frac{s_i^n-s_{i-1}^n}{\Delta x}\right)^2}_{\text{numerical mixing},\,\chi_{s,\mathrm{num},i}}.$$

A step-by-step derivation of (F4) is given in Sec. F2. The left-hand side of (F4) is the discretisation of the advection and diffusion of s^2 and the first term on the right-hand side is a consistent discretisation of the physical mixing, where the non-dimensional numerical parameters μ and ν determine the weights for the composition of the discrete squared salinity gradient by means of the discrete values s_{i+1}^n, s_i^n and s_{i-1}^n. Although this term partially depends on numerical parameters, we associate it with physical mixing, since it is proportional to the eddy diffusivity K_h. The second term on the right-hand side is a sink term for stable conditions with $0\le\mu\le1$, and is therefore called the numerical mixing term (Burchard and Rennau, 2008). With the numerical diffusivity $K_{\mathrm{num}}=\frac{1}{2}u\Delta x\,(1-\mu)$ it has a similar structure as the physical mixing, being twice the diffusivity times the tracer-gradient square.

F2 Derivation of physical and numerical mixing for the one-dimensional advection-diffusion equation

Here we show the step-by-step calculation of the physical and numerical mixing for the advection-diffusion equation with first-order upstream (FOU) discretisation for advection and central difference discretisation for diffusion (F3), which is the starting point here:

$$\frac{s_i^{n+1}-s_i^n}{\Delta t}+u\frac{s_i^n-s_{i-1}^n}{\Delta x}-K_h\frac{s_{i+1}^n-2s_i^n+s_{i-1}^n}{\Delta x^2}=0. \tag{F5}$$

Multiplication of (F5) by $s_i^{n+1}+s_i^n$ results in

$$\frac{\left(s_i^{n+1}\right)^2-\left(s_i^n\right)^2}{\Delta t}+u\underline{\left(s_i^{n+1}+s_i^n\right)}\frac{s_i^n-s_{i-1}^n}{\Delta x}-K_h\underline{\left(s_i^{n+1}+s_i^n\right)}\frac{s_{i+1}^n-2s_i^n+s_{i-1}^n}{\Delta x^2}=0, \tag{F6}$$

where we mark changes from step to step by an underline. Substitution of

$$\begin{aligned} s_i^{n+1} &= s_i^n-\mu\left(s_i^n-s_{i-1}^n\right)+\nu\left(s_{i+1}^n-2s_i^n+s_{i-1}^n\right) \\ &= \nu s_{i+1}^n+(1-\mu-2\nu)s_i^n+(\mu+\nu)s_{i-1}^n \end{aligned} \tag{F7}$$

with the Courant number $\mu = u\Delta t/\Delta x$ and the stability number for diffusion $\nu = K_h\Delta t/\Delta x^2$ gives

$$\begin{aligned}
&\frac{\left(s_i^{n+1}\right)^2 - \left(s_i^n\right)^2}{\Delta t} \\
&+\frac{u}{\Delta x}\left(\underline{\nu s_{i+1}^n + (2-\mu-2\nu)s_i^n + (\mu+\nu)s_{i-1}^n}\right)\left(s_i^n - s_{i-1}^n\right) \\
&-\frac{K_h}{\Delta x^2}\left(\underline{\nu s_{i+1}^n + (2-\mu-2\nu)s_i^n + (\mu+\nu)s_{i-1}^n}\right)\left(s_{i+1}^n - 2s_i^n + s_{i-1}^n\right) = 0.
\end{aligned} \tag{F8}$$

$$\begin{aligned}
&\frac{\left(s_i^{n+1}\right)^2 - \left(s_i^n\right)^2}{\Delta t} \\
&+\frac{u}{\Delta x}\Big(\underline{\nu s_{i+1}^n s_i^n + (2-\mu-2\nu)(s_i^n)^2 + (\mu+\nu)s_{i-1}^n s_i^n} \\
&\quad\underline{-\nu s_{i+1}^n s_{i-1}^n + (-2+\mu+2\nu)s_i^n s_{i-1}^n + (-\mu-\nu)(s_{i-1}^n)^2}\Big) \\
&-\frac{K_h}{\Delta x^2}\Big(\underline{\nu(s_{i+1}^n)^2 + (2-\mu-2\nu)s_i^n s_{i+1}^n + (\mu+\nu)s_{i-1}^n s_{i+1}^n} \\
&\quad\underline{-2\nu s_{i+1}^n s_i^n + (-4+2\mu+4\nu)(s_i^n)^2 + (-2\mu-2\nu)s_i^n s_{i-1}^n} \\
&\quad\underline{+\nu s_{i+1}^n s_{i-1}^n + (2-\mu-2\nu)s_i^n s_{i-1}^n + (\mu+\nu)(s_{i-1}^n)^2}\Big) = 0.
\end{aligned} \tag{F9}$$

Reordering gives

$$\begin{aligned}
&\frac{\left(s_i^{n+1}\right)^2 - \left(s_i^n\right)^2}{\Delta t} = \\
&-\frac{u}{\Delta x}\Big(\nu s_{i+1}^n s_i^n + (2-\mu-2\nu)(s_i^n)^2 + (-2+\underline{2}\mu+\underline{3}\nu)s_{i-1}^n s_i^n \\
&\quad -\nu s_{i+1}^n s_{i-1}^n + (-\mu-\nu)(s_{i-1}^n)^2\Big) \\
&+\frac{K_h}{\Delta x^2}\Big(\nu(s_{i+1}^n)^2 + (2-\mu-\underline{4}\nu)s_i^n s_{i+1}^n + (\mu+\underline{2}\nu)s_{i-1}^n s_{i+1}^n \\
&\quad +(-4+2\mu+4\nu)(s_i^n)^2 + (2-\underline{3}\mu-\underline{4}\nu)s_i^n s_{i-1}^n + (\mu+\nu)(s_{i-1}^n)^2\Big).
\end{aligned} \tag{F10}$$

Adding on both sides

$$+\frac{u}{\Delta x}\left((s_i^n)^2-(s_{i-1}^n)^2\right)-\frac{K_h}{\Delta x^2}\left((s_{i+1}^n)^2-2(s_i^n)^2+(s_{i-1}^n)^2\right) \tag{F11}$$

gives

$$\begin{aligned}
&\frac{\left(s_i^{n+1}\right)^2-(s_i^n)^2}{\Delta t}+\underline{\frac{u}{\Delta x}\left((s_i^n)^2-(s_{i-1}^n)^2\right)-\frac{K_h}{\Delta x^2}\left((s_{i+1}^n)^2-2(s_i^n)^2+(s_{i-1}^n)^2\right)}= \\
&-\frac{u}{\Delta x}\Big(\nu s_{i+1}^n s_i^n+(\underline{1}-\mu-2\nu)(s_i^n)^2+(-2+2\mu+3\nu)s_{i-1}^n s_i^n \\
&\quad -\nu s_{i+1}^n s_{i-1}^n+(\underline{1}-\mu-\nu)(s_{i-1}^n)^2\Big) \\
&+\frac{K_h}{\Delta x^2}\Big((\underline{-1}+\nu)(s_{i+1}^n)^2+(2-\mu-4\nu)s_i^n s_{i+1}^n+(\mu+2\nu)s_{i-1}^n s_{i+1}^n \\
&\quad +(\underline{-2}+2\mu+4\nu)(s_i^n)^2+(2-3\mu-4\nu)s_i^n s_{i-1}^n+(\underline{-1}+\mu+\nu)(s_{i-1}^n)^2\Big).
\end{aligned} \tag{F12}$$

Eq. (F12) is the diagnostic discrete equation for the advection-diffusion equation of squared salinity, where the right-hand side shows the total discrete mixing, consisting of a discretisation of the physical mixing plus contributions from numerical mixing. To differentiate numerical and physical mixing, we split the right-hand side into a purely advective contribution (only containing $u/\Delta x$ and μ) and the remainder:

$$\begin{aligned}
&\frac{\left(s_i^{n+1}\right)^2-(s_i^n)^2}{\Delta t}+\frac{u}{\Delta x}\left((s_i^n)^2-(s_{i-1}^n)^2\right)-\frac{K_h}{\Delta x^2}\left((s_{i+1}^n)^2-2(s_i^n)^2+(s_{i-1}^n)^2\right)= \\
&-\frac{u}{\Delta x}\left((1-\mu)(s_i^n)^2+(-2+2\mu)s_{i-1}^n s_i^n+(1-\mu)(s_{i-1}^n)^2\right) \\
&\underline{-\nu\frac{u}{\Delta x}\left(s_{i+1}^n s_i^n-2(s_i^n)^2+3s_{i-1}^n s_i^n-s_{i+1}^n s_{i-1}^n-(s_{i-1}^n)^2\right)} \\
&+\frac{K_h}{\Delta x^2}\Big((-1+\nu)(s_{i+1}^n)^2+(2-\mu-4\nu)s_i^n s_{i+1}^n+(\mu+2\nu)s_{i-1}^n s_{i+1}^n \\
&\quad +(-2+2\mu+4\nu)(s_i^n)^2+(2-3\mu-4\nu)s_i^n s_{i-1}^n+(-1+\mu+\nu)(s_{i-1}^n)^2\Big).
\end{aligned} \tag{F13}$$

Noting that

$$\nu\frac{u}{\Delta x}=\mu\frac{K_h}{\Delta x^2} \tag{F14}$$

and reformulating the purely advective term, we obtain

$$\begin{aligned}
&\frac{\left(s_i^{n+1}\right)^2-(s_i^n)^2}{\Delta t}+\frac{u}{\Delta x}\left((s_i^n)^2-(s_{i-1}^n)^2\right)-\frac{K_h}{\Delta x^2}\left((s_{i+1}^n)^2-2(s_i^n)^2+(s_{i-1}^n)^2\right)= \\
&-\frac{u}{\Delta x}\underline{(1-\mu)}\left((s_i^n)^2-2s_{i-1}^n s_i^n+(s_{i-1}^n)^2\right) \\
&+\frac{K_h}{\Delta x^2}\Big((-1+\nu)(s_{i+1}^n)^2+(2-\underline{2}\mu-4\nu)s_i^n s_{i+1}^n+(\underline{2}\mu+2\nu)s_{i-1}^n s_{i+1}^n \\
&\quad+(-2+\underline{4}\mu+4\nu)(s_i^n)^2+(2-\underline{6}\mu-4\nu)s_i^n s_{i-1}^n+(-1+\underline{2}\mu+\nu)(s_{i-1}^n)^2\Big).
\end{aligned} \tag{F15}$$

Now the right-hand side will be expressed as gradient-squared terms. This is simple for the advective term. For the diffusive term, we apply the following Ansatz to express it as a linear combination of the three possible discrete gradient-square terms:

$$\begin{aligned}
&a\left(\frac{s_{i+1}^n-s_i^n}{\Delta x}\right)^2+b\left(\frac{s_i^n-s_{i-1}^n}{\Delta x}\right)^2+c\left(\frac{s_{i+1}^n-s_{i-1}^n}{2\Delta x}\right)^2= \\
&\frac{1}{\Delta x^2}\Big[\left(a+\frac{c}{4}\right)(s_{i+1})^2+(a+b)\,(s_i^n)^2+\left(b+\frac{c}{4}\right)(s_{i-1})^2 \\
&\quad-2a s_{i+1}^n s_i^n-2b s_i^n s_{i-1}^n-\frac{c}{2}s_{i+1}^n s_{i-1}^n\Big]
\end{aligned} \tag{F16}$$

Comparison of coefficients results in

$$\begin{aligned}
&a+\frac{c}{4}=-1+\nu, \qquad a+b=-2+4\mu+4\nu, \quad b+\frac{c}{4}=-1+2\mu+\nu, \\
&-2a=2-2\mu-4\nu, \quad -2b=2-6\mu-4\nu, \qquad -\frac{c}{2}=2\mu+2\nu,
\end{aligned} \tag{F17}$$

with the solution

$$a=-1+\mu+2\nu, \quad b=-1+3\mu+2\nu, \quad c=-4\mu-4\nu. \tag{F18}$$

With this, (F15) can be expressed as

$$\frac{\left(s_i^{n+1}\right)^2-\left(s_i^n\right)^2}{\Delta t}+\frac{u}{\Delta x}\left((s_i^n)^2-(s_{i-1}^n)^2\right)-\frac{K_h}{\Delta x^2}\left((s_{i+1}^n)^2-2(s_i^n)^2+(s_{i-1}^n)^2\right)=$$

$$-u\Delta x(1-\mu)\left(\frac{s_i^n-s_{i-1}^n}{\Delta x}\right)^2$$

$$+K_h\left((-1+\mu+2\nu)\left(\frac{s_{i+1}^n-s_i^n}{\Delta x}\right)^2+(-1+3\mu+2\nu)\left(\frac{s_i^n-s_{i-1}^n}{\Delta x}\right)^2\right.$$

$$\left.+(-4\mu-4\nu)\left(\frac{s_{i+1}^n-s_{i-1}^n}{2\Delta x}\right)^2\right), \tag{F19}$$

which can be reformulated as

$$\frac{\left(s_i^{n+1}\right)^2-\left(s_i^n\right)^2}{\Delta t}+\frac{u}{\Delta x}\left((s_i^n)^2-(s_{i-1}^n)^2\right)-\frac{K_h}{\Delta x^2}\left((s_{i+1}^n)^2-2(s_i^n)^2+(s_{i-1}^n)^2\right)=$$

$$-2u\frac{\Delta x}{2}(1-\mu)\left(\frac{s_i^n-s_{i-1}^n}{\Delta x}\right)^2$$

$$-2K_h\left[\left(\frac{1}{2}-\frac{\mu}{2}-\nu\right)\left(\frac{s_{i+1}^n-s_i^n}{\Delta x}\right)^2+\left(\frac{1}{2}-\frac{3}{2}\mu-\nu\right)\left(\frac{s_i^n-s_{i-1}^n}{\Delta x}\right)^2\right.$$

$$\left.+(2\mu+2\nu)\left(\frac{s_{i+1}^n-s_{i-1}^n}{2\Delta x}\right)^2\right], \tag{F20}$$

and which is identical to (F4). It should be noted that for stationary problems (which must not depend on the time step Δt) such as the discrete solution of the exponential estuary in Sec. F3, the sum of all terms in (F20) containing one of the numerical parameters μ or ν is zero:

$$-2K_h\left\{(2\nu+2\mu)\left(\frac{s_{i+1}^n-s_{i-1}^n}{2\Delta x}\right)^2+\left(-\nu-\frac{1}{2}\mu\right)\left(\frac{s_{i+1}^n-s_i^n}{\Delta x}\right)^2+\left(-\nu-\frac{3}{2}\mu\right)\left(\frac{s_i^n-s_{i-1}^n}{\Delta x}\right)^2\right\}$$

$$-2\,\frac{u\Delta x}{2}\,(-\mu)\left(\frac{s_i^n-s_{i-1}^n}{\Delta x}\right)^2=0. \tag{F21}$$

F3 One-dimensional stationary estuarine example.

We demonstrate the distribution of physical and numerical mixing for a simple example of a one-dimensional stationary estuary of length L with constant cross-section A and constant discharge velocity $u>0$ (such that the river run-off is $Q_r=uA$) and constant along-estuary diffusivity $K_h>0$, being slightly simplified from Burchard (2020). Under those circumstances, the

stationary form of (F1) describes the balance,

$$\frac{\partial}{\partial x}\left(us - K_h\frac{\partial s}{\partial x}\right) = 0, \tag{F22}$$

of which the analytical solution for salinity is exponentially increasing from the river towards the ocean,

$$s(x) = s_o \exp\left(\frac{u}{K_h}(x-L)\right), \tag{F23}$$

with the ocean salinity s_o at $x = L$ and the river salinity $s_r = s_o \exp(-uL/K_h)$ at $x = 0$. The universal law of estuarine mixing (33) can be directly derived from (F23), see Sec. F4 for details.

The analytical solution (F23) and a numerical solution, obtained by iterating (F3) into a stationary state, are given in Fig. F1a. Using $i_{\max} = 20$ equidistant spatial increments results in a good numerical representation of the analytical solution with some deviations at high salinities. The universal law of estuarine mixing (33) is shown as analytical solution and numerical approximation in Fig. F1b. There, the numerically approximated physical mixing $\mathbb{m}_{\mathrm{phy},i}$ and the numerical mixing $\mathbb{m}_{\mathrm{num},i}$ are calculated as

$$\mathbb{m}_{\mathrm{phy},i} = \frac{\chi_{s,\mathrm{phy},i}}{\frac{1}{2}(s^n_{i+1} - s^n_{i-1})} A\Delta x, \quad \mathbb{m}_{\mathrm{num},i} = \frac{\chi_{s,\mathrm{num},i}}{\frac{1}{2}(s^n_{i+1} - s^n_{i-1})} A\Delta x, \tag{F24}$$

with the total mixing $\mathbb{m}_{\mathrm{tot},i}$ being the sum of the two. In (F24), the integration over a grid cell is carried out by multiplication with the grid box volume $A\Delta x$. Note that the discrete salinity classes are not equidistant in salinity space here, but defined in terms of the stationary salinity distribution on the equidistant spatial grid such that the size of the salinity classes is $\frac{1}{2}(s^n_{i+1} - s^n_{i-1})$. The numerical mixing amounts to about 12% of the total mixing for this simple estuarine example with a small tidally averaged advection velocity (Fig. F1b). Clearly, the universal law of estuarine mixing (33) is only fulfilled when considering the total mixing consisting of physical and numerical mixing. Note that for this stationary solution, the results for mixing must not depend on the time step Δt. It can indeed be shown that in this case the sum of all terms in $\chi_{s,\mathrm{phy},i}$ and $\chi_{s,\mathrm{num},i}$ of (F4) containing the numerical parameters μ and ν is exactly zero, independently of Δt, see (F21) of Sec. F2. For a simulation of a realistic estuary using a high-resolution coastal ocean model, the relation of physical to numerical mixing per salinity class is shown in Fig. 8, with the numerical mixing also being of the order of 10% of the total mixing.

F4 Analytical solution for salinity mixing per salinity class

Here, we derive the universal law of estuarine mixing directly from the analytical solution for the simple stationary one-dimensional estuary (F22) which reads

$$s(x) = s_o \exp\left(\frac{u}{K_h}(x-L)\right), \tag{F25}$$

see also (F23). This solution differs slightly from the solution given by Burchard (2020). Inverting (F25) to resolve for x gives

$$x(S) = \frac{K_h}{u}\ln\left(\frac{S}{s_o}\right) + L \tag{F26}$$

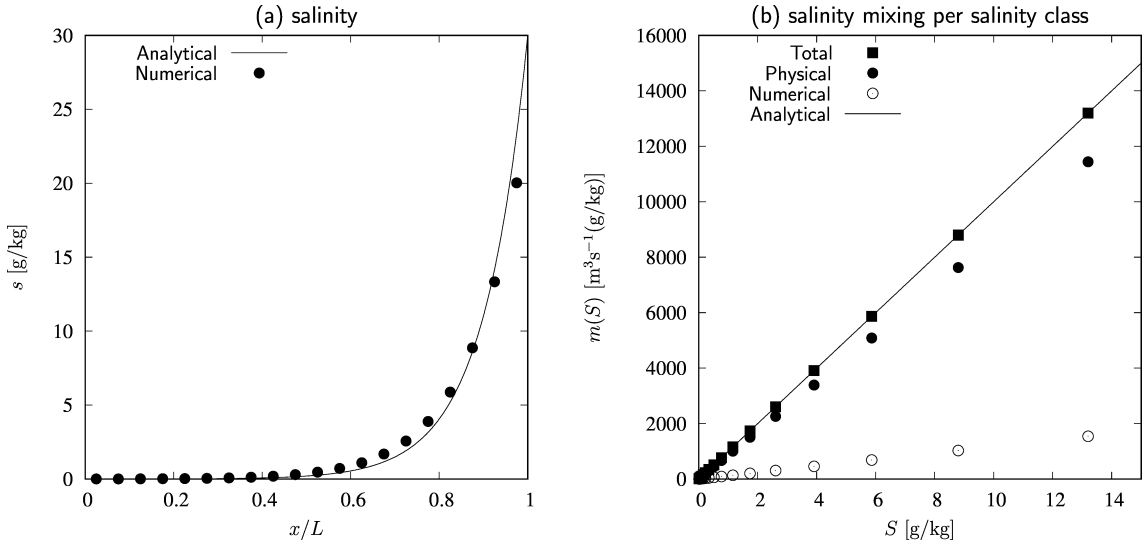

Figure F1. Analytical and numerical solutions for the one-dimensional stationary estuary with run-off velocity $u = 0.05$ m s^{-1}, $K_h = 500$ m^{2}s^{-1}, $L = 100$ km and $A = 10000$ m^2 (such that the run-off is $Q_r = uA = 500$ m^{3}s^{-1} and the river salinity is $s_r = 1.4 \cdot 10^{-3}$ g/kg). The numerical solution is carried out for $i_{\max} = 20$ equidistant spatial increments of $\Delta x = L/i_{\max}$. (a) Analytical solution (F23) and numerical solution (bullets) for salinity s as function of non-dimensional estuarine length x/L. (b) Analytical solution (33) and numerical results for the salinity mixing per salinity class $m(S)$: Total mixing (squares), physical mixing $\mathtt{m}_{\mathrm{phy},i}$ (bullets) and numerical mixing $\mathtt{m}_{\mathrm{num},i}$ (circles).

where S is now used as the salinity coordinate. The volume-integrated mixing $M(S)$ for the monotone salinity distribution (F25) can be calculated as the integral over the local mixing (using A as cross-sectional area),

$$\mathbb{M}(S) = A \int_0^{x(S)} 2K_h \left(\frac{\partial s(x')}{\partial x'}\right)^2 \mathrm{d}x'. \tag{F27}$$

Inserting the square of the x-derivative of (F25) into (F27) gives

$$\begin{aligned} \mathbb{M}(S) &= 2As_o^2 \frac{u^2}{K_h} \int_0^{x(S)} \exp\left(2\frac{u}{K_h}(x' - L)\right) \mathrm{d}x' = As_o^2 u \int_{-2\frac{u}{K_h}L}^{2\frac{u}{K_h}(x-L)} \exp(x')\, \mathrm{d}x' \\ &= Q_r s_o^2 \left(\exp^2\left(\frac{u}{K_h}(x-L)\right) - \exp^2\left(-\frac{u}{K_h}L\right)\right) = Q_r s_o^2 \left(\frac{S^2}{s_o^2} - \frac{s_r^2}{s_o^2}\right) = Q_r\left(S^2 - s_r^2\right), \end{aligned} \tag{F28}$$

where (F26) and $Q_r = Au$ have been used. Finally, this yields the mixing per salinity class,

$$\mathtt{m}(S) = \frac{\partial \mathbb{M}(S)}{\partial S} = 2SQ_r, \tag{F29}$$

which is identical to (33). Following Lorenz et al. (2021), and in analogy to their case of freshwater input across the ocean surface due to precipitation, the additional term $-Q_r s_r^2$ in (F28) represents the corresponding boundary flux of S^2 at the river end and reduces the mixing in the interior.

Symbol	Meaning	Unit	Equation
A	area of transect or isohaline	m	(B2)
A_v	vertical eddy viscosity	$m^2 s^{-1}$	(E2)
b	buoyancy	$m\,s^{-2}$	(13)
b_0	Kolmogorov constant for scalar variance	-	(41)
b_x	longitudinal buoyancy gradient	s^{-2}	(13)
B	vertical turbulent buoyancy flux	$m^2 s^{-3}$	(E4)
D	water depth	m	(13)
g	gravitational acceleration	$m\,s^{-2}$	(E2)
F_{dia}	diahaline total salt transport	$m^3 s^{-1}$(g/kg)	(30)
$f_{\mathrm{dia},z}$	vertical total salinity flux	$m\,s^{-1}$(g/kg)	(27)
J_{dia}	diahaline diffusive salt transport	$m^3 s^{-1}$(g/kg)	(30)
$j_{\mathrm{dia},z}$	vertical diahaline diffusive salinity flux	$m\,s^{-1}$(g/kg)	(26)
k	turbulent kinetic energy (TKE) per unit mass	$m^2 s^{-2}$	(E2)
$\mathcal{K}$	wave number	m^{-1}	(41)
$\mathcal{K}_\eta$	Kolmogorov wave number	m^{-1}	(41)
K_h, K_v	horizontal, vertical eddy diffusivity	$m^2 s^{-1}$	(7)
L_O	Ozmidov scale	m	(39)
L_T	Thorpe scale	m	(40)
m	local salinity mixing per salinity class	$m\,s^{-1}$(g/kg)	(28)
$\mathbb{m}$	salinity mixing per salinity class	$m^3 s^{-1}$(g/kg)	(33)
$\mathbb{M}$	volume-integrated salinity mixing	$m^3 s^{-1}$(g/kg)^2	(19)
Mc	salinity mixing completeness	-	(25)
N	buoyancy frequency	s^{-1}	(E2)
P	shear production	$m^2 s^{-3}$	(E4)
P_s	stirring of micro-structure salinity variance (typically $= \chi_s$)	$m\,s^{-1}$(g/kg)^2	(5)
q	Total Exchange Flow (TEF) of volume	$m^3 s^{-1}$(g/kg)$^{-1}$	(15)
q_s	Total Exchange Flow (TEF) of salinity	$m^3 s^{-1}$	(15)
q_{s^2}	Total Exchange Flow (TEF) of squared salinity	$m^3 s^{-1}$(g/kg)	(15)
Q	estuarine circulation streamfunction	$m^3 s^{-1}$	(14)
Q_{dia}	inflow volume transport across isohaline	$m^3 s^{-1}$	(30)
$Q_{\mathrm{dia,in}}$	volume transport across isohaline	$m^3 s^{-1}$	(31)
$Q_{\mathrm{dia,out}}$	outflow volume transport across isohaline	$m^3 s^{-1}$	(31)
Q_{in}	inflow volume transport	$m^3 s^{-1}$	(16)
$Q_{s,\mathrm{in}}$	inflowing salt transport	$m^3 s^{-1}$(g/kg)	(16)

$Q_{s^2,\mathrm{in}}$	inflowing salt squared transport	$\mathrm{m^3 s^{-1} (g/kg)^2}$	(16)
Q_{out}	outflow volume transport	$\mathrm{m^3 s^{-1}}$	(16)
$Q_{s,\mathrm{out}}$	outflowing salt transport	$\mathrm{m^3 s^{-1} (g/kg)}$	(16)
$Q_{s^2,\mathrm{out}}$	outflowing salt squared transport	$\mathrm{m^3 s^{-1} (g/kg)^2}$	(16)
Q_r	river discharge	$\mathrm{m^3 s^{-1}}$	(18)
Q_s	estuarine circulation streamfunction for salinity	$\mathrm{m^3 s^{-1} (g/kg)}$	(14)
Q_{s^2}	estuarine circulation streamfunction for squared salinity	$\mathrm{m^3 s^{-1} (g/kg)^2}$	(14)
Q_{surf}	surface freshwater transport	$\mathrm{m^3 s^{-1}}$	(24)
Rf	flux Richardson number	-	(38)
$\mathrm{Rf}_{\mathrm{st}}$	steady-state flux Richardson number	-	(E6)
Ri	gradient Richardson number	-	(E3)
$\mathrm{Ri}_{\mathrm{st}}$	steady-state gradient Richardson number	-	(E5)
s	salinity	g/kg	(1)
S	salinity coordinate	g/kg	(32)
Si	Simpson number	-	(13)
s_{in}	inflow salinity	g/kg	(17)
$(s^2)_{\mathrm{in}}$	inflowing squared salinity	$\mathrm{(g/kg)^2}$	(17)
s_{out}	outflow salinity	g/kg	(17)
$(s^2)_{\mathrm{out}}$	outflowing squared salinity	$\mathrm{(g/kg)^2}$	(17)
s_r	river salinity	g/kg	(23)
S_{ss}	power spectral density of salinity variance	$\mathrm{m\ (g/kg)^2}$	(41)
s_{surf}	representative surface salinity	g/kg	(24)
S_v	shear frequency	$\mathrm{s^{-1}}$	(E4)
t	time coordinate	s	(2)
$u = u_1$, $v = u_2$, $w = u_3$	eastward, northward and upward velocity component	$\mathrm{m\,s^{-1}}$	(2)
$u_{\mathrm{dia},z}$	upward diahaline entrainment velocity	$\mathrm{m\,s^{-1}}$	(26)
u_*	bottom friction velocity	$\mathrm{m\,s^{-1}}$	(13)
$\mathbb{v}$	volume per salinity class	$\mathrm{m^3 (g/kg)^{-1}}$	(35)
V	estuarine volume (bounded by transect or isohaline)	$\mathrm{m^3}$	(B2)
$x = x_1$, $y = x_2$, $z = x_3$	eastward, northward and upward coordinate	m	(2)
α_N	buoyancy number	-	(E2)
χ_s	micro-structure salinity variance decay (typically $= P_s$)	$\mathrm{m\,s^{-1} (g/kg)^2}$	(1)
η	sea surface elevation	m	(12)
ε	dissipation rate of TKE	$\mathrm{m^2 s^{-3}}$	(38)
Γ	mixing efficiency	-	(E6)

κ	molecular diffusivity of salinity	$\mathrm{m^2 s^{-1}}$	(1)
μ	Courant number	-	(F4)
ν	diffusion number	-	(F4)
ρ	potential density	kg $\mathrm{m^{-3}}$	(13)
ρ_0	reference density	kg $\mathrm{m^{-3}}$	(13)

Table 2: List of major variables including their physical meaning and dimensions.

Operator	Meaning
$\check{x} = [x] + \tilde{x}$	instantaneous variable, not Reynolds-averaged
$[x]$	Reynolds-averaged variable
$\tilde{x}$	turbulent fluctuation of variable
$\bar{x}$	volume-averaged or vertically averaged variable
$x'^2 = (x - \bar{x})^2$	local variance of variable
$\langle x \rangle$	temporal average in z coordinates
$\langle x \rangle_S$	temporal average in S coordinates

Table 3: List of operators demonstrated for an arbitrary variable x.

Author contributions. HB and WRG developed the first ideas, aims and structure for this review paper. HB wrote most of the text and designed the explanatory sketches. WRG wrote the Observations section 5.1 and parts of the Introduction Sec. 1 and the Mixing processes Sec. 4. LR wrote the Sec. C on the Elbe River estuary simulations and KK wrote the derivation for the Coordinate transformation in Sec. D. Furthermore, KK checked all mathematical equations and derivations in detail. XL performed the Elbe River estuary model simulations for this review paper and LR and XL carried out the model analysis and the Elbe figures. WRG and KK implemented major changes to the structure of the manuscript. Finally, all authors reviewed, edited and corrected the entire manuscript in detail.

Competing interests. The authors declare that they have no conflict of interest.

Acknowledgements. The work of H. Burchard and K. Klingbeil is a contribution to the Collaborative Research Centre TRR 181 *Energy Transfers in Atmosphere and Ocean* (No. 274762653), funded by the German Research Foundation. We further acknowledge funding for X. Li by grant no. 03F0954F of the German Federal Ministry of Research, Technology and Space (BMFTR) as part of the DAM mission "mareXtreme", project ElbeXtreme and for L. Reese by grant no. 03F0980B of the German Federal Ministry of Research, Technology and Space (BMFTR) as part of the DAM mission "sustainMare", project CoastalFutures II. The authors are grateful for the useful comments and recommendations by Tobias Kukulka (University of Maryland, USA), Qing Li (The Hong Kong University of Science and Technology, Guangzhou, China) and Parker MacCready (University of Washington, USA). We further thank Robert Hetland (Pacific Northwest National Laboratory, USA), John Huthnance (National Oceanography Centre, UK) and an anonymous referee for their critical reviews of our original version of the manuscript.

References

Armi, L. and Farmer, D. M.: Maximal two-layer exchange through a contraction with barotropic net flow, J. Fluid Mech., 164, 27–51, 1986.

Banerjee, T., Klingbeil, K., and Danilov, S.: Discrete variance decay analysis of spurious mixing, Ocean Modell., 192, 102 460, 2024.

Becherer, J., Burchard, H., Flöser, G., Mohrholz, V., and Umlauf, L.: Evidence of tidal straining in well-mixed channel flow from microstructure observations, Geophys. Res. Lett., 38, L17 611, 2011.

Bo, T., Ralston, D. K., Garcia, A. M. P., and Geyer, W. R.: Tidal intrusion fronts, surface convergence, and mixing in an estuary with complex topography, J. Phys. Oceanogr., 54, 653–677, 2024.

Boehlich, M. J. and Strotmann, T.: The Elbe estuary, Die Küste, 74, 288–306, 2008.

Börgel, F., Karsten, S., Rummel, K., and Gräwe, U.: From weather data to river runoff: using spatiotemporal convolutional networks for discharge forecasting, Geosci. Model Devel., 18, 2005–2019, 2025.

Boyle, E., Collier, R., Dengler, A., Edmond, J., Ng, A., and Stallard, R.: On the chemical mass-balance in estuaries, Geochimica et Cosmochimica Acta, 38, 1719–1728, 1974.

Broatch, E. M. and MacCready, P.: Mixing in a salinity variance budget of the Salish Sea is controlled by river flow, J. Phys. Oceanogr., 52, 2305–2323, 2022.

Burchard, H.: A universal law of estuarine mixing, J. Phys. Oceanogr., 50, 81–93, 2020.

Burchard, H. and Bolding, K.: Comparative analysis of four second-moment turbulence closure models for the oceanic mixed layer, J. Phys. Oceanogr., 31, 1943–1968, 2001.

Burchard, H. and Bolding, K.: GETM – A General Estuarine Transport Model, Tech. Rep. EUR 20253 EN, European Commission, 2002.

Burchard, H. and Hetland, R. D.: Quantifying the contributions of tidal straining and gravitational circulation to residual circulation in periodically stratified tidal estuaries, J. Phys. Oceanogr., 40, 1243–1262, 2010.

Burchard, H. and Rennau, H.: Comparative quantification of physically and numerically induced mixing in ocean models, Ocean Modell., 20, 293–311, 2008.

Burchard, H., Bolding, K., and Villarreal, M. R.: GOTM – a general ocean turbulence model. Theory, applications and test cases, Tech. Rep. EUR 18745 EN, European Commission, 1999.

Burchard, H., Bolding, K., and Villarreal, M. R.: Three-dimensional modelling of estuarine turbidity maxima in a tidal estuary, Ocean Dyn., 54, 250–265, 2004.

Burchard, H., Hetland, R. D., Schulz, E., and Schuttelaars, H. M.: Drivers of residual estuarine circulation in tidally energetic estuaries: Straight and irrotational channels with parabolic cross section, J. Phys. Oceanogr., 41, 548–570, 2011.

Burchard, H., Schulz, E., and Schuttelaars, H. M.: Impact of estuarine convergence on residual circulation in tidally energetic estuaries and inlets, Geophys. Res. Lett., 41, 913–919, 2014.

Burchard, H., Bolding, K., Feistel, R., Gräwe, U., Klingbeil, K., MacCready, P., Mohrholz, V., Umlauf, L., and van der Lee, E. M.: The Knudsen theorem and the Total Exchange Flow analysis framework applied to the Baltic Sea, Progr. Oceanogr., 165, 268–286, 2018a.

Burchard, H., Schuttelaars, H. M., and Ralston, D. K.: Sediment trapping in estuaries, Annu. Rev. Mar. Sci., 10, 10 371–10 395, 2018b.

Burchard, H., Lange, X., Klingbeil, K., and MacCready, P.: Mixing estimates for estuaries, J. Phys. Oceanogr., 49, 631–648, 2019.

Burchard, H., Gräwe, U., Klingbeil, K., Koganti, N., Lange, X., and Lorenz, M.: Effective diahaline diffusivities in estuaries, Journal of Advances in Modeling Earth Systems, 13, 2021.

Burchard, H., Klingbeil, K., Lange, X., Li, X., Lorenz, M., MacCready, P., and Reese, L.: The relation between exchange flow and diahaline mixing in estuaries, J. Phys. Oceanogr., 55, 243–256, 2025.

Cessi, P.: The global overturning circulation, Annu. Rev. Mar. Sci., 11, 249–270, 2019.

Chang, Y., Li, X., Wang, Y. P., Klingbeil, K., Li, W., Zhang, F., and Burchard, H.: Salinity mixing in a tidal multi-branched estuary with huge and variable runoff, J. Hydrol., 634, 131 094, 2024.

Chen, S.-N. and Sanford, L. P.: Axial wind effects on stratification and longitudinal salt transport in an idealized, partially mixed estuary, J. Phys. Oceanogr., 39, 1905–1920, 2009.

Chen, S.-N., Geyer, W. R., Ralston, D. K., and Lerczak, J. A.: Estuarine exchange flow quantified with isohaline coordinates: Contrasting long and short estuaries, J. Phys. Oceanogr., 42, 748–763, 2012.

Cheng, Y., Canuto, V. M., and Howard, A. M.: An improved model for the turbulent PBL, J. Atmos. Sci., 59, 1550–1565, 2002.

Chrysagi, E., Umlauf, L., Holtermann, P., Klingbeil, K., and Burchard, H.: High-resolution simulations of submesoscale processes in the Baltic Sea: The role of storm events, J. Geophys. Res. Oceans, 126, e2020JC016 411, 2021.

Collignon, A. G. and Stacey, M. T.: Turbulence dynamics at the shoal–channel interface in a partially stratified estuary, J. Phys. Oceanogr., 43, 970–989, 2013.

Conroy, T., Sutherland, D. A., and Ralston, D. K.: Estuarine exchange flow variability in a seasonal, segmented estuary, J. Phys. Oceanogr., 50, 595–613, 2020.

Dijkstra, Y. M., Schuttelaars, H. M., and Burchard, H.: Generation of exchange flows in estuaries by tidal and gravitational eddy viscosity-shear covariance (ESCO), J. Geophys. Res. Oceans, 122, 4217–4237, 2017.

Döös, K., Meier, H. M., and Döscher, R.: The Baltic haline conveyor belt or the overturning circulation and mixing in the Baltic, AMBIO, 33, 261–266, 2004.

Drake, H. F., Shanice, B., Dussin, R., Griffies, S. M., Krasting, J. P., MacGilchrist, G. A., Stanley, G. J., Tesdal, J.-E., and Zika, J. D.: Water mass transformation budgets in finite-volume generalized vertical coordinate ocean models, J. Adv. Model. Earth Sys., 17, e2024MS004 383, 2025.

Etemad-Shahidi, A. and Imberger, J.: Anatomy of turbulence in a narrow and strongly stratified estuary, J. Geophys. Res. Oceans, 107, 7–1, 2002.

E.U. Copernicus Marine Service: Atlantic – European North West Shelf – Ocean Physics Analysis and Forecast, https://doi.org/https://doi.org/10.48670/moi-00054, accessed 18 December 2024, 2024.

Ferrari, R., Mashayek, A., McDougall, T. J., Nikurashin, M., and Campin, J.-M.: Turning ocean mixing upside down, J. Phys. Oceanogr., 46, 2239–2261, 2016.

Fischer, H. B.: Mixing and dispersion in estuaries, Annu. Rev. Fluid Mech., 8, 107–133, 1976.

Galperin, B., Kantha, L., Rosati, A., and Hassid, S.: A quasi-equilibrium turbulent energy model for geophysical flows, J. Atmos. Sci., 45, 55–62, 1988.

Gargett, A. E.: Observing turbulence with a modified acoustic Doppler current profiler, J. Atmos. Ocean. Technol., 11, 1592–1610, 1994.

Garrett, C.: Marginal mixing theories, Atmosphere-Ocean, 29, 313–339, 1991.

Garvine, R. W.: Penetration of buoyant coastal discharge onto the continental shelf: A numerical model experiment, J. Phys. Oceanogr., 29, 1892–1909, 1999.

Geyer, W. R.: The importance of suppression of turbulence by stratification on the estuarine turbidity maximum, Estuaries, 16, 113–125, 1993.

Geyer, W. R.: Influence of wind on dynamics and flushing of shallow estuaries, Estuarine Coast. Shelf Sci., 44, 713–722, 1997.

Geyer, W. R. and MacCready, P.: The estuarine circulation, Annu. Rev. Fluid Mech., 46, 175–197, 2014.

Geyer, W. R. and Ralston, D. K.: Estuarine frontogenesis, J. Phys. Oceanogr., 45, 546–561, 2015.

Geyer, W. R., Ralston, D. K., and Holleman, R. C.: Hydraulics and mixing in a laterally divergent channel of a highly stratified estuary, J. Geophys. Res. Oceans, 122, 4743–4760, 2017.

Geyer, W. R., Ralston, D. K., and Chen, J.-L.: Mechanisms of exchange flow in an estuary with a narrow, deep channel and wide, shallow shoals, J. Geophys. Res., 125, e2020JC016 092, 2020.

Gibbs, J. W.: On the equilibrium of heterogeneous substances, Am. J. Sci., 3, 441–458, 1878.

Gibson, A. H., Hogg, A. M., Kiss, A. E., Shakespeare, C. J., and Adcroft, A. J.: Attribution of horizontal and vertical contributions to spurious mixing in an Arbitrary Lagrangian–Eulerian ocean model, Ocean Modell., 119, 45–56, 2017.

Giddings, S. N., Fong, D. A., and Monismith, S. G.: Role of straining and advection in the intratidal evolution of stratification, vertical mixing, and longitudinal dispersion of a shallow, macrotidal, salt wedge estuary, J. Geophys. Res. Oceans, 116, 2011.

Gräwe, U., Holtermann, P., Klingbeil, K., and Burchard, H.: Advantages of vertically adaptive coordinates in numerical models of stratified shelf seas, Ocean Modell., 92, 56–68, 2015.

Gräwe, U., Flöser, G., Gerkema, T., Duran-Matute, M., Badewien, T. H., Schulz, E., and Burchard, H.: A numerical model for the entire Wadden Sea: Skill assessment and analysis of hydrodynamics, J. Geophys. Res., 121, 5231–5251, 2016.

Griffies, S. M.: Fundamentals of Ocean-Climate Models, Princeton University Press, Princeton, USA, 2004.

Griffies, S. M., Pacanowski, R. C., and Hallberg, R. W.: Spurious diapycnal mixing associated with advection in a z-coordinate ocean model, Mon. Weather Rev., 128, 538–564, 2000.

Groeskamp, S., Griffies, S. M., Iudicone, D., Marsh, R., Nurser, A. G., and Zika, J. D.: The water mass transformation framework for ocean physics and biogeochemistry, Annu. Rev. Mar. Sci., 11, 271–305, 2019.

Harcourt, R. R.: An improved second-moment closure model of Langmuir turbulence, J. Phys. Oceanogr., 45, 84–103, 2015.

Henell, E., Burchard, H., Gräwe, U., and Klingbeil, K.: Spatial composition of the diahaline overturning circulation in a fjord-type, non-tidal estuarine system, J. Geophys. Res., 128, e2023JC019 862, 2023.

Hetland, R.: Relating river plume structure to vertical mixing, J. Phys. Oceanogr., 35, 1667–1688, 2005.

Hieronymus, M., Nilsson, J., and Nycander, J.: Water mass transformation in salinity–temperature space, J. Phys. Oceanogr., 44, 2547–2568, 2014.

Hofmeister, R., Beckers, J.-M., and Burchard, H.: Realistic modelling of the exceptional inflows into the central Baltic Sea in 2003 using terrain-following coordinates, Ocean Modell., 39, 233–247, 2011.

Holleman, R., Geyer, W., and Ralston, D.: Stratified turbulence and mixing efficiency in a salt wedge estuary, J. Phys. Oceanogr., 46, 1769–1783, 2016.

Holmes, R. M., Zika, J. D., Griffies, S. M., Hogg, A. M., Kiss, A. E., and England, M. H.: The geography of numerical mixing in a suite of global ocean models, J. Adv. Model. Earth Syst., 13, 2021.

Horner-Devine, A. R., Hetland, R. D., and MacDonald, D. G.: Mixing and transport in coastal river plumes, Annu. Rev. Fluid Mech., 47, 569–594, 2015.

Huang, J., Chamecki, M., Li, Q., and Chen, B.: The role of longitudinal alignment between surface and bottom forcing on the full-column turbulence mixing in the coastal ocean, Ocean Modell., p. 102637, 2025.

Huguenard, K., Valle-Levinson, A., Li, M., Chant, R., and Souza, A.: Linkage between lateral circulation and near-surface vertical mixing in a coastal plain estuary, J. Geophys. Res. Oceans, 120, 4048–4067, 2015.

Huguenard, K., Bears, K., and Lieberthal, B.: Intermittency in Estuarine Turbulence: A framework toward limiting bias in microstructure measurements, J. Atmos. Ocean. Technol., 36, 1917–1932, 2019.

Huzzey, L. M. and Brubaker, J. M.: The formation of longitudinal fronts in a coastal plain estuary, J. Geophys. Res. Oceans, 93, 1329–1334, 1988.

Ianniello, J. P.: Tidally induced residual currents in estuaries of variable breadth and depth, J. Phys. Oceanogr., 9, 962–974, 1979.

Inall, M. and Gillibrand, P.: The physics of mid-latitude fjords: a review, Geological Society, London, Special Publications, 344, 17–33, 2010.

Jay, D. A. and Musiak, J. D.: Particle trapping in estuarine tidal flows, J. Geophys. Res., 99, 20 445–20 461, 1994.

Ji, Z.-G., Hu, G., Shen, J., and Wan, Y.: Three-dimensional modeling of hydrodynamic processes in the St. Lucie Estuary, Estuarine Coast. Shelf Sci., 73, 188–200, 2007.

Kim, J., Park, K., Yang, D. R., and Hong, S.: A comprehensive review of energy consumption of seawater reverse osmosis desalination plants, Applied Energy, 254, 113 652, 2019.

Klingbeil, K. and Burchard, H.: Implementation of a direct nonhydrostatic pressure gradient discretisation into a layered ocean model, Ocean Modell., 65, 64–77, 2013.

Klingbeil, K. and Henell, E.: A rigorous derivation of the water mass transformation framework, the relation between mixing and diasurface exchange flow, and links to recent theories in estuarine research, J. Phys. Oceanogr., 53, 2953–2968, 2023.

Klingbeil, K. and Lorenz, M.: On the instantaneous salt mixing due to freshwater boundary fluxes, J. Phys. Oceanogr., 55, 809–813, 2025.

Klingbeil, K., Mohammadi-Aragh, M., Gräwe, U., and Burchard, H.: Quantification of spurious dissipation and mixing - Discrete variance decay in a Finite-Volume framework, Ocean Model., 81, 49–64, 2014.

Klingbeil, K., Lemarié, F., Debreu, L., and Burchard, H.: The numerics of hydrostatic structured-grid coastal ocean models: State of the art and future perspectives, Ocean Modell., 125, 80–105, 2018.

Klingbeil, K., Becherer, J., Schulz, E., de Swart, H. E., Schuttelaars, H. M., Valle-Levinson, A., and Burchard, H.: Thickness-Weighted Averaging in tidal estuaries and the vertical distribution of the Eulerian residual transport, J. Phys. Oceanogr., 49, 1809–1826, 2019.

Knudsen, M.: Ein hydrographischer Lehrsatz, Annalen der Hydrographie und Maritimen Meteorologie, 28, 316–320, 1900.

Kuhlbrodt, T., Griesel, A., Montoya, M., Levermann, A., Hofmann, M., and Rahmstorf, S.: On the driving processes of the Atlantic meridional overturning circulation, Rev. Geophys., 45, 2007.

Lange, X. and Burchard, H.: The relative importance of wind straining and gravitational forcing in driving exchange flows in tidally energetic estuaries, J. Phys. Oceanogr., 49, 723–736, 2019.

Lange, X., Klingbeil, K., and Burchard, H.: Inversions of estuarine circulation are frequent in a weakly tidal estuary with variable wind forcing and seaward salinity fluctuations, J. Geophys. Res. Oceans, 125, e2019JC015 789, 2020.

Lavery, A. C., Geyer, W. R., and Scully, M. E.: Broadband acoustic quantification of stratified turbulence, J. Acoust. Soc. Amer., 134, 40–54, 2013.

Legay, A., Deremble, B., and Burchard, H.: Derivation and implementation of a non-local term to improve the oceanic convection representation within the k–ε parameterization, J. Adv. Model. Earth Syst., 17, e2024MS004 243, 2025.

Lemagie, E., Giddings, S. N., MacCready, P., Seaton, C., and Wu, X.: Measuring estuarine total exchange flow from discrete observations, J. Geophys. Res. Oceans, 127, e2022JC018 960, 2022.

Lerczak, J. and Geyer, W.: Modeling the lateral circulation in straight, stratified estuaries, J. Phy. Oceanogr., 34, 1410–1428, 2004.

Lesieur, M.: Turbulence in Fluids, Springer, 2008.

Li, M., Trowbridge, J., and Geyer, W. R.: Asymmetric tidal mixing due to the horizontal density gradient, J. Phys. Oceanogr., 38, 418–434, 2008.

Li, M., Radhakrishnan, S., Piomelli, U., and Geyer, W. R.: Large-eddy simulation of the tidal-cycle variations of an estuarine boundary layer, J. Geophys. Res. Oceans, 115, 2010.

Li, Q., Bruggeman, J., Burchard, H., Klingbeil, K., Umlauf, L., and Bolding, K.: Integrating CVMix into GOTM (v6. 0): A consistent framework for testing, comparing, and applying ocean mixing schemes, Geosci. Model Dev., 14, 4261–4282, 2021.

Li, X., Geyer, W. R., Zhu, J., and Wu, H.: The transformation of salinity variance: A new approach to quantifying the influence of straining and mixing on estuarine stratification, J. Phys. Oceanogr., 48, 607–623, 2018.

Li, X., Lorenz, M., Klingbeil, K., Chrysagi, E., Gräwe, U., Wu, J., and Burchard, H.: Salinity mixing and diahaline exchange flow in a large multi-outlet estuary with islands, J. Phys. Oceanogr., 52, 2111–2127, 2022.

Li, X., Chrysagi, E., Klingbeil, K., and Burchard, H.: Impact of islands on tidally dominated river plumes: A high-resolution modeling study, J. Geophys. Res.: Oceans, 129, e2023JC020 272, 2024.

Loder, T. C. and Reichard, R. P.: The dynamics of conservative mixing in estuaries, Estuaries, 4, 64–69, 1981.

Lorenz, M., Klingbeil, K., MacCready, P., and Burchard, H.: Numerical issues of the Total Exchange Flow (TEF) analysis framework for quantifying estuarine circulation, Ocean Sci., 15, 601–614, 2019.

Lorenz, M., Klingbeil, K., and Burchard, H.: Numerical study of the exchange flow of the Persian Gulf using an extended total exchange flow analysis framework, J. Geophys. Res. Oceans, 125, e2019JC015 527, 2020.

Lorenz, M., Klingbeil, K., and Burchard, H.: Impact of evaporation and precipitation on estuarine mixing, J. Phys. Oceanogr., 51, 1319–1333, 2021.

Lu, Y. and Lueck, R. G.: Using a broadband ADCP in a tidal channel. Part II: Turbulence, J. Atmos. Ocean. Technol., 16, 1568–1579, 1999.

Lui, H.-K. and Chen, C.-T. A.: Shifts in limiting nutrients in an estuary caused by mixing and biological activity, Limnol. Oceanogr., 56, 989–998, 2011.

MacCready, P.: Toward a unified theory of tidally-averaged estuarine salinity structure, Estuaries, 27, 561–570, 2004.

MacCready, P.: Calculating estuarine exchange flow using isohaline coordinates, J. Phys. Oceanogr., 41, 1116–1124, 2011.

MacCready, P. and Banas, N.: Residual Circulation, Mixing, and Dispersion, in: Treatise on Estuarine and Coastal Science (Second Edition), edited by Baird, D. and Elliott, M., pp. 92–108, Academic Press, Oxford, second edition edn., 2011.

MacCready, P. and Geyer, W. R.: Estuarine salt flux through an isohaline surface, J. Geophys. Res., 106, 11 629–11 637, 2001.

MacCready, P. and Geyer, W. R.: Advances in estuarine physics, Annu. Rev. Mar. Sci., 2, 35–58, 2010.

MacCready, P. and Geyer, W. R.: Estuarine exchange flow in the Salish Sea, J. Geophys. Res., 129, e2023JC020 369, 2024.

MacCready, P., Hetland, R. D., and Geyer, W. R.: Long-term isohaline salt balance in an estuary, Cont. Shelf Res., 22, 1591–1601, 2002.

MacCready, P., Geyer, W. R., and Burchard, H.: Estuarine exchange flow is related to mixing through the salinity variance budget, J. Phys. Oceanogr., 48, 1375–1384, 2018.

McPherson, R., Stevens, C., and O'Callaghan, J.: Turbulent scales observed in a river plume entering a fjord, J. Geophys. Res. Oceans, 124, 9190–9208, 2019.

McWilliams, J. C.: Submesoscale currents in the ocean, Proc. R. Soc. Lond., A, Math. Phys. Eng. Sci., 472, 2016.

Mellor, G. L. and Yamada, T.: A hierarchy of turbulence closure models for planetary boundary layers, J. Atmos. Sci., 31, 1791–1806, 1974.

Monismith, S. G., Burau, J. R., and Stacey, M.: Stratification dynamics and gravitational circulation in Northern San Francisco Bay, in: San Francisco Bay: the ecosystem, edited by Hollibaugh, J. T., pp. 123–153, American Association for the Advancement of Science, Pacific Division, San Francisco, 1996.

Muche, Y., Klingbeil, K., Lorenz, M., Yankovsky, A. E., and Burchard, H.: Numerical investigation of the influence of wind and tides on salt mixing and cross-shore transport in river plumes, J. Geophys. Res.: Oceans, https://doi.org/10.1029/2025JC023583, accepted for publication, 2026.

Munk, W. H.: Abyssal recipes, in: Deep sea research and oceanographic abstracts, vol. 13, pp. 707–730, Elsevier, 1966.

Munk, W. H. and Wunsch, C.: Abyssal recipes II: Energetics of tidal and wind mixing, Deep Sea Res. I, 45, 1977–2010, 1998.

Nash, J. D. and Moum, J. N.: Microstructure estimates of turbulent salinity flux and the dissipation spectrum of salinity, J. Phys. Oceanogr., 32, 2312–2333, 2002.

Nikurashin, M. and Ferrari, R.: Global energy conversion rate from geostrophic flows into internal lee waves in the deep ocean, Geophys. Res. Lett., 38, 2011.

Norwegian Meteorological Institute: MET Nordic operational archive, https://github.com/metno/NWPdocs/wiki/MET-Nordic-dataset, accessed 18 December 2024, 2024.

Notz, D. and Worster, M. G.: Desalination processes of sea ice revisited, J. Geophys. Res.: Oceans, 114, 2009.

Nunes, R. and Simpson, J.: Axial convergence in a well-mixed estuary, Estuarine, Coastal and Shelf Science, 20, 637–649, 1985.

Osborn, T. R.: Estimates of the local rate of vertical diffusion from dissipation measurements, J. Phys. Oceanogr., 10, 83–89, 1980.

Osborn, T. R. and Cox, C. S.: Oceanic fine structure, Geophys. Fluid Dyn., 3, 321–345, 1972.

Pemberton, P., Nilsson, J., Hieronymus, M., and Meier, H. M.: Arctic Ocean water mass transformation in S–T coordinates, J. Phys. Oceanogr., 45, 1025–1050, 2015.

Peters, H.: Observations of stratified turbulent mixing in an estuary: Neap-to-spring variations during high river flow, Estuarine Coast. Shelf Sci., 45, 69–88, 1997.

Peters, H. and Bokhorst, R.: Microstructure observations of turbulent mixing in a partially mixed estuary. Part I: Dissipation rate, J. Phys. Oceanogr., 30, 1232–1244, 2000.

Peters, H. and Bokhorst, R.: Microstructure observations of turbulent mixing in a partially mixed estuary. Part II: Salt flux and stress, J. Phys. Oceanogr., 31, 1105–1119, 2001.

Pietrzak, J. D.: The use of TVD limiters for forward-in-time upstream-biased advection schemes in ocean modeling, Monthly Weather Rev., 126, 812–830, 1998.

Pritchard, D. W.: Observations of circulation in coastal plain estuaries, Estuaries, AAAS Publ., 83, 37–44, 1967.

Purkiani, K., Becherer, J., Flöser, G., Gräwe, U., Mohrholz, V., Schuttelaars, H. M., and Burchard, H.: Numerical analysis of stratification and destratification processes in a tidally energetic inlet with an ebb tidal delta, J. Geophys. Res. Oceans, 120, 225–243, 2015.

Qu, L., Hetland, R. D., and Schlichting, D.: Mixing pathways in simple box models, J. Phys. Oceanogr., 52, 2761–2772, 2022.

Ralston, D. K., Cowles, G. W., Geyer, W. R., and Holleman, R. C.: Turbulent and numerical mixing in a salt wedge estuary: Dependence on grid resolution, bottom roughness, and turbulence closure, J. Geophys. Res., 122, 692–712, 2017.

Ramadhan, A., Wagner, G., Hill, C., Campin, J.-M., Churavy, V., Besard, T., Souza, A., Edelman, A., Ferrari, R., and Marshall, J.: Oceananigans. jl: Fast and friendly geophysical fluid dynamics on GPUs, J. Open Source Software, 5, 2020.

Rayson, M. D., Gross, E. S., Hetland, R. D., and Fringer, O. B.: Using an isohaline flux analysis to predict the salt content in an unsteady estuary, J. Phys. Oceanogr., 47, 2811–2828, 2017.

Reese, L., Gräwe, U., Klingbeil, K., Li, X., Lorenz, M., and Burchard, H.: Local mixing determines spatial structure of diahaline exchange flow in a mesotidal estuary: A study of extreme runoff conditions, J. Phys. Oceanogr., 54, 3–27, 2024.

Reese, L., Becker, M., Holtermann, P., Li, X., and Burchard, H.: The role of the shoal – salt mixing mechanisms in a partially mixed tidal estuary with channel-shoal geometry, Cont. Shelf Res., 299, 105 669, 2026.

Rippeth, T. P., Fisher, N., and Simpson, J. H.: The cycle of turbulent dissipation in the presence of tidal straining, J. Phys. Oceanogr., 31, 2458–2471, 2001.

Rodi, W.: Examples of calculation methods for flow and mixing in stratified fluids, J. Geophys. Res., 92, 5305–5328, 1987.

Ross, L., Huguenard, K., and Sottolichio, A.: Intratidal and fortnightly variability of vertical mixing in a macrotidal estuary: The Gironde, J. Geophys. Res. Oceans, 124, 2641–2659, 2019.

Rummel, K., Strauß, T., Lauer, F., and Gräwe, U.: Real-time prediction of salt intrusion in tidal estuaries using long short-term memory networks, J. Geophys. Res. Machine Learning Comput., 2, e2025JH000 768, 2025.

Schlichting, D., Qu, L., Kobashi, D., and Hetland, R.: Quantification of physical and numerical mixing in a coastal ocean model using salinity variance budgets, J. Adv. Model. Earth Syst., 15, e2022MS003 380, 2023.

Schumann, U. and Gerz, T.: Turbulent mixing in stably stratified shear flows, J. Appl. Meteorol., 34, 33–48, 1995.

Scully, M. E. and Friedrichs, C. T.: Sediment pumping by tidal asymmetry in a partially mixed estuary, J. Geophys. Res.: Oceans, 112, 2007.

Scully, M. E., Friedrichs, C. T., and Brubaker, J.: Control of estuarine stratification and mixing by wind-induced straining of the estuarine density field, Estuaries, 28, 321–326, 2005.

Scully, M. E., Michel, A. P., Nicholson, D. P., and Traylor, S.: Spatial and temporal variations in atmospheric gas flux from the Hudson River: the estuarine gas exchange maximum, Limnol. Oceanogr., 67, 1590–1603, 2022.

Shchepetkin, A. F. and McWilliams, J. C.: The regional oceanic modeling system (ROMS): a split-explicit, free-surface, topography-following-coordinate oceanic model, Ocean Modell., 9, 347–404, 2005.

Sievers, J., Malte, R., and Milbradt, P.: EasyGSH-DB: Bathymetrie (1996-2016), https://doi.org/https://doi.org/10.48437/02.2020.K2.7000.0002, accessed 18 December 2024, 2020.

Simpson, J. H., Brown, J., Matthews, J., and Allen, G.: Tidal straining, density currents, and stirring in the control of estuarine stratification, Estuaries and Coasts, 13, 125–132, 1990.

Skyllingstad, E. D. and Wijesekera, H. W.: Large-eddy simulation of flow over two-dimensional obstacles: high drag states and mixing, J. Phys. Oceanogr., 34, 94–112, 2004.

Smagorinsky, J.: General circulation experiments with the primitive equations: I. The basic experiment, Mon. Weather Rev., 91, 99–164, 1963.

Smolarkiewicz, P. K.: Multidimensional positive definite advection transport algorithm: an overview, Int. J. Num. Meth. Fluids, 50, 1123–1144, 2006.

Stacey, M. T., Fram, J. P., and Chow, F. K.: Role of tidally periodic density stratification in the creation of estuarine subtidal circulation, J. Geophys. Res., 113, doi: 10.1029/2007JC004 581, 2008.

Stacey, M. W., Monismith, S. G., and Burau, J. R.: Measurements of Reynolds stress profiles in unstratified tidal flow, J. Geophys. Res., 104, 10 933–10 949, 1999.

Strotmann, T.: Deutsches Gewässerkundliches Jahrbuch. Elbegebiet, Teil III. Untere Elbe ab der Havelmündung. 2014, ISSN: 0949-3654, 2017.

Sutherland, D. A., MacCready, P., Banas, N. S., and Smedstad, L. F.: A model study of the Salish Sea estuarine circulation, J. Phys. Oceanogr., 41, 1125–1143, 2011.

Thorpe, S. A.: Turbulence and mixing in a Scottish loch, Phil. Trans. R. Soc. London, A 286, 125–181, 1977.

Trowbridge, J., Geyer, W., Bowen, M., and Williams III, A.: Near-bottom turbulence measurements in a partially mixed estuary: Turbulent energy balance, velocity structure, and along-channel momentum balance, J. Phys. Oceanogr., 29, 3056–3072, 1999.

Umlauf, L.: A note on the description of mixing in stratified layers without shear in large-scale ocean models, J. Phys. Oceanogr., 39, 3032–3039, 2009.

Umlauf, L. and Burchard, H.: A generic length-scale equation for geophysical turbulence models, J. Mar. Res., 61, 235–265, 2003.

Umlauf, L. and Burchard, H.: Second-order turbulence models for geophysical boundary layers. A review of recent work, Cont. Shelf Res., 25, 795–827, 2005.

Verspecht, F. I., Burchard, H., Rippeth, T. P., Howarth, M. J., and Simpson, J. H.: Processes impacting on stratification in a region of freshwater influence: Application to Liverpool Bay, J. Geophys. Res. Oceans, 114, 11 022, 2009.

Walin, G.: A theoretical framework for the description of estuaries, Tellus, 29, 128–136, 1977.

Walin, G.: On the relation between sea-surface heat flow and thermal circulation in the ocean, Tellus, 34, 187–195, 1982.

Wang, T. and Geyer, W. R.: The balance of salinity variance in a partially stratified estuary: Implications for exchange flow, mixing, and stratification, J. Phys. Oceanogr., 48, 2887–2899, 2018.

Wang, T., Geyer, W. R., and MacCready, P.: Total exchange flow, entrainment, and diffusive salt flux in estuaries, J. Phys. Oceanogr., 47, 1205–1220, 2017.

Wang, X., Kukulka, T., and Plueddemann, A. J.: Wind fetch and direction effects on Langmuir turbulence in a coastal ocean, J. Geophys. Res. Oceans, 127, e2021JC018 222, 2022.

Warner, J. C., Geyer, W. R., and Lerczak, J. A.: Numerical modeling of an estuary: A comprehensive skill assessment, J. Geophys. Res.: Oceans, 110, 2005a.

Warner, J. C., Sherwood, C. R., Arango, H. G., and Signell, R. P.: Performance of four turbulence closure models implemented using a generic length scale method, Ocean Modell., 8, 81–113, 2005b.

Warner, J. C., Geyer, W. R., Ralston, D. K., and Kalra, T.: Using tracer variance decay to quantify variability of salinity mixing in the Hudson River estuary, J. Geophys. Res., 125, e2020JC016 096, 2020.

Wasserstraßen- und Schifffahrtsamt Hamburg: DGM-W 2010 Unter- und Außenelbe (Digitales Geländemodell des Wasserlaufes – Multifunktionsmodell), https://www.kuestendaten.de/Tideelbe/DE/Service/Kartenthemen/Kartenthemen_node.html, accessed 18 December 2024, 2011.

Wasserstraßen- und Schifffahrtsamt Hamburg: DGM-W 2022 Außen- und Unterelbe (Digitales Geländemodell des Wasserlaufes – Multifunktionsmodell), https://www.kuestendaten.de/Tideelbe/DE/Service/Kartenthemen/Kartenthemen_node.html, accessed 19 October 2024, 2024.

Wasserstraßen- und Schifffahrtsamt Magdeburg: Abflussstation Neu Darchau, https://www.kuestendaten.de/DE/Services/Messreihen_Dateien_Download/Download_Zeitreihen_node.html, accessed 18 December 2024, 2024.

Wasserstraßen- und Schifffahrtsamt Weser-Jade-Nordsee: Digitales Geländemodell des Wasserlaufes (DGM-W) 2016 der Weser (ARGE inphoris GmbH – smile consult GmbH 2018), provided by Bundesanstalt für Wasserbau (BAW), 2023.

Xiong, J., Shen, J., and Qin, Q.: Exchange flow and material transport along the salinity gradient of a long estuary, J. Geophys. Res. Oceans, 126, e2021JC017 185, 2021.

Yan, C., McWilliams, J. C., and Chamecki, M.: Overlapping boundary layers in coastal oceans, J. Phys. Oceanogr., 52, 627–646, 2022.

Yin, D., Ralston, D. K., Warner, J. C., Ganju, N. K., and Harris, C. K.: Wind pumping dominates landward salt transport in a weakly tidal estuary, J. Geophys. Res. Oceans, 130, e2025JC022 683, 2025.

Yu, L.: On sea surface salinity skin effect induced by evaporation and implications for remote sensing of ocean salinity, J. Phys. Oceanogr., 40, 85–102, 2010.

Zalesak, S. T.: Fully multidimensional flux-corrected transport algorithms for fluids, J. Comput. Phys., 31, 335–362, 1979.

Zhang, Y. J., Ye, F., Stanev, E. V., and Grashorn, S.: Seamless cross-scale modeling with SCHISM, Ocean Modell., 102, 64–81, 2016.